THE FEASIBILITY OF LOW-COST, DUAL-POLARIZED, PHASE-TILT ANTENNA ARRAYS FOR DENSE RADAR NETWORKS

A Dissertation Presented

by

JORGE L. SALAZAR CERREÑO

Submitted to the Graduate School of the
University of Massachusetts Amherst in partial fulfillment
of the requirements for the degree of

DOCTOR OF PHILOSOPHY

September 2012

Electrical and Computer Engineering

UMI Number: 3546048

UMI

Dissertation Publishing

UMI 3546048

ProQuest®

THE FEASIBILITY OF LOW-COST, DUAL-POLARIZED, PHASE-TILT ANTENNA ARRAYS FOR DENSE RADAR NETWORKS

A Dissertation Presented

by

JORGE L. SALAZAR CERREÑO

Approved as to style and content by:

_____

David J. McLaughlin, Chair

_____

Stephen Fraiser, Member

_____

Daniel H. Schaubert, Member

_____

Paula L. Sturdevant Rees, Member

_____

Chistopher V. Hollot, Department Chair
Electrical and Computer Engineering

To my family in special to my wife Patricia, my parents and my two
wonderful kids Andrea and Alejandro

ACKNOWLEDGMENTS

First, I would like to extend my sincerest thanks to my PhD advisor, Professor David McLaughlin, with whom I have had the privilege of working with and gave me the opportunity to design and implement the "CASA phased array antenna project" also for the support all the way to the graduating. My most sincere thank you goes also to Eric Knapp, who discuss with me technical aspects of the project on a daily basis. I want to give a special thanks to my good friend Rafael Medina for his great contribution with the T\R modules and calibration process.

I am also would like to thanks to Dr. Stephen Fraiser for his involvement and leadership in the solid state radar group and Dr. Paul Siqueira for his advice and interest in the wet radome model. My special thanks to Dr. Daniel Schaubert and Dr. Marinos Vuovakis for clarify my doubts and answer my questions about phased array antennas. I also want to particularly thank to Dr. David Pozar for serving as my adviser for a short period of time and teaching me everything about frequency scan microstrip patch array antennas. Thanks to Dr. Paula Rees for accepting to serve in my committee. Many thanks are due to my good friend Jorge Trabal for all of his technical support and radar discussions. Thanks to Apoorva Bajaj, Tom Hartley, Brenda Phillips, Susan Lanfare, Janice Brickley, Marci Kelly and Linda Klemik for always providing the administrative support.

Most importantly, I wish to express my profound appreciation to my family, who have provided their support and encouragement all the time necessary to finish this ambitious project undertaken in my life. Especially thanks to my wife Patricia Zegarra, who was a fundamental component to achieve my goals and keep things in

perspective when the times were difficult. Thanks to my parents and brothers for all their love and support.

Finally, to all my friends in the CASA, MIRSL and CASCA labs specially, to Razi Ahmed, Benjemin St. Peter, Peisang Tsai, Ninoslav Majurec, Krzysztof Orzel, Vijey Venkatesh, Robert Palumbu, Ogechi Ibe, Edin Insanic, Franchesc Junyet, Mauricio Sanchez, Justin Creticos, Steve Holland, Chris Merola, Gita Pathak, Sreenivas Kasturi and Wajih Esallal. I express my thanks for their most invaluable support and friendship.

ABSTRACT

THE FEASIBILITY OF LOW-COST, DUAL-POLARIZED, PHASE-TILT ANTENNA ARRAYS FOR DENSE RADAR NETWORKS

SEPTEMBER 2012

JORGE L. SALAZAR CERREÑO

B.Sc., UNIVERSIDAD PRIVADA ANTENOR ORREGO

M.Sc., UNIVERSITY OF PUERTO RICO, MAYAGUEZ

Ph.D., UNIVERSITY OF MASSACHUSETTS AMHERST

Directed by: Professor David J. McLaughlin

This document address the feasibility of low-cost, dual-polarized, X-band phased array antennas for use in dense radar networks for weather surveillance. The "phase-tilt" architecture under investigation combines one-dimensional, electronic beam steering with mechanical actuation (tilting) to achieve a low-cost design capable of rapid, two-dimensional beam positioning without the use of a large scanning pedestal. This architecture is less complex and costly than a full, two-dimensional "phase-phase" array. In addition to meeting requirements for cost, it has the potential to meet requirements for off-axis polarization performance and other key requirements. A prototype antenna already has been designed, fabricated and tested. It defines a new state-of-the-art for remote sensing of weather using small radars. The prototype antenna also serves as a test bed and proof of concept for exploring a potential future

network comprised of many antennas arranged in a dense network. This dissertation reviews the current state-of-the-art (in weather radars, dense radar networks, dual-polarized radars, and phased arrays); presents the design, verification testing, and validation experiments of the prototype array; and establishes performance requirements for this technology for deployment in future networks of small weather radars.

TABLE OF CONTENTS

APPENDICES

LIST OF TABLES

LIST OF FIGURES

CHAPTER 1

INTRODUCTION

1.1 Problem statement

Weather radars implemented with phased array technologies are receiving increased interest by the weather radar community due to this technology's fast beam steering and high flexibility to implement a diversity of scanning modes and multi-function capabilities. In 2001 the National Research Council (NRC) identified the Phased-Array technology as the best candidate to upgrade the current US radar system. Replacing 500 radars (for weather, or air traffic surveillance) with a Multi-function Phased Array Radar (MPAR) network of 300 has the potential to be a cost effective solution, reducing $3 B in life cycle cost [1]. The inability of observation at lower altitudes because of terrestrial curvature and terrain blockage presents a fundamental limitation of any long-range radar network system (with a spacing of more than 200 km). The Engineering Research Center (ERC) for Collaborative Adaptive Sensing of the Atmosphere (CASA) offers an alternative approach, one that provides more compressive coverage of the lower part of the atmosphere (below 3 km altitude). It relies on the concept of a low-cost, low-power, dense radar network [2],[3]. CASA envisions a dense radar network with radars arranged in a triangular grid of 30 km spacing. The network will have full overlapping coverage in order to ensure multiple simultaneous views of a specific region, and also to reduce design complexity (cost, antenna size, peak transmitted power and infrastructure required). Dual-polarized radar measurements are required principally for improving quantitative precipitation and hydrometer classification, and also to compensate for attenuation and X-band

frequencies. A dense radar deployment with several thousand short-range and small phased array radar nodes is attractive since it provides a large production volume (million of components), which will help to keep down the cost of the radars. A number of factors, including short-range radars (<40 km), low-power (<100 W), short wavelength (~3 cm), small antenna sizes (<1 m^2), and small weight (<200 lb), significantly reduce costs because they make it possible to reuse existing infrastructure (rooftops, sides of buildings and cell-phone towers). Phased array radars are also more reliable than a single, centralized transmitter; their life cycles are much larger, and their operational cost is significantly less compared to a conventional dish radar system.

Two primary factors must be considered in the feasibility determination for the projected architecture, namely, economic challenges with respect to cost control, and technical challenges regarding the polarization performance of these small, phased array antennas. The Engineering Research Center for Collaborative Adaptive Sensing of the Atmosphere (CASA) has estimated that the purchase price of a 1 meter sized, four-face phased array is constrained to at most \$200 k [3]. Implementing a 2-dimensionally-steered military phased array with a 1 m^2 aperture in the X-band requires approximately 4,000 antenna elements. The cost estimated is about \$1 M/m^2. This estimate is obtained assuming each element is controlled by a separate transmitter\receiver module (T\R), with a module costs at current rates of \$ 250. The \$1 M/m^2 cost implies a 50:1 cost level reduction to implement a low-cost phased array architecture for the CASA radar network. Clearly, one of the greatest challenges for the CASA team is to achieve a design of a phased array antenna that meets this target. The small size (only 1 meter on a side), and low-power characteristic of the antenna (averaging ~10s of watts) suggests an approach involving a combination of electronic and mechanical tilting of the array.

The second key design challenge associated with the CASA project is related to the polarization performance of the phased array antennas. Weather radars operate at two orthogonal polarizations to measure parameters such as the ellipticity of raindrops. Currently, polarization requirements for weather radars are defined based on parabolic dish antenna patterns. Dual-polarization operation using parabolic dish antennas is well developed, and many research papers and text books have been published addressing design and performance of such antennas for weather radar. Dish antenna patterns do not change with beam position, so the polarization behavior of a dish is constant as the antenna scans. But dual-polarization for phased arrays is another matter. A dual-polarization performance challenge exists to maintain low cross-polarization levels and well-matched vertical and horizontal beam patterns as the array scans away from the boresight axis. Degradation in the polarization performance of the electronically scanned antenna beam patterns can occur as the beam position steers from broadside. The quality of measured polarimetric data in weather radars is affected by the mismatched co-polar patterns, and the isolation of horizontal (H) and vertical (V) polarization is degraded.

1.2 Significance

Sampling of the lower part of the atmosphere is important to the atmospheric scientific community, which tries to improve day-to-day forecasting and warning ahead of localized hazardous phenomena (such as tornados, storms, flooding) that affect thousands of lives in the U.S. each year. CASA ERC has proposed the implementation of a dense radar network using low-cost (<$200 k per node), short-range (<30 km), low power (<100 W) small radars in X-band, implemented in existent infrastructure. Since 2007, CASA has shown the benefits of a dense radar network tested in Oklahoma using four dish spin radar nodes with full overlapping coverage. The target cost estimated was $200k. CASA expended the amount of $259 k for each radar

(parts only). The operational cost for each radar is estimated to be \$26 k per year. The IP1 radar system uses a dish antenna, a fast linear actuator for elevation, and a fast pedestal for azimuth scans. The mechanical frame to support both positioners and the rest of the radar system is large and heavy, and the cost associated (in parts and infrastructure) is relatively high. The azimuth positioner alone represents 50 % of the parts cost. The phased array antenna architecture proposed in this dissertation addresses these issues and satisfies the cost and performance requirements of the CASA dense radar network. The antenna architecture and fabrication process permit significant cost reduction, with a cost of \$50 k per panel and \$180 k per radar node, as estimated for a production volume of 1000 units. The low profile characteristics of the flat panel and low weight (<200 lb.) makes this radar ideal for installation in existent infrastructures, such as roof tops and wireless towers.

The impacts of this research project can be summarizes as follows:

1. Provides to CASA ERC a cost effective radar platform for implementing the CASA dense radar network.

2. Demonstrates feasibility of cost and performance for the CASA dense radar network.

3. Provides a low cost phased radar at less than \$200 k per node.

3. Provides a test platform to obtain experimental algorithms for future phased array antenna deployments.

1.2.1 Literature review

A brief overview of current experimental and operational dual-polarized phased weather radars for meteorological applications is provided. This review emphasizes current capabilities, performance, and cost of phased array antennas for a radar system configured in a network for meteorological applications.

1.2.2 Phased array weather radars

For weather applications, phased array antennas are desirable in part because they offer the advantage of fast scanning, which allows the sampling of large volumes. This significantly improves precipitation characterization and rainfall estimation without using expensive mechanical parts that carry substantial operation and maintenance costs. Increased recent interest in using phased array technology in the weather community is primarily motivated by a significant improvement in RF component performance (at upper frequencies of S-band) and by the reduced cost of RF Microwave components (high power amplifiers, phase shifters, low noise amplifiers, etc.), this is due to the rapid proliferation of digital wireless market technologies (GSM, CDMA, PCs, WiFI and WiMAX). It appears that substantial development of weather radars using phased array technology is imminent. In 1993 The European Union (EU) Cooperation in Science and Technology (COST) group implemented a five-year European research program concentrating on advanced weather systems to develop guideline specifications for a future generation of European radar systems using phased array technology [4]. In 2001, the National Research Council (NRC) identified phased array technology as the best candidate to replace the existent radar network (NEXRAD). In 2006 a committee of radar experts sponsored by the US National Oceanic and Atmospheric Administration (NOAA), Federal Aviation Administration (FAA), Department of Defense (DoD), and the Department of Homeland Security (DHS) have undertaken planning for the possible replacement of existent radar networks with a multifunction system designed to meet the surveillance needs and mission requirements of the several agencies simultaneously. At the same time, two mobile radars implemented with electronic scanning array antennas were deployed in the southern plains in order to evaluate convective storms. Shapiro and Wurman at [5] presented measured results of the evolution of a tornado in Kansas using this technology. Mobile radar designed to operate in X-band uses a frequency-scan slot-waveguide array

antenna; the scanning antenna uses a frequency range of 9.3 GHz to 9.75 GHz in order to have a beam steering elevation of 13.5 degrees. In addition, Rapid scan radar uses mechanical parts to perform scanning in the azimuth direction. This system demonstrates the great advantages offered by fast scanning radars for significantly improving the capability to evaluate fast-evolving convective storms. During 2007 and 2008, a hybrid mechanically-phased array antenna called MWR-05XP (Mobile Weather Radar-2005, X-band, Phased array) was used in a field experiment in the southern region of the US [6]. This radar is a converted military phased array antenna, and it was modified by the CIRPAS (Center for Interdisciplinary Remotely-Piloted Aircraft Studies), the Naval Postgraduate School in Monterey CA, and the NSSL (National Severe Storm Laboratory). This radar, operating at 9.37 GHz, performs beam steering using ferrite phase shifters and in azimuth scans using a fast mechanical pedestal (30 rpm). It also can perform electronic scans using this frequency due to a series-fed slot-waveguide array antenna like the MWR-05XP. Due to its rapid update time (10-30 seconds), this radar permits better observation of convective storms, like tornados events. Since 2004, scientists at the NSSL have been exploring the high-temporal resolution scanning capabilities of the S-band phase-array antenna as part of the National Weather Radar Test-bed (NWRT) program in Norman, Oklahoma. Like prior e-scan radars, the NWRT is a military radar that operates at S-band (AN/SPY1-A of the Navy's Aegis system) modified to be operated as weather radar. The phased array is a single polarized passive array antenna composed of 4,352 open ended waveguides that provide an electronic beam (with HPBW of 1.5°) scanning in both azimuth and elevation on a pulse-to-pulse basis. In 2008 NSSL examined data from three different convective storms (collected in 2006 using the NWRT over a sector scan of 90 ° in azimuth). It demonstrated the capability to adaptively scan storms at a high temporal resolution that is not possible with weather surveillance radar WSR-88D [7]. In 2009 Douglas Carlson presented a summary of significant

6

progress in the development of S-band T/R modules for multifunction capabilities using high efficiency semiconductor technology [8]. This work has been conducted by the MPAR research group at MITs Lincoln Laboratory and at M/A-COM over the last two years. However, the high cost associated with large array antennas is still one of the biggest limitations in order to have this system considered a real potential solution to MPAR.

1.2.3   Radar weather network

In the U.S. two large operational radar networks are implemented for weather applications. The first one, NEXRAD (WSR-88D), was developed in the 1980s to provide volumetric scans of the atmosphere, allowing operators to observe vertical structures of storms and provide detailed wind profiles above the radar site. The radar network consists of a network of 156 long range (240 km - 450 km) radar nodes that monitor precipitation and storms over the contiguous United States. The radar operates at 10 cm wavelength (S-band), utilizes a $1°$ transmit and receive beam, and transmits uncoded 750 kW pulses with selectable durations of 1.6 or 4.7μsec. NEXRAD is fully coherent of supporting ground clutter suppression and weather Doppler spectrum moment estimation [9]. The second radar, the Terminal Doppler Weather Radar (TDWR), was developed in response to a series of commercial aircraft accidents caused by low altitude wind shear [10]. The network has 48 active radars across the United States and Puerto Rico. This radar system was funded by the United States Federal Aviation Administration, and was developed in the early 1990's at MITs Lincoln Laboratory to assist air traffic controllers by providing real-time wind shear detection and high-resolution precipitation data. Due to limited space requirements, the TDWR was designed at 5 cm wavelength (C-band). The antenna beamwidth of TDWR of about $0.5°$ offers a significant improvement in spacial resolution relative to NEXRAD, and transmits uncoded, 1 μsec, 250 kW pulses [11].

The TDWR is designed to operate at short range, near the airport of interest, and has an area of high-resolution coverage limited to just 96 km, as compared to the 250 km of the conventional WSR-88Ds. The short wavelength (5 cm wavelength) the TDWRs enables this radar to see details as small as 150 meters along the beam, at the radar's regular range of 96 km. The azimuth resolution of the TDWR is nearly twice what is available in the WSR-88D. Each radial in the TDWR has a beam width of $0.55°$. The average beam width for the WSR-88D is $0.95°$. One the most serious drawbacks to using the TDWRs is signal attenuation resulting from heavy precipitation falling near the radar. Since the TDWRs use the shorter 5 cm wavelength, radar signals are more easily absorbed and scattered away by precipitation.

Given that both NEXRAD and TDWR are relatively long-range radar, the curvature of the earth represents a limiting factor in their ability to observe the lower part of the atmosphere, where severe atmospheric events can occur. The Engineering Research Center (ERC) for Collaborative Adaptive Sensing of the Atmosphere (CASA) addresses lower atmosphere coverage (below 3 km altitude) using the concept of a low cost, low power dense radar network. In order to probe this concept, CASA designed, fabricated and deployed a four-radar network in Oklahoma. Each radar unit operates at 9.41 GHz (X-band) using a 1.2 m parabolic dish antenna for dual-polarization capability. To perform at high temporal resolution, each unit is implemented with a high-performance pedestal that provides scan rates of 24 °/sec. Since 2007, data collected in CASA IP1 systems have demonstrated an improved scan performance providing scanning update rates 5 times faster than the nearest WSR-88D [19].

CASAs next step is to deploy a phased array antenna in the radar network. Two approaches are currently under development to obtain a dual-polarized e-scan array for CASA. The first, being developed by Raytheon, is based on low-cost microwave semiconductors combined with low-cost packaging, fabrication and assembly techniques [13]. The second approach, which is being developed by the CASA solid state

group, is based on a low-cost antenna architecture that uses only 64 T/R modules to perform e-scanning in azimuth while scanning in elevation is controled using a rapid mechanical part [14]

1.3 Contribution

This work presents a design paradigm for a phased array antenna to be used for a weather radar system that is configured to operate in a dense network environment, and that aims to maximize performance and minimize cost and complexity. In contrast to conventional stand-alone military phased array radars, this work uses the advantages of a radar configured in a network to minimize cost and optimize scanning radar performance.

The specific contributions of this work can be summarized as:

(1) Contributes to understanding system requirements for phased array weather radars.

(2) Demonstrates the feasibility of low-cost, phase/tilt array antennas that satisfy the polarization and other performance requirements needed for deployment in networks of weather radars.

(3) Captures cost-performance trade-offs of phased array antennas for weather radars applications using theoretical models that accurately predict the behavior of the radar system in radar network topology.

(4) Provides an experimental platform for future development and design of a dual-polarized phased array antenna.

(5) Facilitates the transference of the system to industry and academic partners.

1.4 Dissertation overview

In detail, the specific contributions of this work can be summarized as follows:

Chapter 2 discussed the requirements and specifications for dual-polarized phased arrays radars used for weather surveillance. It references meteorological needs and requirements of the meteorological community. It also presents the system requirements of a CASA phased array radar to operate in a dense radar network based on the experience of the current CASA IP1 radar network. Chapter 3 discussed a trade-off analysis of key design parameters of electronically scanned phased array antennas for a single radar node and also for a radar system configured in a dense network. Initial requirements for the IP1 radar network system were used as a starting point to define a set of radar specifications for the new CASA phased array radar. Chapter 4 outlines the design of the antenna array. Design details of the radiating element and a synthesis model to design linear and planar array antenna are discussed. Radome design, T\R modules, and other parts of the antenna are also covered in this chapter. Chapter 5 describes the fabrication integration and testing of the antenna array prototype composed of 72x32 elements for the CASA phased-array radar. This chapter also discusses the performance of the measured results of the antenna array, T\R modules and radome. Chapter 6 presents the predicted performance of the polarimetric CASA phased array radar as a function of the scanned measured antenna patterns. The measured patterns in combination with predicted antenna patterns based on the measured embedded element patterns are used to estimate the accuracy of the two polarimetric radar parameters (Z_{dr} and ICPR$_2$). Considering that meteorological radar are meant to operate in presence of rain, a model to predict the radar performance under rain conditions is introduced. Chapter 7 discusses the cost of the CASA phased radar system as a function of antenna performance. The performance-model evaluates the performance degradation of the Effective Radiated Power (ERP), the antenna gain in reception (G_R), and the mean-squared sidelobe level (MSLL) as function of the failure rate of the phased array antenna. The cost-model, performance

model and reliability model are integrated to define the life cycle cost model of the proposed CASA phased array antenna.

CHAPTER 2

REQUIREMENT FOR PHASED ARRAY WEATHER RADARS

2.1 Introduction

This chapter presents the radar requirements and specifications for dual-polarized phased arrays used for weather surveillance radar. It references meteorological requirements of the meteorological community. The staring point for this analysis are preliminary studies that define system requirements for conventional radar (using reflector antennas), with emphasis on antenna performance. The scanning performance of electronically steered antennas were incorporated to develop the complete set of requirements needed for the phased array antennas used for weather radar applications.

2.2 Range

Operational weather radar in the U.S. (e.g. NEXRAD and TDWR) are designed to operate over long distances ($\sim$250 km for NEXRAD $\sim$100 km for TDWR). Beyond this range radar detects only high altitudes because the curvature of the earth. In the case of WSR-88D/NEXRAD at the 250 km range, the radar horizontal is about 3 km high. This represents a serious limitation for current radar systems because, below this altitude, radar cannot observe any atmospheric events that occur near the ground. Typically long-range radar operates at wavelengths of $\sim$10 cm (S-band) in order to minimize the attenuation of the medium. They require large antennas apertures with high gain and narrow beamwidth to sense long distances. For example, the

12

WSR-88D/NEXRAD system requires a ~8.5 m diameter antenna and a 1° antenna beamwidth to obtain a spatial resolution of 4.3 km at 250 km distance. WSR-88D requires ~750 kW of transmit peak power, and the TDWR requires ~100 kW to obtain enough sensitivity for sampling atmospheric events at those distances. The biggest drawbacks of long-range radars are the need for dedicated land, high power and substantial operational resources. In contrast to long-range radars, short-range radars are small radars designed to operate short distances, typically less than 100 km since, at higher frequency, the atmospheric attenuation in the radar path can considerably affect the accuracy of the measurements.

2.3 Wavelength

The radar wavelength selected for a radar system impacts radar performance, the cost of the radar system, and the infrastructure required. Shorter wavelength radars (e.g. 3 cm for X-band and 5 cm for C-band) require smaller antennas and provide better spatial resolution, for the same antenna aperture size, than radars operating at 10 cm (S-band). One drawback of short wavelength radars is the fact that radar signals (at frequencies greater than 10 GHz) can be significantly affected by the attenuation of the medium. Specific attenuation less than 0.02 dB km^{-1} is required for achieving accurate measurements in a range of 230 km in a S-band radar system. In order to have consistent accuracy performance using short wavelength radars, the maximum range needs to be significantly reduced. An alternative way to compensate for the effects of attenuation in the medium is using polarimetric radars. X-band radars capable of dual-polarization have demonstrated an improvement in rainfall estimation when compared to single polarization measurements [15]. Methods to correct path attenuation based on specific differential phase shift [16] and network-based correction have been developed for CASA radars [17].

2.4 Volumetric coverage and update time

Different scan patterns can be used for a volumetric sampling of an atmospheric event. A long-range radar network such as NEXRAD requires a variety of scan modes called Volume Coverage Patterns (VCPs). VCP11 and VCP21 are the patterns used for precipitation in NEXRAD. VCP11 provides continuous of 360 ° scanning for 5 minutes in azimuth and 14 elevation positions, starting with 0.5 ° and ending with 19.5 °. VCP21 also provides continuous scanning of 360 ° in azimuth with only 9 elevation positions, starting with 0.5 ° and ending with 19.5 ° in 6 minutes. To improve the lead time for rapid evolving events (such as tornados, and microbursts) near the earth's surface, a faster version of VCP11 called VCP12 was tested and implemented in 2001-2003 [18]. The VCP12 can scan the same volume in 4.2 minutes, and consists of 14 elevation steps having denser sampling at lower elevation angles.

The CASA IP1 radar system was developed as a new approach to sample a volumetric event with improved update abilities and using conventional dish antennas. This CASA radar network is designed as a triangular grid radar network with overlapped radar coverage to support adaptive scanning volume patterns. The high performance pedestal, with a rate of speed of up to 240 $°/s$ and an acceleration rate of up to 120 $°/s^2$, offers a unique adaptive scanning pattern that has a scanning update 5 times faster than the current operational NEXRAD radar system [3]. CASA radars can perform sector scans in the range of 60 ° to 270 °, permitting an increase in the number of steps for elevation scanning (1 °, 3 °, 5 °, 7 °, 9 °, 11 °and 14°). This is helpful for better vertical analysis of storm structures [12]. One limitation of the IP1 radar system is the cost of the high performance mechanical scanning parts. About 52 % of the overall cost of the parts of the IP1 radar system pertains to the cost of the positioner (azimuth and elevation) and infrastructure required to support 1200 lb. An alternative solution, which is also proposed by CASA ERC, is to replace the dish radar system with small, low profile, low weight phased array

antennas. Considering the maximum scanning range for a PAR is about 90 ° (±45 °), 4 two-dimensional scanning antenna panels are required to perform 360 ° scanning in azimuth. A demonstration of the rapid sampling of severe storms using the National Weather Radar Tested Phased Array Radar (NWRT-PAR), as compared with the Weather Surveillance Radar Doppler (WSR-88D), is given in [7]. The PAR performs a sector volumetric scanning of 90 ° in 58 seconds, while WSR-88D takes 4.3 minutes for the same volume.

Two dimensional phased array antennas are expensive radars. The aperture size required to perform $2°$ beamwidth is about 1 m^2 (in X-band) and requires about 4000 T\R modules (spaced $0.5\lambda_\circ$). Considering that the TR module is the critical cost factor of a PAR, and assuming (optimistically) the cost of an X-band TR is about $100, the two dimensional phased array antenna cost will be about $ 0.5 M/panel and $ 2 M/per radar node (4 panels). CASA ERC needs low-cost phased array antennas, where the cost can be less than $200 k per node (or $50 k per panel). The only possibility to achieve a cost reduction factor of 40 is to combine electronic scanning in one dimension with mechanical scanning in the other dimension. CASA ERC has proposed, implemented, and tested a low-cost phased array antenna that performs electronically in azimuth and mechanically in elevation. The cost of this panel is $50 k in large production volume. Having 4 panels per node, the volume scan pattern can be performed with a sector of 90 ° (±45 °) and an elevation of up to 14 °.

2.5   Spatial resolution

Spatial resolution is defined by the size of the phenomena event, and is limited by the aperture size of the antenna and the radar range. Long-range radar systems such as WSR-88D require an aperture size of 8.5 m in diameter to provide an antenna beamwidth of $1°$. Even though the beamwidth is narrow, the spatial resolution is significantly degraded for longer distances. In a range of 40 km, the spatial resolution

of the WSR-88D is about 0.7 km, however in a 230 km range, the radar is limited to observing atmospheric events larger that 4 km. In short-range radars, the spatial resolution can be better, since the radar range is much smaller (<40 km). CASA X-band radars use an antenna aperture of 2.5 m, which provides a 2 ° beamwidth. At the maximum range (40 km), the spatial resolution is about 1.4 km. One inherent problem with mechanical dish antennas is the broadening beamwidth effect or beam smearing, which is produced when the samples comprising numerous pulses are collecting while the antenna is rotated [20]. In the case of WSR-88D the effective spatial resolution is about 40 % larger at the 3 RPM scan rates. In the case of phased array antennas, the beam is fixed during the time the samples are collected, so the smearing is not a concern anymore. Broadening beamwidth effect can also results of aperture projection with respect to beam position. This broadening beamwidth depends only on the scanning position. For example, for an X-band antenna with a beamwidth at broadside of 2 °, if the antenna is scanning in the azimuth plane about 20 ° the antenna beamwidth increases to $2.2°$ (6.4%); however, at $45°$ the beam broadens to $2.82°$ (40 %). This effect can considerably increase the spatial resolution of long-range radars.

2.6   Accuracy

In general the accuracy in a radar system is associated principally with: Signal to Noise ratio (S/N), bias errors in radar calibration, errors in propagation conditions, and errors from interference sources, such as radar clutter. All these factors, except for propagation conditions, are closely related to antenna performance. Large aperture antennas provide higher gain and more transmit power, which is important for improving the radar SNR, increasing the received dynamic range, improving minimum radar sensitivity, and allowing compensation for losses due to atmospheric attenuation. Large antennas enable narrower beamwidths, which is important for more

accurate estimation and detection of small scale events such tornados and mesocy-clones.

Low antenna sidelobes relative to the main beam are required to avoid side lobe collected energy contamination of the main beam. In severe storms, as tornados and heavy precipitation, the reflectivity values can vary between 20 to 60 dBZ, and large gradients can be produced. When this happens, the sidelobes can intercept large portions of the storm (with high reflectivity values), and the collected energy can contaminate the energy collected by the main beam. To minimize this effect, control of the sidelobes is required. One advantage of phased array radars is their flexibility in controlling the shape of the beam and sidelobes. Active phased array antennas can change the amplitude and phase of each element, and this provides the capability to control the sidelobes. Another important part of the radar system that affects radar accuracy is the performance of the radome under the influence of rain. Previous studies [21], [22], [23], [15] and [24] have demonstrated that high levels of uncertainty occur when the radar radome is wet. Attenuation, reflection and depolarization affect the radar signals. To mitigate the problem, radomes with hydrophobic and super-hydrophobic skin surfaces are currently required.

2.7 Cost

In any radar system the overall cost is influenced by a number of factors, the most important of which in this case are: a) user needs, b) technology, and c) quantity.

a) User needs: Different weather communities and the agencies have unique needs, and thus differing design, technology and cost requirements to satisfy specific de-mands. The National Oceanic and Atmospheric Administration (NOAA) and the National Weather Service (NWS) have operated an S-band, long-range radar net-work of 162 nodes to provide weather, hydrologic, and climate forecasts and warnings for the United States. The Department of Defense (DOD) relies on radar weather

surveillance for resource protection and military operational deployment. The Federal Highway Administration (FHWA) needs low-level radar coverage to provide safe and efficient transportation on the nation's roads and highways. The Atmospheric Radiation Measurement (ARM) Climate Research Facility of the Department of Energy (DoE) need radars systems at C,X, Ka, and W bands for the study of global climate change by the national and international research community. These are but a few examples of different needs, and all of them require different radar platforms, functionality and cost.

b) RF Technology: The evolution of RF technologies in the microwave spectrum has played an important role in the cost of radar systems, especially for phased array antennas that require several thousand active antenna elements. Emerging MMIC technologies capable of supporting higher RF power per unit area (for example GaNi) are providing higher levels of circuit integration [26]. Surface mount designs have enabled more affordable costs and lighter weight panels, suitable for low profile radar systems. Today GaAs MMIC chip-based T/R modules represent a mature technology that provides large quantities to satisfy the demands for modern X-band active phased array radars. In 2009 M/A-COM Technology Solutions released an X-band GaAs MMIC TR core chip fabricated with a 0.5-μm PHEMT technology. The CI cost is about \$100, and it operated in the 8.5 to 11 GHz range. The core chip consists of a 6-bit phase shifter, a 5-bit attenuator, an output driver amplifier, LNA, T/R switches, and digital control circuitry [27]. Another contribution of the technology is RF improvements using SiGe technology. Even though this technology does not provide the same RF performance as GaAs, SiGe provides better integration and functionality (digital and RF suitable for low power applications) than GaAs. The X-band, low-power, low cost phased array antenna developed by Raytheon [13] provides an example of higher integration of RF and logic functionality. Another important contribution of phased array technology is significant improvements in the

fabrication standards to provide more reliable components. In the past, conventional fighter radars have had Mean Time Before Failure (MTBF) durations of around 60 to 300 hours. Current technology in GaAs has increased MTBF to 1,000 hours [28]. This is a very important enhancement that increases the life cycle and reduces the operational and maintenance cost of phased array radars.

c) Quantity: Mass production is the key for reducing the cost of a phased array radar system, as in other technologies. For example, since the 1980s, the market for wireless devices has been growing at an unprecedented rate, and the rapid proliferation of wireless systems has brought the cost of a cell-phone to below $100. For phased array antennas, the cost of T\R modules are the main driver cost in the radar system. The CASA dense radar network is attractive for breaking down the cost of T\R modules since 10 thousand radars nodes require a very large production volume of RF components [29].

2.8 CASA radar requirements

In this section a set of specifications for the CASA phased array radar system is presented. The current IP1 radar system, the requirements of the radar community, and CASA end-user needs were all factors considered in the set of design specifications for the new radar system.

2.8.1 CASA IP1 radar system

The IP1 test bed (composed of 4 radars) developed within CASA [30] has demonstrated the application of networked radar operations for targeted applications. Each IP1 radar unit is placed in a triangular grid of 30 km (node-to node) and provides short-range radar of 40 km for each node, as illustrated in Figure 2.1. Each radar unit is based in a 1.2 m parabolic dish antenna to scan mechanically, which provides sector adaptive and overlapped coverage, a volume defined in 1 minute intervals

(called "heartbeats"). During each heartbeat interval, the radar performs a low-level 360 PPI surveillance suite at 2° elevation, followed by a multi-elevation PPI sector scan of between 60° to 120° with seven elevations (1°,3°,5°,7°,9°,11° and 14°), or 180° with four elevations only. The power source based in a magnetron provides a maximum power of 25 kW, a duty cycle of 0.15 %, and a maximum pulse length of 1 μs that yields a pulse repetition frequency of 1.5 kHz. The unambiguous radar range is larger than the radar range required. Yet this PRF provides a maximum unambiguous Doppler velocity of ±7.5 m/s that is insufficient for severe weather applications, where velocities occur typically in excess of ±25 m/s. In order to improve the maximum unambiguous Doppler velocity to up to ±38 m/s, a pulse width of 0.66 μs using two higher PRFs (1.6 kHz and 2.4 kHz) was implemented [31]. After splitting the transmitted power for each channel (H and V), and reducing the peak transmitted power to accommodate higher duty cycle PRF's, about 5 kW of transmitted power became available for each polarization channel respectively. For low-level 360 PPI surveillance suite at 2° elevation, the one pulse radar of the IP1 system provides a mean radar network sensitivity of 7.5 dBz, while at 14° elevation the mean radar sensitivity can be degraded 2 dB due to a larger range and a cone of silence over each radar. With 1.84° of half power antenna beam width, the mean spatial resolution is 340 m for low-level elevation (or 0.1 km altitude), and 740 m for a high-level elevation (or 4 km altitude).

2.8.2 CASA Phased array radar specifications

Based on basic needs and on the requirements of an IP1 radar network system, a radar analysis that includes the characteristics of phased array antennas is considered, contributing to the definition of a new set of radar specifications for a phased array radar system. Specifically, radar characteristics such as spatial resolution, minimum radar sensitivity, and bias differential reflectivity are considered in this analysis for
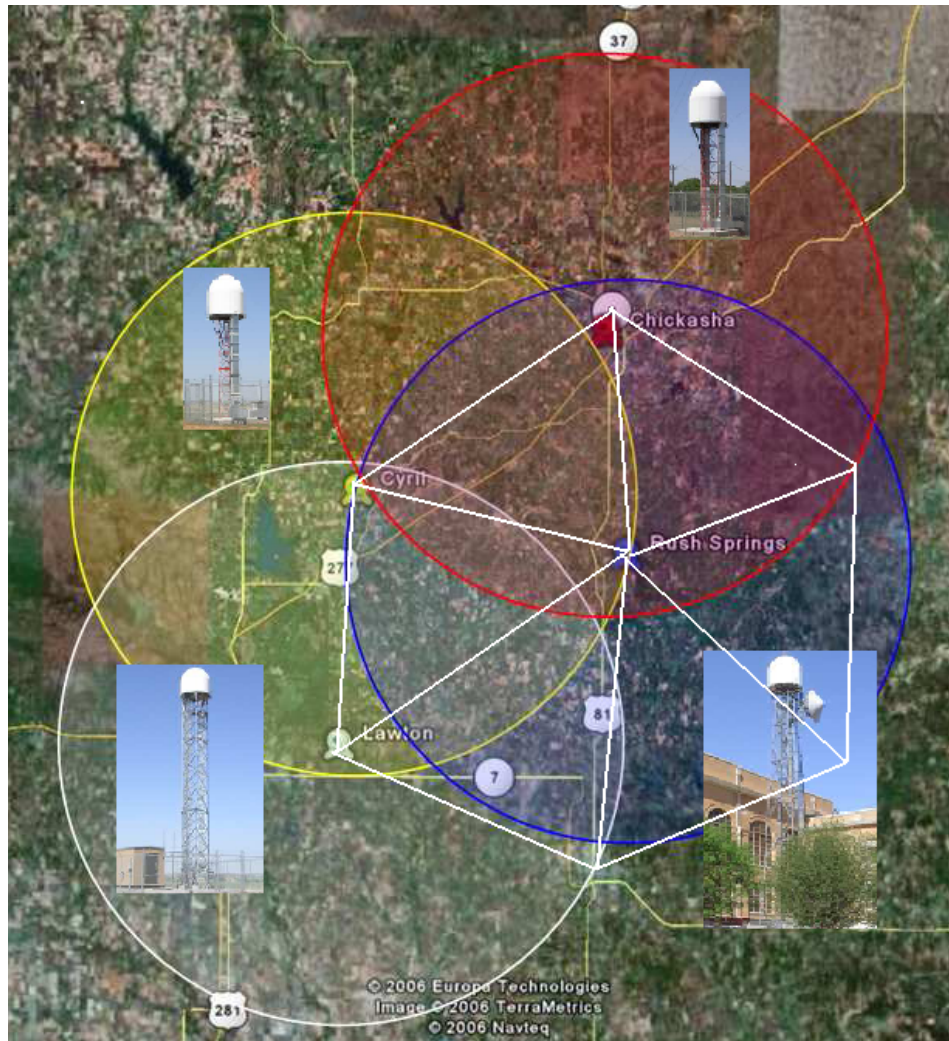
Figure 2.1. CASA IP1 weather radar network layout in triangular grid configuration [30].

different radar configuration nodes in a triangular radar grid, similar to the IP1 radar network grid.

CHAPTER 3

PHASED ARRAY ANTENNA DESIGN TRADE-OFFS FOR CASA RADAR NETWORK SYSTEM

3.1 Introduction

This chapter presents a trade-off analysis of key design parameters for electronically scanned phased array antennas as a single radar node and also as a radar system configured in a dense network. Results of azimuth resolution (A_{zr}), minimum radar sensitivity (Z_{min}), bias differential reflectivity (Z_{dr}^b), and integrated cross polarization (ICPR) were evaluated as a function of scanned array patterns. The dual-polarized scanned patterns consider different sidelobe distributions, errors induced in the antenna excitations and perturbations due the surface waves, mutual coupling and edge diffraction effects.

3.2 Initial set of requirements

A set of initial requirements for an IP1 radar network system, described in Table 3.1 were used a starting point for this analysis.

3.3 Radar node configurations

To provide equivalent radar coverage in the azimuth plane (0 ° to 360 °) using phased array antenna panels, at least three sectors must be considered since it is not practical to scan electronically beyond 120 ° or ± 60 ° from the broadside direction [35]. The problem of determining the optimum number of sectors for a multi-face planar array has been studied by Trunk [34] for the case when a single radar is considered

Table 3.1. Need-based radar performance attributes

Attributes	Desirable value
Operation frequency	Carrier frequency around 9.4 GHz ±60 MHz [3], [32].
Antenna beamwidth	Maximum half-power beamwidth of 1.8 °. [32]
Matched V & H antenna patterns	A pattern matched to within 5 % integrated power over the main lobe. [32]
Antenna max. sidelobe level	A maximum sidelobe gain of -25 dB when compared with main beam. [32]
Antenna cross-polarization isolation	A minimum cross-polarization isolation of 20 dB radar operating in alternate transmit and alternate receive mode. [41].
Radar sensitivity	A minimum detectable signal of 10 dBZ at 40 km in absence of precipitation, for single pulse of 600 ns duration. [32]
Radar maximum range	A range of at least 40 km. [3], [32]
Radar range in azimuth and elevation	A continuously scan 360 ° in azimuth and from -3 ° to 90 ° in elevation. [32]
Maximum bias in differential reflectivity	A maximum error of 0.2 dB, independent of any attenuation. [32]
Wind loading operation and survivability	The radar shall operate in condition of winds up to 60 mph, and wind gusts up to 90 mph [32]
Thermal regime	The radar shall be able to operate in a temperature range of 21° F to 140 °F. [32]
Radar weight	The maximum radar weight should not exceed 1200 lb per radar node. [33]
Radar cost target	The radar node cost should be less that $ 250,000. [3]

for the target tracking and surveillance problem. In such a case, either three or four planar sectors proves to be the optimum design (see Figure 3.1), depending on the specifics of the electrical properties of the antennas and the costs of the various components of the system. A trade-off radar analysis to evaluate the number of phased array panels needed in a radar node embedded in a CASA type network environment is discussed in [35]. This preliminary analysis addresses design trade-offs and seeks to define optimum system parameters (e.g., network topology, sector and antenna configuration) for a CASA dense radar network. The particular analysis investigated the degradation in the performance of a two-dimensional phased array radar as it scans away from the boresight direction, and the effects of scan loss, beamwidth broadening, gain loss and cross-polarization distortion in the radar measurement performance. The performance of the resolution cell area, the minimum measurement sensitivity, and polarization performance in various scenarios of planar phased arrays was evaluated in different configurations of a dense radar network. Three different topological and antenna-sector deployments in a triangular and rectangular radar network grid were considered. The number of antenna elements in the array (azimuth plane) was defined considering the maximum scanning range for each sector configuration. The results show that considering spatial resolution, radar sensitivity and polarization, the configuration with 6 sectors (each panel scanning 60 °or ±30 °) represents the best sector configuration in terms of performance. However, the high cost associated with 6 panels per node make this configuration complicated, expensive, and therefore impractical for implementation.

Considering cost constraints, the current analysis is focused on phased array antennas that perform electronic steering in a one dimensional plane, while the inexpensive mechanical positioner can be used in the other plane. Three radar configurations are considered in this analysis. The first one consists of a one dimensional phased array antenna that performs electronic scanning in the elevation plane, while a spinning
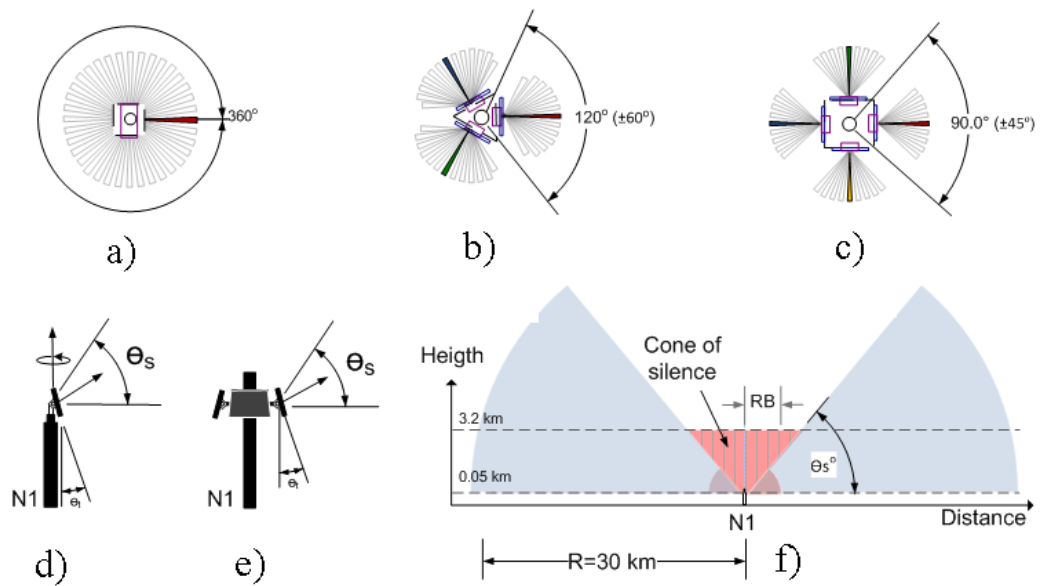
Figure 3.1. Representation of a single radar node configuration in azimuth scanning (top) for a) Spinning -Phase (SP) radar node configuration b) Phase-tilt radar node configuration with 3 sectors of 120° ±60° and c) Phase-tilt radar node configuration with 4 sectors of 90° ±45°, and in elevation plane (bottom) for d) SP e) PT3 and PT4 radar node.

pedestal can be used to scan in the azimuth plane. This configuration will be called Spinning-Phase, or SP for short. The second radar configuration consists of a a set of 3 phased array antenna panels that performs electronic scanning about 120° or ±60° in the azimuth plane, while a servo motor is used to perform mechanical scanning in the elevation plane. This configuration will be called Phase-tilt with 3 Sectors (PT3). The third radar node configuration consists of a set of 4 phased array antenna panels that performs electronically scanning about 90 ° or ±45 ° in the azimuth plane while a servo motor is used to perform mechanic scanning in the elevation plane. This configuration will be called Phase-tilt With 4 Sectors (PT4). A representation of the three radar configurations for a radar node in the azimuth and elevation plane is illustrated in the Figure 3.2.

3.4   Radar network grid

Similar to the IP1 radar network, a triangular grid with spacing between radars of about 30 km is considered for three radar node configuration alternatives (as illustrated in Figure 2.1). The radar range requirement is defined to 40 km in order to provide overlapped coverage and to compensate for the cone of silence in each radar node. Figure 3.2 (a-c) provides an illustration of the three radar node deployed in a triangular radar grid network. Figure 3.2 (d-e) illustrates the elevation setup of each radar node in a network environment to satisfy the 100% radar volume coverage at 3.2 km altitude.

3.5   Radar spatial resolution (SR)

The radar spatial resolution (SR), in terms of the radar range and beamwidth of the antenna, is expressed in the following equations:

$$SR(R, \theta_{3s}) = R \sin(\theta_{3s}) \tag{3.1}$$
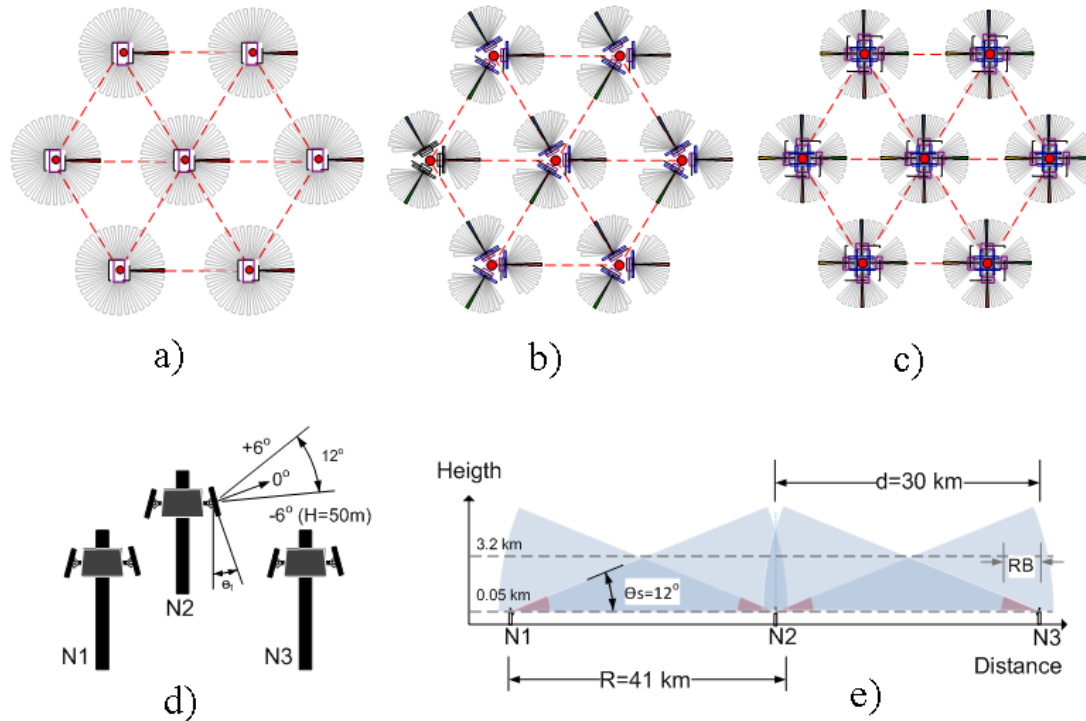
Figure 3.2. Representation of a radar nodes alternatives in a triangular radar network configuration. In the top for azimuth scanning for a) Spinning -Phase (SP) radar node configuration b) Phase-tilt radar node configuration with 3 sectors of 120 ° ±60 ° and c) Phase-tilt radar node configuration with 4 sectors of 90 ° ±45 °, and in elevation plane (bottom) for d) SP e) PT3 and PT4 radar node.

$$\theta_{3s} = \theta_{03}/cos(\theta_s) \qquad (3.2)$$

$$\theta_{03} = 0.886B_b\frac{\lambda_o}{L} \qquad (3.3)$$

where θ_{3s} represents the scanned half-power antenna beamwidth, and R is the radar range in kilometers. For electronically scanned planar array antennas, the beamwidth of the radiation pattern is not constant in angular space; it increases when the antenna beam is steered away from the broadside direction. The beamwidth θ_{3s} is defined in 3.2 where θ_{03} represents the antenna beamwidth at broadside, which is expressed in 3.3 in terms of a beam broadening factor (B_b), the free space wavelength (λ_o), and the length of the aperture antenna (L), assuming a linear array with no dependence on the elevation plane. [36]. Taking into consideration the broadening effect, for a 3 sector radar configuration, a reduction by a factor of 2 in antenna beamwidth is required to achieve the same mean radar resolution requirement. This requirement is difficult to satisfy since fully double the aperture size is needed, at a significant associated cost increment. The broadening beamwidth of phased array antennas is illustrated in Figure 3.3 (b and c) and quantified in Table 3.2. The radar node configuration SP does not suffer any degradation in the azimuth plane since the beamwidth is steered mechanically, and likewise only small degradation occurs in elevation since the scanning range is only 12 ° (±6 °). In any of the three configurations, a cone of silence with a radius of 15 km at 3.2 km altitude is observed, since a 12 ° scanning range is required to achieve coverage at 3.2 km altitude. This limits the radar coverage percentage to 86 %. To overcome this gap in coverage, a scanning range in the elevation plane of 90 ° (±45 °) is required. Table 3.2 shows the spatial resolution for all radar configurations. For a PT3 radar configurations, the mean spatial resolution is degraded by 25 % with respect to the SP, and by 14 % is degraded for a PT4 with respect to the SP radar configuration.
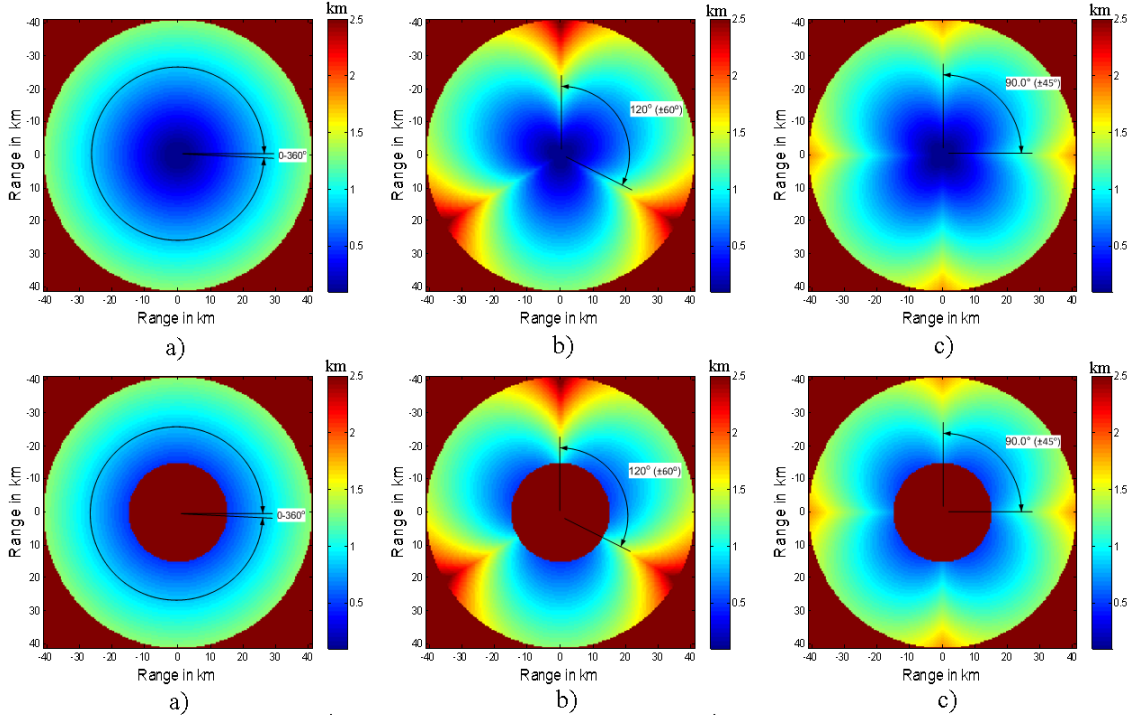
Figure 3.3. Spatial resolution at azimuth plane for a single radar node at 50m altitude in the top and at 3.2 km altitude in the bottom for a) Spinning radar (SP) b) Phase-tilt with 3 sectors (PT3) and c) phase-tilt wit 4 sectors (PT4)

Table 3.2. Spatial resolution in azimuth plane for radar nodes: Spin Phased-array (SP), Phase-tilt 3 sectors (PT3) and for Phase-tilt 4 sectors (PT4). All values in km

Spatial Resolution (SR) for a single radar node				
Config.	Altitude	Max	Median	Mean
SP (1 panel)	0.05	1.3	0.94	0.88
	3.2	1.3	1.0	0.97
PT3 (3 panels of 120°)	0.05	2.6	1.1	1.10
	3.2	2.6	1.2	1.20
PT4(4 panels of 90°)	0.05	1.8	1.1	0.90
	3.2	1.8	1.1	1.10
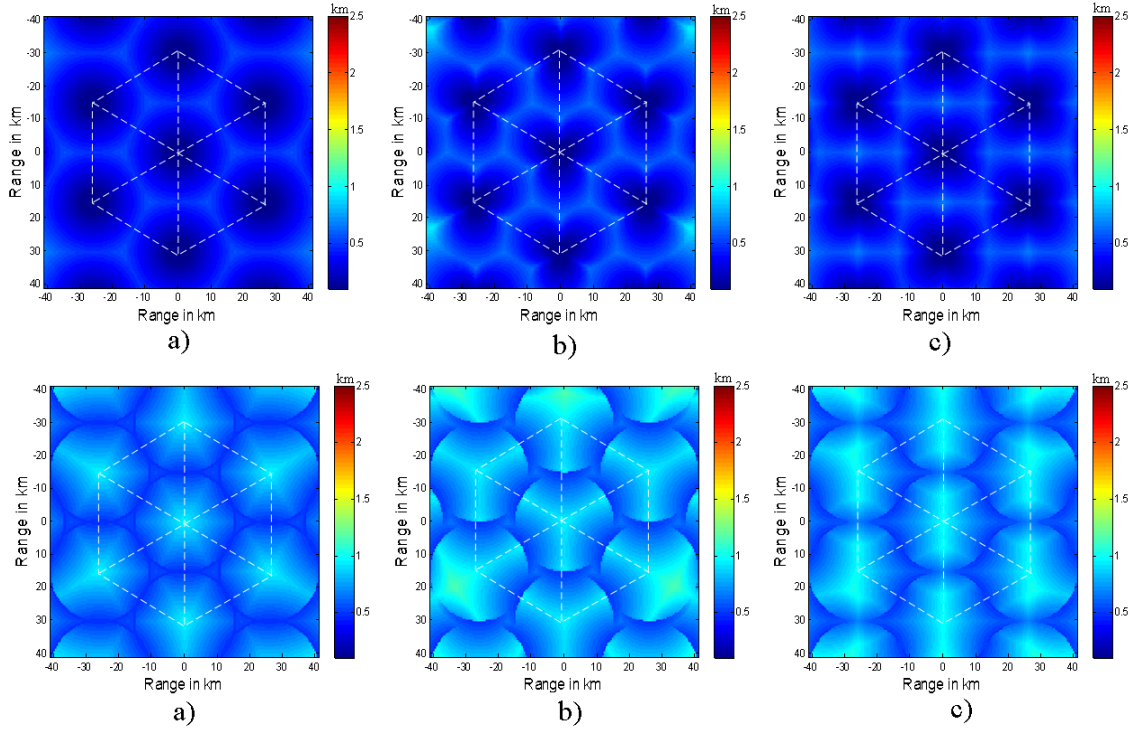
Figure 3.4. Spatial resolution at azimuth plane for a triagular radar at 50m altitude and at 3.2 km altitude for a: Spinning radar (SP), Phase-tilt with 3 sectors (PT3) and phase-tilt wit 4 sectors (PT4)

Figure 3.4 shows the spatial resolution for the 3 radar configuration deployed in a triangular network grid. As expected, for the three radar node configurations, the overlapped coverage in a network environment improves the mean spatial resolution with respect to a single radar node. An improvement factor of about 2.5 in the mean spatial resolution is observed for a radar network deployed at low altitude (0.05 km), and an improvement factor of about 1.5 is observed when deployed at low altitude (3.2 km) for all radar configurations. Table 3.3 presents the spatial resolution of the three radar configuration for an altitude of 0.05 km and 3.2 km. A small variation between the 3 and 4 sector radar nodes as compared to the SP radar configuration is observed.

Table 3.3. Spatial resolution in azimuth plane for radar nodes: Spin Phased-array (SP), Phase-tilt 3 sectors (PT3) and for Phase-tilt 4 sectors (PT4). All of them in a trianlgular network grid of 30 km. All values in km

Spatial Resolution (SR) for a network radar system				
Config.	Altitude	Max	Median	Mean
SP (1 panel)	0.05	0.97	0.37	0.35
	3.2	0.97	0.65	0.66
PT3 (3 panels of 120°)	0.05	0.96	0.44	0.42
	3.2	1.20	0.77	0.76
PT4(4 panels of 90°)	0.05	0.99	0.41	0.39
	3.2	1.10	0.72	0.73

3.6   Minimum radar reflectivity ($\mathbf{Z}_{min}$)

Another important radar parameter used to define the phased array radar specification is the minimum radar reflectivity Z_{min} (mm^6m^3). The minimum radar sensitivity can be expressed by 4.34 [20]. In the case of phased array antennas, the gain and beamwidth is dependent on angular position (θ_s). The antenna beamwidth in the azimuth plane is expressed by (3.2). The other parameters in 3.4 are described in Table 3.4.

$$Z_{min}(R, \theta_s) = \frac{CP_{min}R^2\lambda^2 L}{P_t G^2(\theta_s)\tau\theta_3(\theta_s)\phi_3|K_w{}^2|}SNR \tag{3.4}$$

The expression of the total gain as function of the antenna gain scan loss is represented by 3.5, [50].

$$G(\theta_s) = \frac{4\pi d_x d_y N_x N_y}{\lambda^2}[1 - |\Gamma(\theta_s)^2|]\cos(\theta) \tag{3.5}$$

where, dx and dy represent the unit cell dimensions of the antenna elements on the array, Nx and Ny are the total number of elements in the array in the x (azimuth) and y (elevation) dimensions. $\Gamma(\theta_s)$ represents the active reflection coefficient of the active element which changes as a function of the beam position. The gain scanloss is represented by $(1 - |\Gamma(\theta_s)^2|)\cos(\theta)$ and can be approximated $cos(\theta)^{1.2}$ for practical considerations [36]. To illustrate the effect of gain loss and broadening

effect in a phased array for the minimum radar reflectivity, a set of radar parameters similar to those for the IP1 radar system were used (see Table 3.4). In this case, pulse compression techniques using modulated long pulses have been used to improve sensitivity and achieve range resolution similar to that of a short pulse [37]. Longer pulses using compression techniques bring an inherent problem of not receiving signal for the duration of the time while the radar is transmitting. In order to overcome this problem, a second short pulse is required to cover the blind region of the first long pulse, keeping in consideration that the blindness region due to the second pulse must be small enough to compromise the radar coverage initially specified. Table 3.4 provides information about the set of design requirements for the IP1 radar nodes (left) in comparison with the phased array solid state radar (right).

Table 3.4. Radar system parameters for IP1 and Phase-tilt radar system in a network enviroment.

Parameter	Sym	IP1	Phase-tilt
Frequency	f	9.4 GHz $\pm$ 30 MHz	9.36 GHz $\pm$50MHz
Peak Tx. power	P_t	5 KW	50 W
Beamwidth (Azim)	θ_3	1.8°	1.8° to 2.5°
Beamwidth (Elev)	ϕ_3	1.8°	3.6°
Scaning range (Azim.)	$\Delta\theta$	0° -360°	120°($\pm$60°), 90°($\pm$45°)
Scaning range (Elev)	$\Delta\phi$	0° -12°	0° -12°($\pm$6°)
Noise Figure	NF	5.5 dB	4.5 dB
Gain (Broadside)	G	36 dB	38d B
Maximum radar range	R	40 km	40 km
Range resolution	Δ_r	100 m	50m - 100m
Antenna bandwidth	BW	30 MHz	50 MHz
Pulse repetition freq.	PRF	1.6 - 2.4 KHz	2.4 KHz
System loss	L	2.5 dB	2.0 dB
Pulse width	τ	0.66 μs	3.33 μs, 40 μs
Radar constant	C	2.5x10^{26}	2.5x10^{26}
Min. Detectable signal	P_{min}	-103.6 dBm@3 MHz	-103.6 dBm@1.5 MHz

Figure 3.5 illustrates the radar sensitivity of a single radar node for the three radar node configuration discussed previously for low (0.05 km) and highest (3.2 km)
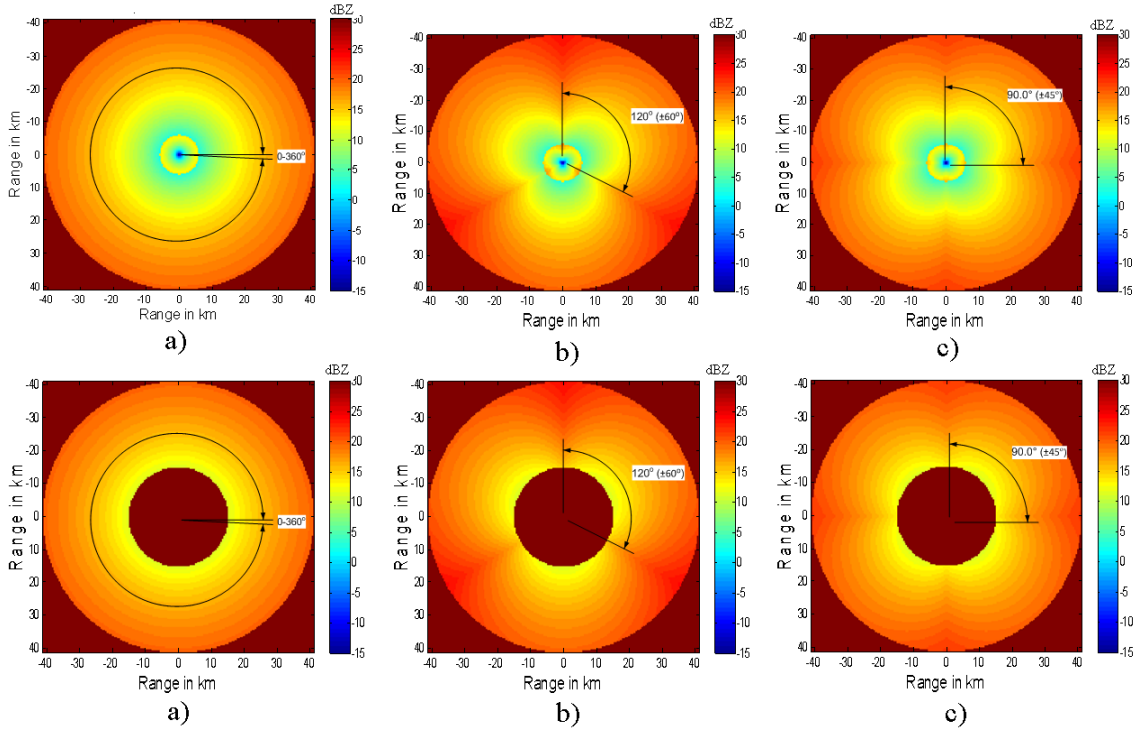
Figure 3.5. Minimum radar sensitivity at azimuth plane for a single radar node at 50 m altitude in the top and at 3.2 km altitude in the botom for Spinning radar (SP) Phase-tilt with 3 sectors (PT3) and phase-tilt wit 4 sectors (PT4). P$_{min}$=-107 dBm, NF=4.5 dB, t$_1$=3.33 μs, t$_2$=40 μs, BW=3 MHz, PCG$_2$=21 dB, Pt=50 W (peak), G=38 dB.

Table 3.5. Minimum radar sensitivity (Z$_{min}$) in azimuth plane for radar nodes: IP1 radar (IP1), Spin Phased-array (SP), Phase-tilt 3 sectors (PT3) and for Phase-tilt 4 sectors (PT4).

Minimum radar sensitivity (Z$_{min}$) for a single radar system				
Config.	Altitude(km)	Max(dBZ)	Median (dBZ)	Mean (dBZ)
SP (1 panel)	0.05	19.7	16.7	15.6
	3.2	19.8	17.3	16.8
PT3 (3 panels of 120°)	0.05	23.8	17.8	16.9
	3.2	23.9	18.4	18.0
PT4(4 panels of 90°)	0.05	21.7	17.3	16.3
	3.2	21.7	17.9	17.4
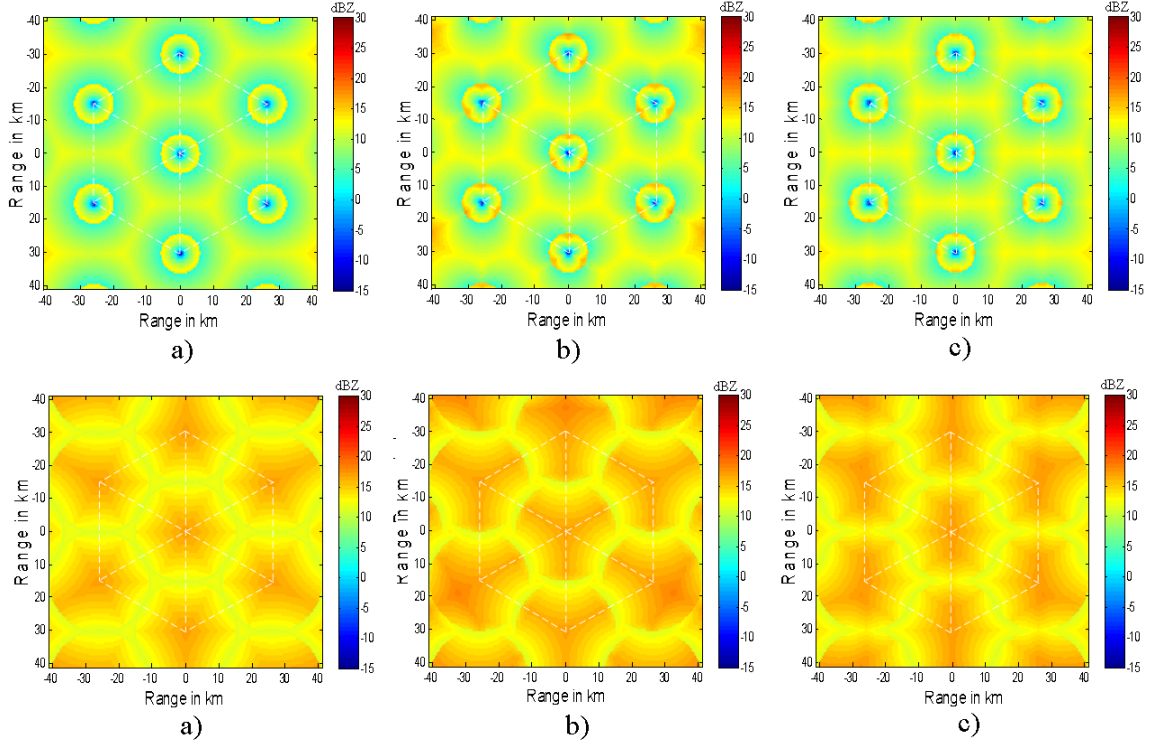
Figure 3.6. Minimum radar sensitivity (Z_{min}) at azimuth plane for a triangular radar at 50 m altitude and at 3.2 km altitude for a: Spinning radar (SP), Phase-tilt with 3 sectors (PT3) and phase-tilt wit 4 sectors (PT4). P_{min}=-107 dBm, NF=4.5 dB, t_1=3.33 μs, t_2=40 μs, BW=3 MHz, PCG_2=21 dB, Pt=50 W (peak), G=38 dB.

altitude. Maximum, median and mean values are summarized in the Table 3.5 . Results show that for a single radar system, even for transmit power equivalent to an IP1 radar system, the mean value of minimum radar sensitivity is higher than 16 dBz. However, when any of those radar nodes is deployed in a regular triangular radar grid (see Figure 3.6), the minimum radar sensitivity improves by 7 dB for lower altitudes and to 3 dB for higher altitudes for the three radar configurations.

Figure 3.7 illustrates the case of minimum radar sensitivity in a triangular radar network with a PT4 radar node configuration versus the peak transmit power for different lengths of the pulse width. In the lowest altitude (0.05 km) and in the right

Table 3.6. Minimum radar sensitivity (Z_{min}) in azimuth plane for radar nodes: Spin Phased-array (SP), Phase-tilt 3 sectors (PT3) and for Phase-tilt 4 sectors (PT4). All of them in a triangular network grid of 30 km. All values in dBZ

Minimum radar sensitivity (Z_{min}) for a network radar system				
Config.	Altitude(km)	Max(dBZ)	Median (dBZ)	Mean (dBZ)
SP (1 panel)	0.05	17.0	9.29	8.81
	3.2	17.1	13.7	13.8
PT3 (3 panels of 120°)	0.05	17.8	10.4	9.90
	3.2	18.3	14.8	14.6
PT4(4 panels of 90°)	0.05	17.2	9.89	9.41
	3.2	17.5	14.2	14.3

for the highest altitude (3.2 km) . Other radar node configurations are not considered since the difference between radar nodes is less 1 dB.

Using the current average transmit peak power of 5 kW for IP1 radars, the curves (in black) show a mean radar sensitivity in the overall domain at the 6.5 dBZ for lower altitude (~50 m), while at 3.2 km altitude the mean radar sensitivity is about 9.1 dBZ. The degradation in sensitivity at high altitudes due to the cone of silent volume occurring at the maximum scanning elevation of 12° is covered by the adjacent radar nodes (see Figure 3.2). Figure 3.2 shows that achieving equivalent mean radar sensitivity using the array antenna and using an equivalent range resolution, or better, requires longer chirp pulses of 40 μs and 3.3 μs with the radars transmitting 110 W peak power. A second chirp pulse of 3.3 μs is also considered in order to mitigate the blind region (of about 6 km) generated for the first long pulse. Increasing the pulse width more that 40 μs does not represent any gain in radar sensitivity because the sensitivity in the larger blindness region (~7.5 km), which is covered by the second and short pulse (of 3.3 μs), is deteriorated since this area increases when the longer pulse is increased. Large blindness regions not only limit the coverage near the radar, they
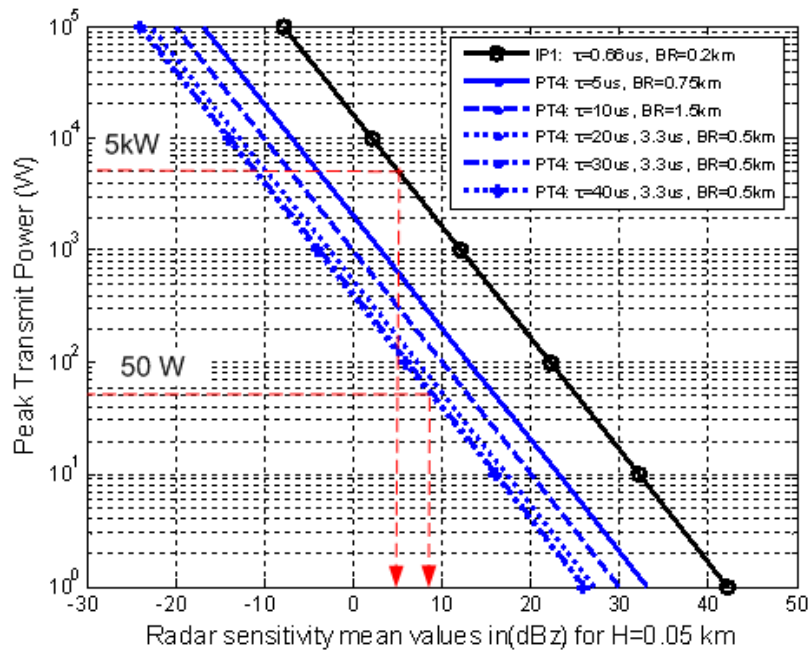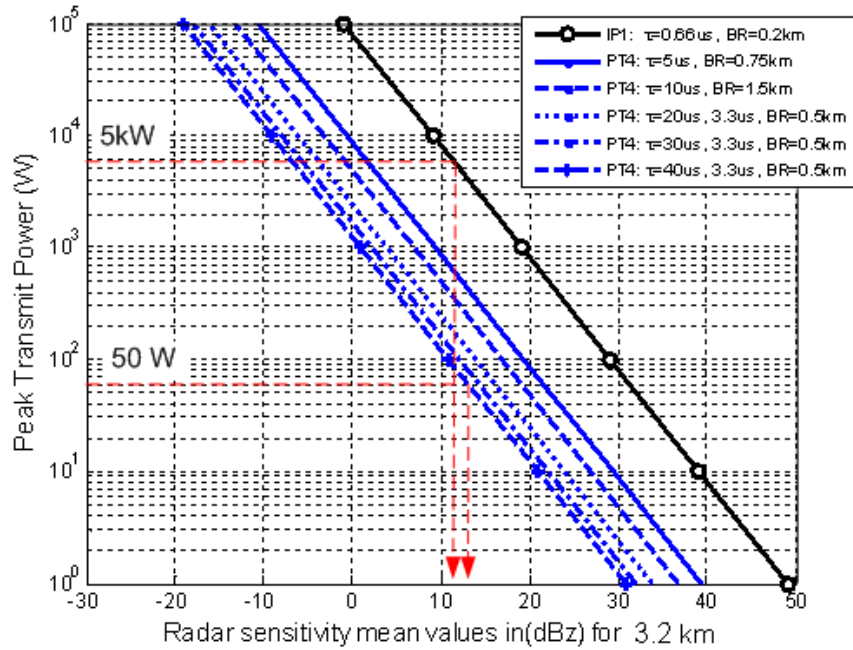
Figure 3.7. Mininimun radar sensitivity (mean values) for PT4 radar node deployed in a trangular grid radar network for: a) lowest altitude(50 m) and b) highest altitude (3.2 km) for $\tau_o = 5\mu s, 10\mu s, 20\mu s, 30\mu s$, and $40\mu s$

also might introduce bias errors in polarimetric variables due to a lack of information in the differential phase that is used for attenuation correction in X-band [40].

3.7 Dual-polarization

This section provides a discussion of the minimum requirements of the CASA phased array antenna to perform polarimetric weather measurement. Two important design considerations commonly used for conventional polarimetric radars (based on parabolic antennas) are taken into account as a starting point to define a new set of design requirements for a dual polarized phased array in a CASA radar network system. These design considerations are:

a) The antenna shall have H and V polarization patterns matched to within 5 % integrated power over the main lobe [32].

b) The radar node antenna shall have a minimum polarization isolation of -20 dB when the radar operates in Alternative Transmit and Alternate Receive (ATAR) to estimate precipitation within ±0.2 dB accuracy [41].

These two requirements are difficult to satisfy in any electronically steered array antenna since the antenna patterns (co-polar and cross-polar and for H and V) change in shape with beam position. Mutual coupling, surface waves, and other effects such as field diffractions at the edges of the antenna array are some of the causes of antenna pattern distortion.

This section presents an analysis of how two polarimetric variables, the differential reflectivity (Z_{dr}) and the linear depolarization ratio (LDR), can be affected by mismatch in co-polar patterns and cross-polarization as a function of beam position in the antenna array.

The approach to evaluate the radar polarimetric was adopted from [40], [42] and [42]. It assumes a measurement of a uniformly filled volume with identically spherical scatters, given the power patterns of the antenna. In this case any measured values

of Z_{dr} and LDR that deviate from ideal would be indicative of the error caused by the antenna only. For such a simulation, Z_{dr} represents the differential reflectivity bias error (Z_{dr}^b), and LDR is called the integrated cross- polarization ratio ($ICPR$) [43].

Bias in the Z_{dr} can also be affected by the type of precipitation and the antenna field projections with respect to the target. The effect of the precipitation media was evaluated and characterized by [41], and the effect of the projection of the fields of the target and and ideal antenna is evaluated by [44], [45]. In this section we focus on the effect of mismatch in antenna patterns and cross-polarization isolation with scanning in the Z_{dr} and $ICPR_2$ due to the effects of the antenna design and performance, since this effect was not studied before. The expression of the Z_{dr}^b and for the $ICPR_2$ in 3.6 and 3.7 are modified to distinguish the patterns in transmission and reception. This modification is needed due to of the possibility that the beam shape can change independently for the transmission and reception mode, respectively, in phased array antennas:

$$Z_{dr}^b = 10 \log_{10} \left(\frac{\int \int \mid F_{Hc_T} F_{Hc_R} + F_{Hx_T} F_{Hx_R} \mid^2 d\Omega}{\int \int \mid F_{Vc_T} F_{Vc_R} + F_{Vx_T} F_{Vx_R} \mid^2 d\Omega} \right) \tag{3.6}$$

$$ICPR_2 = 10 \log_{10} \left(\frac{\int \int \mid F_{Hc_T} \ F_{Hc_R} \ F_{Hx_T} \ F_{Hx_R} \mid d\Omega}{\int \int \mid F_{Hc_T} \ F_{Hc_R} \mid^2 d\Omega} \right) \tag{3.7}$$

where F_{Hc_T}, F_{Hc_R}, F_{Vc_T} and F_{Vc_R} are the antenna co-polar patterns for H and V, and F_{Hx_T}, F_{Hx_R}, F_{Vx_T} and F_{Vx_R} represent the cross-polar patterns for H and V, both in transmission and reception, respectively. and the $d\Omega$ is the element of solid angle $d\Omega = \sin \theta \ d\theta \ d\phi$

3.7.1   Antenna array patterns

The expressions in 3.8 and 3.9 represent the one dimensional scanning array far-field antenna patterns. The electric field is written in terms of the antenna element

patterns for each element in the presence of the whole array ($\overrightarrow{f}_{en}$) and the coefficients (A_n) that represent the excitations (voltages or currents) of each individual antenna element in the array:

$$\overrightarrow{E}(r,\theta,\phi) = k\frac{e^{-jkr}}{r}\sum_{n=1}^{N}\overrightarrow{f}_{en}(\theta,\phi)A_n e^{j(n)kd(\sin\theta-\sin\theta_s)} \tag{3.8}$$

where $k = 2\pi/\lambda_\circ$ and d is the inter-element distance in the array. Considering that the antenna pattern is typically measured on a sphere of constant radius, the factor $k\frac{e^{-jkr}}{r}$ is just a normalizing constant. So the antenna pattern in the expression 3.8 now is only dependent on angle:

$$\overrightarrow{E}(r,\theta,\phi) = \overrightarrow{F}(\theta,\phi)\frac{e^{-jk_o r}}{r} \tag{3.9}$$

$$F(\theta,\phi) = \sum_{n=1}^{N}\overrightarrow{f}_{en}(\theta,\phi)A_n \, e^{j(n)kd(\sin\theta-\sin\theta_s)} \tag{3.10}$$

3.7.1.1   Antenna element patterns

In general, the element patterns are different for each element in the array, even for an array of like elements with uniform spacing; the differences are attributed to the interaction between elements or mutual coupling, and also by the diffracted field near the array edges. For one isolated microstrip patch antenna element, the co-polar radiation patterns for E and H planes are not the same. Typically the antenna element pattern in the E-plane are broader than in the H-plane, due to the interaction of the fields with the ground plane. When the element pattern is taken in an array environment, the presence of mutual coupling, surfaces waves, and edge effects can change the shapes of the antenna element patterns, which also can cause a mismatch in array antenna patterns, and as consequence introduce uncertainties in the measurement of the Z_{dr}. Figure 3.8 illustrates three examples of antenna

element patterns in three different circumstances. Figure 3.8 a) represents the case of a isolated antenna element using an infinite ground plane. In this particular case the element pattern roll-off in H can be represented by $\cos\theta^{0.8}$, and the antenna pattern roll-off in V polarization can be represented by $\cos\theta^{1.4}$. Figure 3.8 b) Represents the case of the antenna element patterns embedded in a linear array of 18 elements in an infinite ground plane. The center element (9th) is excited, and the others are perfectly matched. In this case, it seems that the interaction of the center element and the others in the array somewhat improves the matching in the co-polar patterns. Figure 3.8 c) shows an example of ripples produced in the dual-polarized antenna element excited in horizontal polarization. For this particular case the embedded element pattern (in an array of 18x1 elements) uses a finite ground plane, where the distance from the last element is less than $1\lambda_\circ$ in the azimuth plane. The surfaces waves and mutual coupling (stronger in H polarization) antenna reaches the borders of the antenna and the energy diffracted produces ripples in the element pattern. This effect is not visualized in the elevation plane since the ground plane is extended to infinity and the edge effect has low impact in vertical polarized fields in the azimuth plane.

3.7.1.2   Mutual coupling, surface waves and edge effects

Mutual coupling is attributed to the fields that exist along the air and antenna substrate interface. When high levels of coupling exist between elements in the array, those can produce gain variation, increase the sidelobe, degrade the cross-polarization, fill and shifted nulls and array blindness at some scan angles [46]. In a microstrip patch antenna array, typically the mutual coupling is a function of the relative alignment and spacing between elements. For example, in a linear array antenna, stronger mutual coupling is expected in the direction where the electric fields are collinear to the plane where the elements are placed. In a planar array of dual polarized antenna elements, the electric field for H-polarization is collinear to the azimuth plane, so
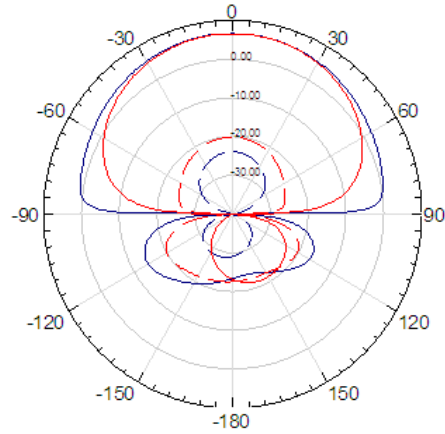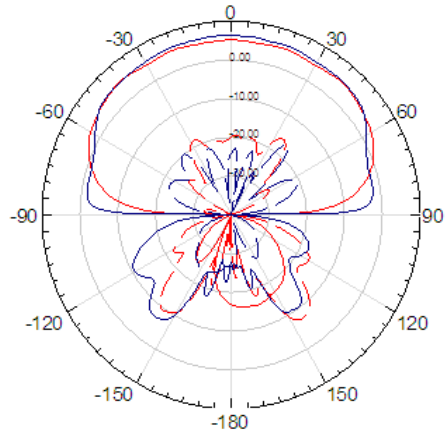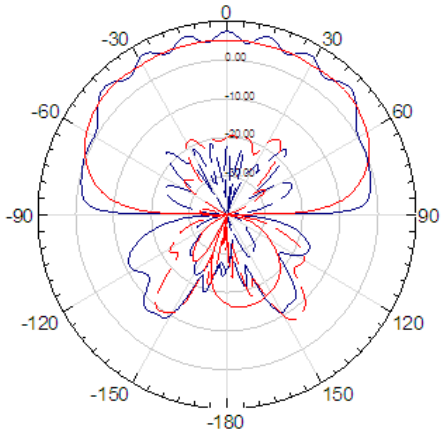
Figure 3.8. Antenna element patterns for H (in red) and V polarization (in blue) for a) Isolated antenna element in a infinite ground plane b) Embedded center element in a linear array of 18x1 elements in azimuth plane with infinite ground plane and c) Embedded center element in a linear array of 18x1 elements in azimuth plane with finite ground plane in the azimuth plane an infinite ground plane in the elevation plane.

larger mutual coupling is expected in this direction. When element spacing in the array is about $\lambda_\circ/2$, mutual coupling should not cause significant degradation in the antenna patterns [46]. Large antenna element spacing can help to reduce the coupling between elements. However, element spacing larger than $\lambda_\circ/2$ limits the scanning aperture, due to the presence of grating lobes.

Surface waves are modes of propagation supported by grounded dielectric substrates. When the antenna array supports surface waves, these propagate in the substrate until they reach the edges, where they can be diffracted and reflected, perturbing the radiation patterns with undesirable ripples. Surface waves are excited when a high dielectric constant or thick substrates are considered in the array design. Stacked substrates with mixed dielectric constants are typically used for applications where large impedance and gain bandwidth are required [47]. Those designs require of careful considerations in order to suppress possible surface waves, and in general increase the fabrication complexity and the cost of the antenna. Satisfying the condition suggested by Pozar and Schaubert in [48] offers one simple criterion to avoid excitations of surface waves in printed scanned array antennas. Where t is the thickness and ε_r is the effective dielectric constant of the antenna substrate:

$$t < \lambda_\circ/(4\sqrt{\varepsilon_r - 1}) \qquad (3.11)$$

One additional design consideration used to minimize the effect of diffraction waves and reflections at the edges of the antenna consists of extending the ground plane about $5\lambda_\circ$ from the array. This distance makes the diffracted fields below -40 dB [46]. Another practical solution to minimize the diffraction at the edges of the antenna is adding 2 or 3 additional antenna elements to operate as dummy antenna elements.

Geometrical Theory of Diffractions (GTD) techniques have been used to predict the diffractions of surfaces waves in ground planes or substrates [51] and [52]. Here, we do not use those techniques to characterize the ripples in the element patterns. Instead, a simpler approach to model ripples in the embedded element pattern consists in using the following expressions 3.12 and 3.13.

$$f_{e-h} = \cos(\theta)^{n_h} + \xi_h \cos(\theta N + \beta_h) \qquad (3.12)$$

$$f_{e-v} = \cos(\theta)^{n_v} + \xi_v \cos(\theta N + \beta_v) \qquad (3.13)$$

In both expressions the first part $\cos(\theta)^n$ represents the co-polar antenna pattern, where n_h and n_v are values that define the roll-off element patterns for H and V. The exponent values of n_h and n_v are values that can vary from 0.8 to 2.0 and give the roll-off characteristics of the antenna element patterns. The second term $\xi_h \cos(\theta N + \beta_h)$ represents the ripples over the embedded antenna element pattern, where ξ_h and ξ_v represent the amplitude of the ripples. N is the number of elements, and β_h and β_v represent the phases of the center element with respect to the edge of the array.

Figure 3.9 illustrates 4 cases of the antenna element patterns embedded in an planar of 18x18 elements, and with spacing of $0.53\lambda_\circ$ in both planes. For all cases we assume the same roll-off patterns of $f_{e-h}=\cos(\theta)^{0.8}$ and $f_{e-v}=\cos(\theta)^{1.6}$ and the ripples can be modeled using the expressions in 3.12 and 3.13.

We illustrate 4 cases. Case a Corresponds to the ideal case where ripples are not affecting the embedded element patterns. For this case we use $\xi_h=\xi_v=0$. Case b represents the case where the co-polar patterns for H are affected by ripples. This can happen when the surface waves and mutual coupling are controlled in the elevation plane and not in the azimuth plane. Case c represents the case where surface waves and mutual coupling are present in the azimuth and elevation plane. In this particular

case we assume that the antenna elements are symmetric in both planes, so differences in the excitation phase for H and V are zero ($\Delta\beta=0$). In this circumstance the induced phases of the possible surface waves can create ripples where the peak and nulls can also be in phase ($\beta_h = \beta_v$). Case d is similar to case c, the difference being that $\beta_h \neq \beta_h$.When this happen the peaks and the nulls of the ripples are not in same position and the large amplitude difference in the ripple amplitude (H and V) can produce a large bias in Z_{dr}. The worst case scenario will happen when $\Delta\beta =90$ °. This scenario is illustrated in the Figure 3.9 d

Figure 3.10 a) shows the effect of the mismatch in an array patterns of 18x18 elements (in the azimuth plane) based on the element patterns not effected by the ripples. It assumes a roll-off constant pattern for H-polarization ($n_h=0.8$) and a range in n_v between 0.9 and 1.6 for the vertical element pattern. The bias in Z_{dr} was estimated using 3.6 assuming no contamination of the cross-polar components ($F_{Hx}=F_{Vx}=0$). It indicates that, for measuring Z_{dr} with an accuracy of ±0.2 dB, the ratio between the roll-off element constants (n_v/ n_h) needs to be less than 1.1. Figure 3.10 b) shows the mismatch percentage of the two-way beam pattern for H and V.

Figure 3.11 a) shows the estimated bias in the Z_{dr} versus scanning angle, considering ripples in the embedded element pattern in the the azimuth plane (only). The antenna array of 18x18 elements, and ripples with amplitudes of 0.5 dB, 1 dB and 2 dB are considered. The ripples were modeled based on the expression 3.12 and 3.13 using for $n_h=0.8$, $n_v=1.6$, and for different ripples amplitudes $\xi_h=0$, $0.025, 0.05$ and 0.1. $\xi_v=0$. In b) we assume the case of having ripples with the same magnitude $\xi_h=\xi_v=0.1$ (for 2 dB) in both planes. The curve in black represents the ideal case where no ripples are in the embedded element patterns. The curve in blue represents the case where the surface waves reach the border of the antenna with the same phase ($\Delta\beta=0°$). In this case, the minimum effect of the ripples as the bias Z_{dr} is observed, since the nulls and peaks are relatively in the same place. The curve in red represents
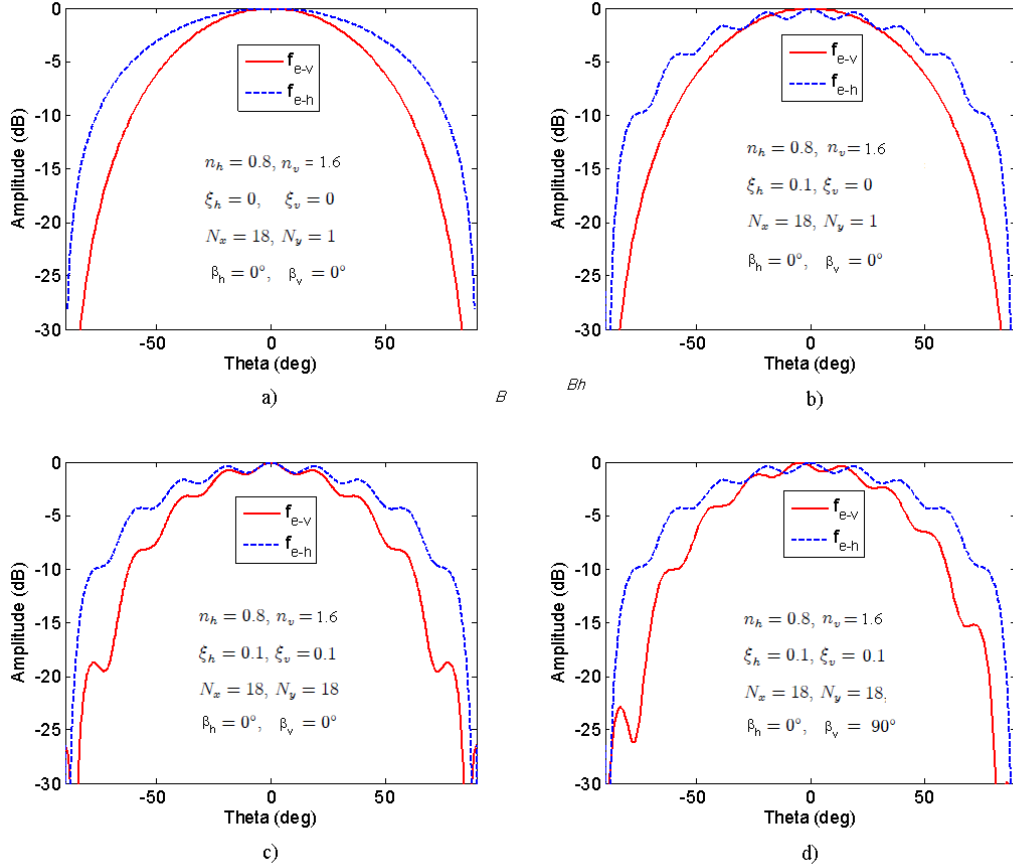
Figure 3.9. Representation of embedded element pattern in a planar array environment. a) Represents the ideal case where no mutual coupling and surface waves are present in the array and also a infinite ground plane is considered; b) Represents the case mutual coupling an surface waves in the array are diffracted in the edges where finite ground plane is considered; c) Represents the case where the ripples produced by the mutual coupling and surfaces waves and diffracted fields at both edges of the array can produce ripples in H and V patterns, the phase of ripples in H and V are in phase; and d) Similarly to c) with the difference being that the ripples are not in phase.
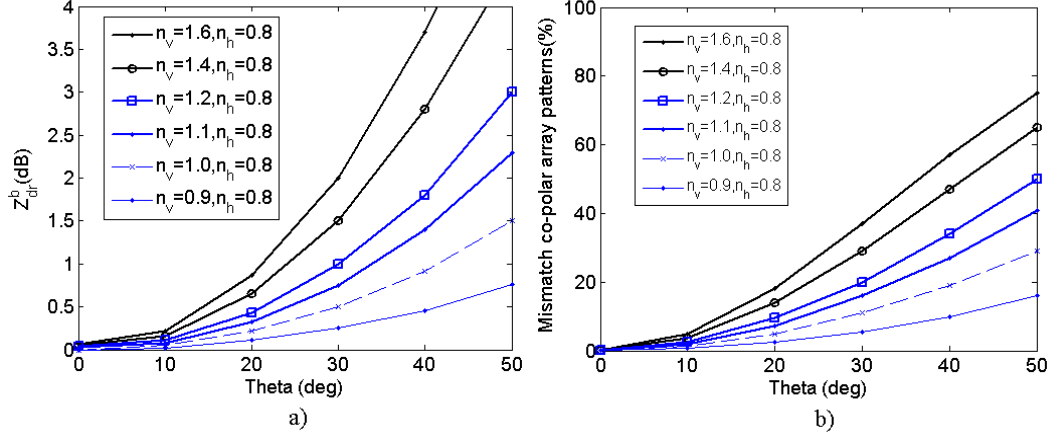
Figure 3.10. a) Bias in Z_{dr} versus scanning angle (in azimuth plane) due the mismatch of the co-polar antenna patterns for H and V based on element patterns without ripples b) Mismatch percentage of co-polar antenna patterns in H and V of an array of 18x18 as a function of scanning angle in the azimuth plane.
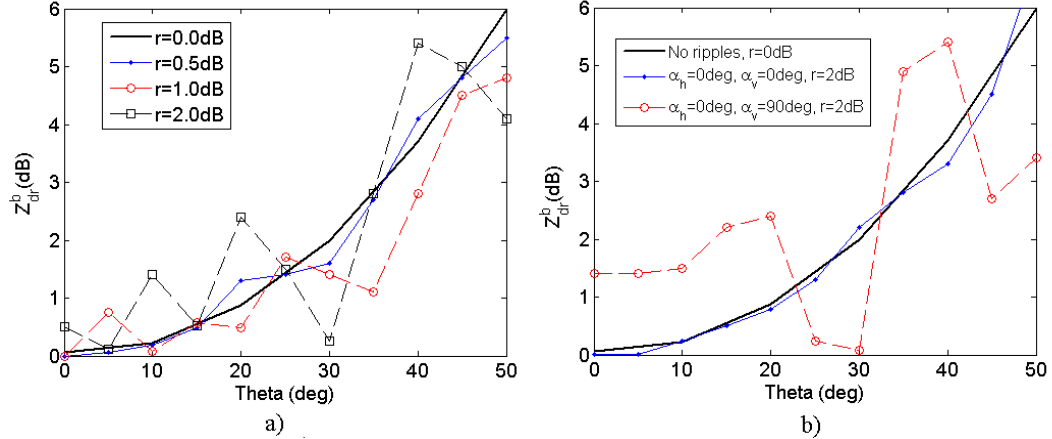
Figure 3.11. a) Bias in the Z_{dr} versus scanning angle considering ripples of 0.5 dB, 1dB and 2 dB. where the ripples were modeled using the equations 3.12 and 3.13, for n_h=0.8 n_v=1.6, ξv=0, and α_h=α_v=0. in an array of 18x18 elements (finite ground plane in azimuth plane only). b) Bias in the Z_{dr} versus scanning angle considering ripples of 2 dB where n_h=0.8 n_v=1.6, ξv=ξv=0.1(2dB) and $\Delta\alpha$=0°.(in phase), $\Delta\alpha$=90°(out of phase) in an array of 18x18 elements.

the case where the surface waves reach the border of the antenna in different phase $(\Delta\beta \neq 0°)$. In this case the red curve represent the worst case scenario when the nulls and peaks for H and V patterns are opposite.

3.7.1.3 Cross-polarization

The polarization performance of a phased array antenna principally depends on the polarization characteristics of the antenna element embedded in the antenna array. Mutual coupling, surface waves and diffraction at the antenna edges can also affect the cross-polarization performance, however those can be significantly less compared to the antenna element performance. One additional contributor of degradation of cross-polarization performance is the spurious radiation of the fed network when it is printed at the same layer as the radiating elements. Discontinuities, bends and long transmission lines in the fed-network can radiate and perturb the antenna radiation patterns, especially in the sidelobe region and cross-polar patterns. Spurious radiation due to the fed-network can be minimized using a multilayer antenna structure which separate the antenna with the fed-network. One antenna element that permits separating the antenna element from the fed network is the aperture coupled patch antenna. This particular antenna type provides the advantage of isolating the antenna and the fed network through a ground plane, permitting a polarization isolation of greater than -25 dB [53]. High levels of cross-polarization present a challenge when square microstrip patches are used for dual-polarized array antennas. Pozar at [46] shows how cross-polarization levels can be highly sensitive to the precision of the feed position. Small errors (<2 %) in the feed position relative to the patch can affect the polarization isolation in 20 dB. To overcome this problem a high precision fabrication process is required.

3.7.1.4 Sidelobes

One of the major advantages of PAR is the flexibility to control array excitations to produce patterns with low sidelobe. High resolution of current attenuators and recent improvements in fabrication capabilities for microstrip array antennas permit the implementation of aperture arrays with amplitude taper distribution to suppress the sidelobe up to -30 dB. For weather radar applications at least -25 dB of the sidelobe suppression is required to minimize contamination in the main beam by the power collected in the sidelobe regions [32]. Reduction of sidelobe can be achieved using a tapered amplitude distribution in the excitation of the array. Various tapered distributions can be used in antenna arrays to suppress the sidelobe, the most common are Chebyshev, Taylor and Cosine on pedestal. These distributions are chosen depending on the required side lobe suppression, aperture efficiency, tolerances, attenuator resolution, number of radiating elements, and expected tolerances in realization. Table 3.7 illustrates the directivity, aperture efficiency, beamwidth, and required tolerances (amplitude and phase) for four different amplitude distributions for a linear array of 18 elements. The directivity and aperture efficiency for a linear array antenna can be estimated using the equations 1.64 and 1.65 in [36], valid for an array with element spacing of at $0.5\lambda_o$. Tapering the amplitude distribution in the antenna excitations provides better sidelobe suppression, however the directivity, aperture efficiency and beamwidth can be compromised. Considering that a PAR provides flexibility to change the aperture distribution, we considered the possibility of using the benefit of uniform distribution in transmission mode in order to maximize the transmit power and narrow beamwidth (maximum directivity and efficiency) and we can use tapered amplitude distribution in reception mode to suppress sidelobes.

Figure 3.12, illustrates the antenna patterns (one-way) using a uniform distribution in transmission mode (Tx), tapered distribution in reception mode (Rx) and the combination of both (two-way pattern) as results of the pattern multiplication

Table 3.7. Required amplitude and phase tolerances for a linear array 18x1 elements.

Excitation distribution	D_i(dB)	ϵ_A	θ_{3dB}(°)	σ_ϕ(°)	σ_a(dB)
Uniform	12.7	1.00	5.3	3.70	-0.60
Chevishev -25dB	12.2	0.92	6.2	3.42	-0.54
Taylor -25dB, n=4	12.1	0.90	6.3	3.38	-0.53
Cosine on pedestal at -25dB	11.8	0.83	6.9	3.26	-0.50

in Tx and Rx (for only H-polarization). In terms average sidelobe suppression, the combination Uniform-Cosine represents the best option compared to other combinations. This combination offers 10 dB better sidelobe suppression compared with other alternatives. However, the first sidelobe level is between 5 and 7 dB higher. Another disadvantage is the broadening beamwidth and the taper efficiency. Table 3.8 summaries the beamwdith, losses, first peak sidelobe, and average sidelobe for the four combinations. Considering all parameters, it seems that the combination of Uniform-Taylor and the Uniform-Chevishev is optimal.

In order to obtain more realistic estimation of the sidelobes, random errors in the excitations (in amplitude and phase) are introduced across the array. Those errors are assumed to be normally distributed (Gaussian) with zero mean and a variance of σ^2 [36] In 3.10, the excitation coefficients A_n with errors will be is A_n $=(a_n + \sigma_a)e^{-i(\sigma_\phi)}$, where σ_a and σ_ϕ represents the amplitude and phase errors in the excitation. Those can be estimated using expression 3.14 where it is expressed as a function of the average sidelobe for an isotropic linear array of N elements. The results shows that even with induced errors in the antenna excitations the combination of Uniform-Taylor and the Uniform-Chevishev is optimal.

$$\overline{SLL}_{dBi} = 10 \log_{10}(\overline{\sigma}_a^2 + \overline{\sigma}_\phi^2) \tag{3.14}$$

50
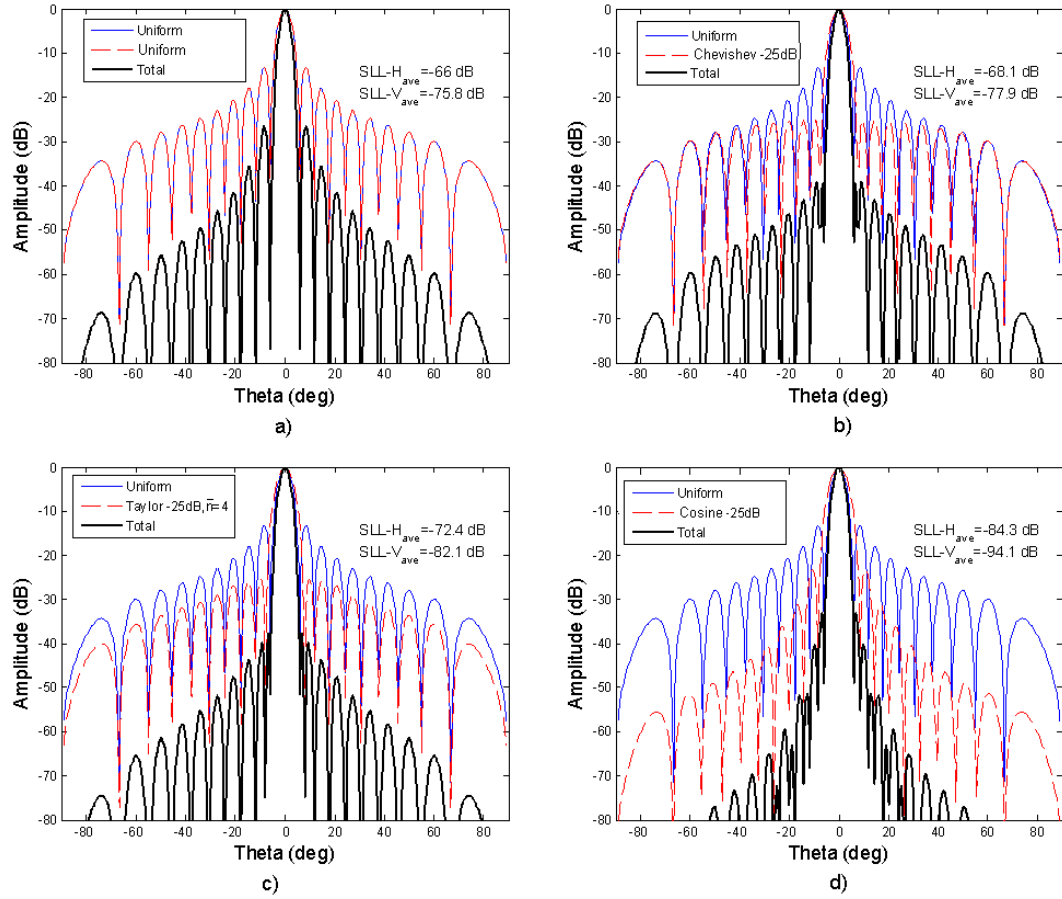
Figure 3.12. One-way and two-way antenna patterns for a linear array of 18x1 elements for: a) Uniform distribution in Tx and Uniform in Rx. b) Uniform in Tx and Chevishev -25dB in Rx c) Uniform for Tx and Taylor -25dB $\overline{n}$=4 for Rx and d) Uniform for Tx and Cosine Pedestal -23dB for Rx. Where the element pattern in H and V are represented by $\cos\theta^{0.8}$ and $\cos\theta^{1.6}$

Figure 3.13, presents the one- and two-way patterns (for only H-polarization) with the effect of random errors. Errors in amplitude (σ_a=0.6 dB) and in phase (σ_ϕ=3.7°) correspond to the maximum tolerance for a uniform linear array of 18 elements. Compared to the ideal case (Figure 3.12), the errors affect the combination Uniform-Cosine most. The Uniform and Taylor alternative presents a better SLL peak and average.
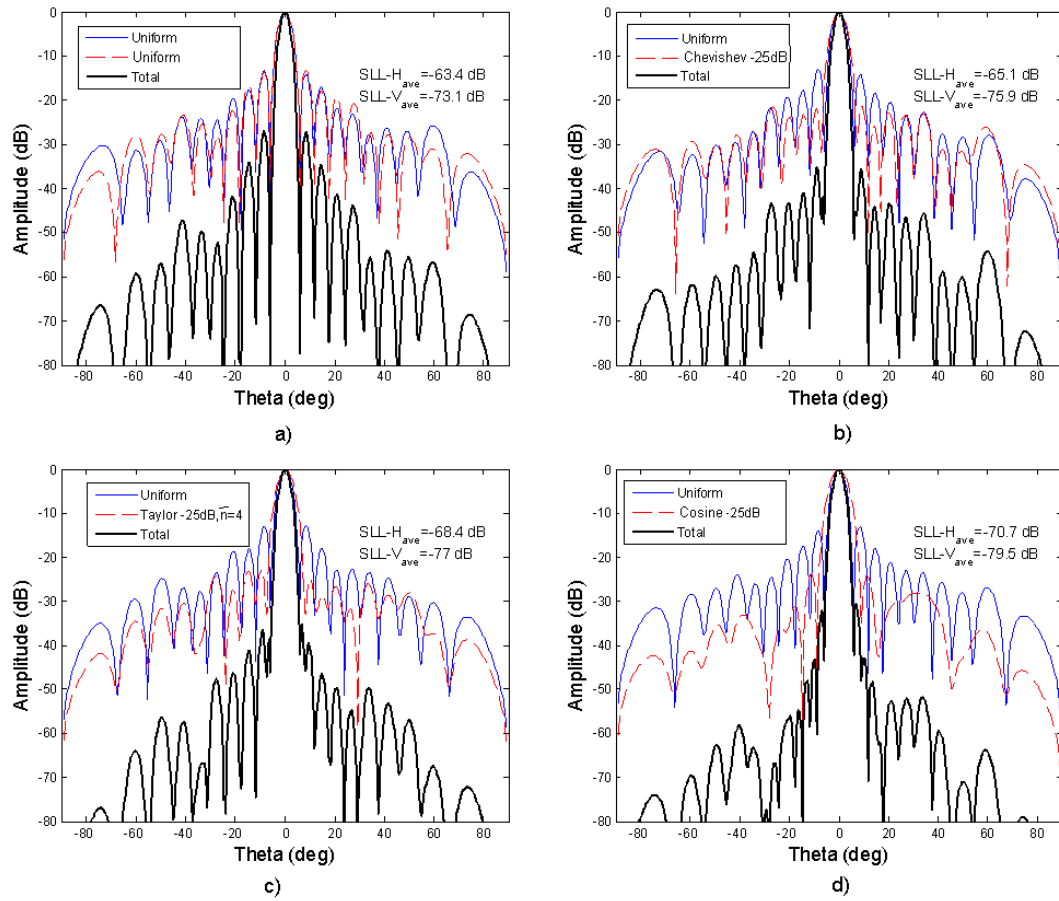
Figure 3.13. One-way and two-way antenna patterns for a linear array of 18x1 elements affected by same random errors in amplituded (σ_a=0.6dB) and phase (σ_ϕ=3.7°) for: a) Uniform distribution in Tx and Uniform in Rx. b) Uniform in Tx and Chevishev -25dB in Rx c) Uniform for Tx and Taylor -25dB $\bar{n}$=4 for Rx and d) Uniform for Tx and Cosine Pedestal -23dB for Rx. Where the element pattern in H and V are represented by $\cos\theta^{0.8}$ and $\cos\theta^{1.6}$

Table 3.8. Two-way antenna patterns sidelobes performance

			σ_a=0dB, σ_ϕ=0°		σ_a=0.6dB, σ_ϕ=3.7°	
Distribution (Tx-Rx)	θ_{3dB} (°)	Loss(dB) (dB)	SLL_p (dB)	SLL_{ave} (dB)	SLL_p (dB)	SLL_{ave} (dB)
Unif.-Uniform	3.9	-0.0	-27/-27	-66/-76	-26/-26	−63/-73
Unif.-Chevishev -25dB	4.0	-0.7	-40/-40	-68/-78	-35/-37	−65/-76
Unif.-Taylor -25dB, n=4	4.0	-0.9	-38/-38	-72/82	-36/-38	−68/-77
Unif.-Cosine -23dB	4.2	-1.6	-33/-33	-84/94	-30/-34	−71/-80

3.8   Conclusion

The most important desirable performance attributes of weather radar are sum-marized in Table 3.1, and used for a trade-off analysis of the key design parameters of the CASA phased array radar. The analysis were carried out first for a single and isolated radar node, considering: a) A single phased array panel (mechanically spined in azimuth and tilted in elevation), b) Three phased array antenna panels (each one performing sector scan angle of 120 ° electronically in azimuth and tilted in elevation) and c) 4 phased array antenna panels (each one performing sector scan angle of 90 ° electronically in azimuth and tilted in elevation). The same radar node configu-rations were embedded in a triangular radar grid network with spacing of 30 km in order to evaluate the radar performance in a radar configured network environment. The analysis was limited to a scanning range 0 ° to 12 ° in elevation plane, since at this scanning range a 100 % radar coverage is obtained at 3.2 km altitude, where the current NEXRAD radar network system only has 70 % coverage [2].

To obtain continuos radar coverage in the azimuth plane, at least 3 phased array panels are required per radar node. Radar nodes with 3 and 4 panels (and not 6 panels) are considered in this analysis since previous results [35] show that imple-menting a radar node with more than 4 panels, is not cost-effective since there is not significant performance improvement.

For short-range radars, as CASA proposed (less than 40 km), the losses in the antenna gain and beamwidth broadening due the electronically scanning performance does not have significant impact in radar sensitivity and spatial resolution. Comparing the radar sensitivity of the 3 radar nodes, small differences, less than 1.2 dB can be obtained from the 3 and 4 panels with respect to the mechanically scan radar. For the spatial resolution, the radar node with 3 panels degrades by 25 % and for the radar node with 4 panels degrades 14 % with respect to radar scanned mechanically.

When the radar nodes are deployed in a radar network, the mean values of the minimum radar sensitivity improves by 7 dB for the lowest altitude (0.05 km) and in 3 dB for highest altitude (3.2 km) for the three radar node configurations. An improvement factor of about 2.5 in the mean spatial resolution is obtained for a radar network observed at the lowest altitude (0.05 km), and an improvement factor of about 1.5 is obtained when radars deployed to observes at highest altitude (3.2 km) for all radar configurations.

To obtain the same radar sensitivity as the IP1 radar system (in a triangular radar network), between 50 W to 120 W peak power and a pulse width between 5 μs to 40 μs is required. Considering a radar network with 4 panels per node and a pulse with of 40 μs, a transmit peak power of 50 W is required to obtain a radar sensitivity (mean values) of 10 dBZ at 50 m altitude and 14 dBZ at 3.2 km altitude.

Two important requirements in the antenna for dual-polarized radars should be satisfied to provide errors less than 0.2 dB in the differential reflectivity Z_{dr} when the ATAR polarization radar mode is considered. The first one requires that the mismatch between antenna patterns (H and V) over the scan volume should not exceed the 5 % integrated power over the main beam. And the second one requires that the cross-polarization isolation between H and V patterns should be less than -20 dB across the scan volume.

Mismatch of the antenna patterns in a phased array antenna is larger than in a dish antenna, since the beam pattern (for H and V) changes with beam position. The Mutual coupling, surface waves and diffracted fields at the edges of the array antenna are the principal causes of mismatch in the phased array antennas.

A simple mathematical model to represent the ripples in the antenna array were presented and used to characterize the effect of ripples in the mismatch antenna patterns. The model was used to represent several scenarios. The worst case scenarios is when surfaces waves (for H and V) reach the antenna borders with a phase difference of 90 °.

Cross-polarization of the antenna array are determined by the polarization of the antenna element, lattice array and also by the fields diffracted in the discontinuities in the antenna (principally at the outer edges).

For ATAR polarization mode, the realization of cross-polarization isolation of -20 dB can easily be obtained for the overall scanning range since the electronically scanning is defined to perform only in the azimuth plane.

Another important parameter evaluated is the sidelobe performance. Sidelobe suppression of -25 dB (in one way antenna patterns) is required for weather radars. This level can be obtained using a 5 or 6 bits digital attenuator and current tolerances in the existing PCB fabrication processes. The analysis here was focused on which combination of aperture distribution can be used for transmission and reception mode in order to obtain a robust performance in the sidelobe without affecting the antenna beamwidth and aperture efficiency. The analysis started by considering the maximum power needed to be in transmission mode. To maximize the transmit power, a uniform aperture distribution is required in transmission. To reduce the effective sidelobe level (two-way antenna patterns) a taper distribution is required in reception. In this analysis the aperture distributions used in reception are: Uniform, Chevishev (-25 dB), Taylor (-25 dB $\overline{n}$=4) and Cosine on pedestal (-23 dB). The results show

that the combination of uniform in transmit and Taylor (-25 dB $\bar{n}$=4) or Chevishev (-25 dB) represents the best combination and provides the best sidelobe performance and aperture efficiency.

CHAPTER 4

PHASE ARRAY ANTENNA PROTOTYPE

4.1 Introduction

This chapter introduces the design and implementation of the antenna array for the CASA phased-array radar. The antenna is a phased array architecture that performs electronic scanning only in the azimuth plane, while a servo motor is used to provide mechanical scanning in the elevation plane. The antenna aperture is a uniform rectangular array composed of 64 elements in the azimuth plane and 32 elements in the elevation plane. In the elevation plane a subarray of 32 elements interconnected in a series-fed network is considered. Each subarray or column is exciting by a T\R module which provides amplitude, phase and polarization diversity. The entire array was fabricated as a multilayer PCB and assembled as a set of modular 18x32 sub-panels.

4.2 System description

The antenna is a rectangular aperture composed of 72x32 elements designed to operate at 9.36 GHz. In order to reduce cost and facilitate the fabrication process, the aperture is subdivided into four sub-panels of 18x32 elements each. Each sub-panel or LRU (Line Replacement Unit) is composed of 18 columns or sub-arrays of 32 dual-linear polarized Aperture Coupled Microstrip Patch Antennas (ACMPAs). These are interconnected by a series-fed network in each polarization. Each subarray or column of 32 elements is fed by a dedicated T/R module, which provides amplitude, phase and polarization diversity. Of the 72 columns, 8 are passive columns (4 at

57

both edges) used to reduce edge diffraction effects and provide more uniform mutual coupling (especially at the edge regions). For the remaining 64 columns, the amplitude and phase of each active element (32x1 linear array) can be individually adjusted to control beam steering and aperture amplitude distribution in the azimuth direction. The spacing between elements is 17 mm $(0.53\lambda_0)$ in both the azimuth and elevation planes. This value restricts the maximum scanning angle to $\pm62.4°$ in azimuth, where the first grating is located. The excitation of each sub-array is controlled in the T/R module with a 6-bit digital attenuator and 6-bit digital phase shifter. Each T/R module has included a FPGA, which creates the control signals from commands that are sent from the array controller. As a part of the control logic, the FPGA's memory is configured as a look-up table, where calibrated settings for the attenuator and phase shifter are stored [59]. Scanning in the elevation plane is performed using a mechanical servo motor, which is capable of scanning up to $90°$. To protect the antenna, a sandwich radome based on low dielectric core material and thin hydrophobic skin layer is considered. Figure 4.1 provides a visual representation of the CASA phased-array antenna and possible deployment in the field.

4.3   Antenna array design

As designed, the array antenna aperture was divided into three parts: a) the radiating antenna element, b) the linear array or column sub-array, and c) the planar array. The linear array was designed using a synthesis method in accordance with the array antenna architecture proposed. Numerical computational software Ansof and HFSS were used [60].

4.3.1   Radiating antenna element

The radiating antenna element in the array consists of a dual-polarized, square aperture coupled microstrip patch antenna. Rogers RT/Duroid 5880 was selected as
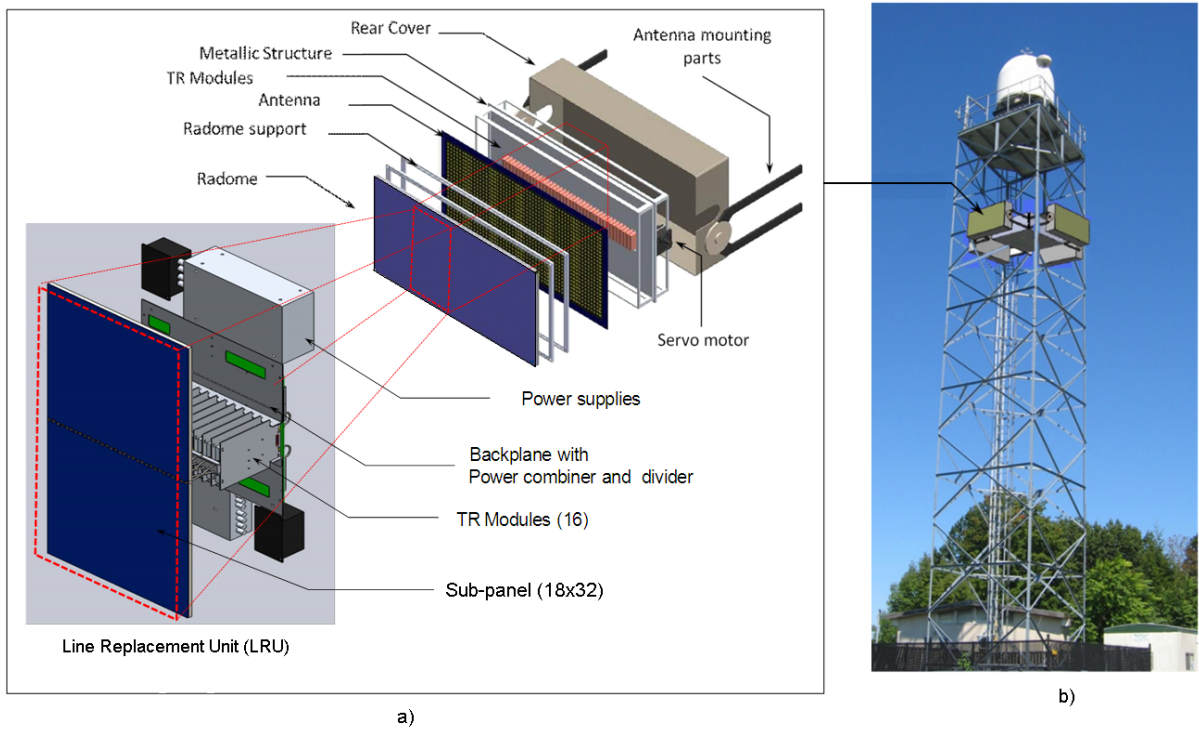
Figure 4.1. CASA phased-array antenna representation and example of radar field deployment.

the RF substrate for the top (patch antenna) and bottom layer (feed). To reduce the backlobe beam, a square reflector patch is placed 250 mil ($\tilde{}\lambda_\circ/4$) apart from the feed. To support the antenna and feed, a foam (Rohacell 31HF) with low dielectric constant (ε_r: 1.04) and tangent loss ($\tan \delta$: 0.0017) is used. The stack up configuration of the array antenna is described in Figure 4.2 d). The microstrip patch antenna is excited with two orthogonal aperture slots to obtain linear dual-polarized fields (H and V). In this design, a dog-bone-shaped coupling aperture was adopted because it requires less area than rectangular slots. This coupling aperture also provides an equivalent and more uniform coupling energy than rectangular slots, and emits low spurious radiation, which helps to improve the cross-polarization isolation of the antenna [54]. Typically, rectangular slot apertures are located at the center of the patch to obtain maximum energy coupling for the feed. In this design, an orthogonal arrangement of the slots, also known as a, "T"slot configuration (see Figure 4.2 b), is considered in order to improve cross-polarization and port isolation [55].

Two antenna elements are considered in the array antenna design. Both geometries are illustrated in the Figure 4.2. In a), a two-port antenna element is used to terminate the linear array. In b), a four-port antenna is used as an inner element in the series-fed array. Figure 4.4 shows the linear array with both antenna elements.

The position of the slots (with respect to the antenna patch) and the spacing between slots defined (g) were optimized to achieve the maximum cross-polarization and front-to-backlobe ratio (FB). The size of the slot (L_s and W_s) and the antenna size (L and W) were also optimized to make the antenna resonate at 9.36 GHz, and also to obtain the impedance required for a series-fed array antenna (discussed in the next section). The transmission line width (w_f) was calculated for 100 Ω and the length of serpentine lines was carefully designed to obtain 360° for each polarization.

Figure 4.3 shows the simulated results of the antenna patterns for the four-port antenna element. In a), the co-polar and cross-polar patterns for the E-plane and
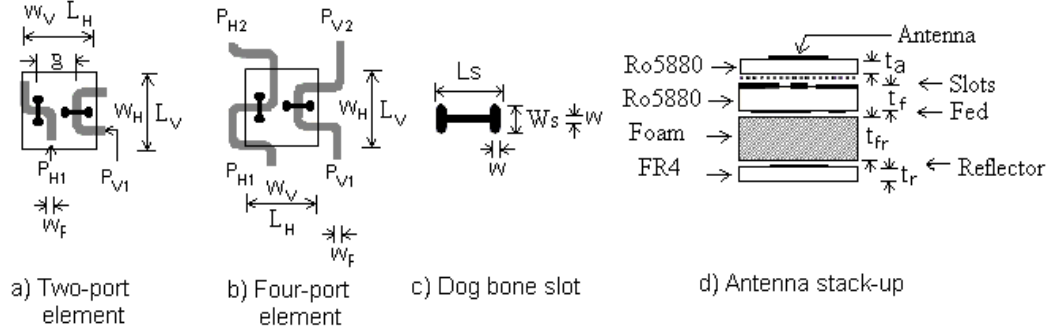
Figure 4.2. Geometry of the a dual-polarized aperture coupled microstrip patch antenna. a) Two-port antenna element b) Four-port antenna element c) Dog-bone shape slot L_s, $W_s = \frac{Ls}{2}$-w and d) Antenna stack-up. d) Antenna stack-up, where $t_a = 20$ mil, $t_f = 31$ mil, $t_{fr} = 250$ mil, $t_r = 125$ mil. The materials Rogers RT/duroid 5880 where $\varepsilon_r = 2.2 \pm 0.02$ and $\tan\delta = 0.009$

H-plane when the antenna is excited in port H are shown. In b), the same is shown when the antenna is excited in port V. The gain for H is about 6.3 dB and for V is about 6.5 dB, and the cross-polarization levels for H and V are -42 and -33 dB respectively. The front-to back lobe ratio (FB) is about -29 dB and -33 dB for H and V respectively. The antenna impedance for H is about $8.26 + 0.2i$ and for V, $5.9 + 0.8i$. The antenna bandwidth for this element is about 240 MHz at -10 dB return loss.

4.3.2 Linear array antenna

To interconnect the antennas 32 elements in the elevation plane, two serpentine lines of 100 Ω are used to serially feed each element in both polarizations. This series-fed configuration offers the advantages of using less substrate area and experiencing less loss than with the a corporate fed design. The drawbacks of a series-fed configuration is design complexity, since it typically involves synthesizing antenna dimensions for a specific feed antenna architecture. The case of using serpentine lines presents a design challenge since their multiple bends introduce parasitic capacitances and inductances that can affect the accuracy of synthesis procedure employed to obtain
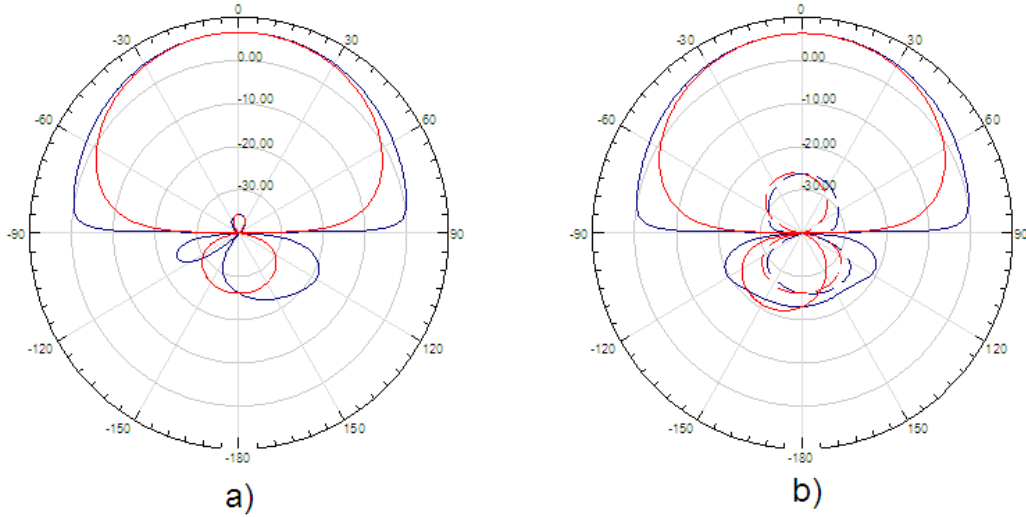
Figure 4.3. Simulated antenna element patterns of four-ports, L_{s-h} = 2.5 mm, L_{s-v} =2.1 mm, L_h =W_v=10.05 mm, L_v=W_v=10.04, g=4.5 mm a) Element polarized in H and b) Element polarized in V

the amplitude and phase required through the array. A symmetric center feed composed of a T-junction power divider, with quarter-wavelength sections to match 100 Ω serpentine microstrip lines, is considered. Center feeding simplifies the design since the left and right halves of the array are mirror images, and it also provides more symmetric sidelobe roll-off. The spacing between elements of 17 mm (equivalent to $0.53\lambda_\circ$) was determined in order to facilitate the accommodation of the serpentine lines, power dividers, and SMP connectors in the feed layer. Figure 4.4 a. illustrates the drawing of the linear array antenna of 32 elements.

4.3.2.0.1 Linear array synthesis. The design procedure for the linear array antenna was developed using an equivalent circuit model of an N-element, series-fed linear array, where each element can be represented as impedance interconnected in series for a serpentine transmission line, each spaced one-half dielectric wavelength apart. This model and its respective parameters are represented in Figure 4.4 d. Each inner section represents a four-port dual-polarized aperture patch antenna (Figure 4.4

b) with the exception of the ends, where a two-port dual-polarized aperture patch antenna is used as the terminal element (Figure 4.4 c).

A dual-polarized ACMPA was designed and then optimized to be resonant at 9.36 GHz, and also to obtain a cross-polarization better than -25 dB and a front-to-back lobe radiation better than -20 dB. Then, a set of 9 four-port ACMPAs were designed to characterize the antenna impedance (real and imaginary part) as a function of the slot length. The range for the slot length was limited by the cross-polarization, port isolation levels and by the space required to arrange the two orthogonal slots and the respective feeds lines. To include the effect of mutual coupling in the antenna impedances, the design considered two adjacent elements on each side in the principal planes. Two elements were considered since no changes were observed in the antenna impedance when more that two elements were added. Table 4.1 and Table 4.2 summarize results simulated in Ansoft Designer of 9 antenna elements, where patch and reflector dimensions were optimized for different slot lengths for H and V polarizations. The range in slot length varies from 2.1 mm to 2.9 mm for H polarization and from 1.7 mm to 2.5 mm for V polarization. The results for H polarization shows that the real part of the antenna impedance varies from 4.9 Ω to 19.3 Ω. The variation in gain is about 0.42 dB where the minimum is 6.21 dB and the maximum is 6.63 dB. The cross-polarization values are between -37 dB to -47 dB. And the FB varies from -25 dB to -31 dB. Similarly for the elements polarized in V, the results in Table 4.2 show the antenna impedance (real part) varies from 3.9 Ω to 14.4 Ω, the gain varies from 5.47 dB to 6.56 dB, the cross-polarization values varies from -32 dB to -36 dB, the FB varies from -23 dB to -30 dB.

Once the two- and four-port antenna elements for H and V are characterized, the iterative synthesis starts defining the slot length of the last element (two-port element) according to the required power radiated, which is defined for the voltage or current coefficients for a given aperture illumination. The next step consists of

Table 4.1. Four-port antenna element characterization for horizontal polarization

L_s(mm)	$Z_a(\Omega)$	G(dB)	X_{pol}(dB)	BL(dB)	L_{opt}(mm)
2.1	4.9+1.85i	6.21	-47	-25	10.13
2.2	5.60+1.60i	6.23	-46	-22	10.12
2.3	6.34+1.20i	6.35	-46	-33	10.10
2.4	7.10+0.75i	6.44	-46	-33	10.08
2.5	8.30+0.10i	6.53	-42	-33	10.05
2.6	11.1+0.06i	6.59	-40	-32	9.96
2.7	16.6+0.0i	6.63	-37	-31	9.88
2.8	17.1+0.02i	6.62	-37	-31	9.87
2.5	19.3+-0.59i	6.63	-39	-31	9.85

Table 4.2. Four-port antenna element characterization for vertical polarization

L_s(mm)	$Z_a(\Omega)$	G(dB)	Xpol (dB)	BL(dB)	L_{opt} (mm)
1.8	4.15+1.80i	5.72	-36	-23	10.12
1.9	4.40+1.50i	5.91	-33	-28	10.10
2.0	4.90+1.10i	6.09	-34	-29	10.08
2.1	5.97+0.80i	6.30	-32	-29	10.04
2.2	7.45+0.40i	6.42	-32	-30	10.01
2.3	11.82+0.00i	6.54	-33	-29	9.88
2.4	12.83.-0.20i	6.55	-33	-30	9.87
2.5	14.4+0.03i	6.56	-34	-29	9.82
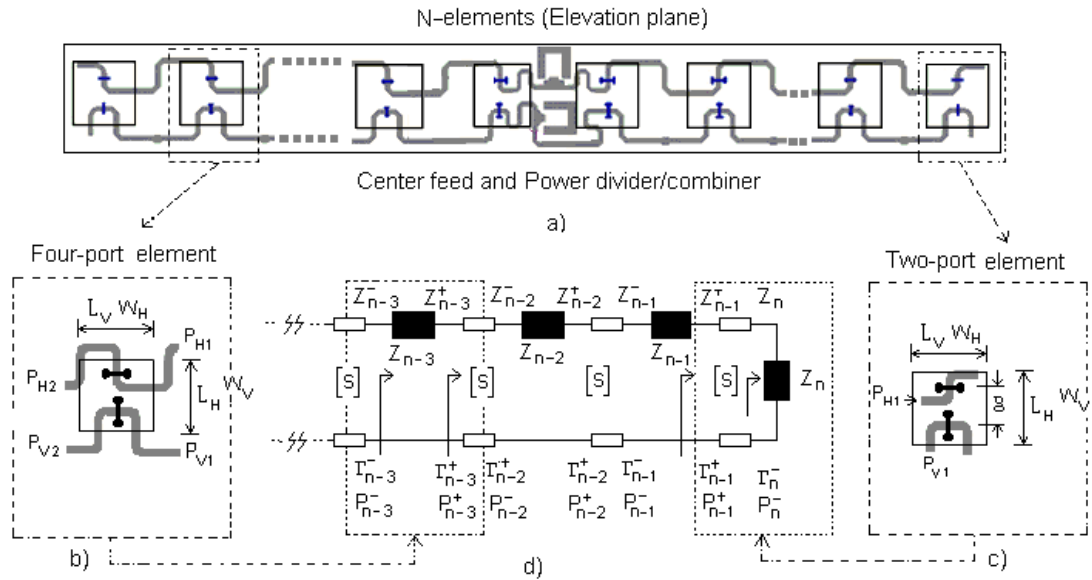
Figure 4.4. Linear array of 32 dual-polarized ACMPA (column of N elements) in the elevation plane. a) Representation of the antenna array layout. b) Geometry of four-port antenna element c) Geometry of two-port antenna element and d) Equivalent circuital model for the half of the series-fed array antenna of elements for one poalrization.

substituting the antenna impedance in equation 4.1 to calculate the incoming input reflection coefficient (Γ_n^-) of n-element of the array. In Figure 4.4 d. The superscripts + and - (in the parameters in Figure 4.4 d) indicates the quantity at the outgoing and incoming sides of the each antenna section along the linear array antenna. With the previous calculation and the S-parameters of the serpentine line (simulated previously), equation 4.2 and 4.3 are used to provide the outgoing impedance (Z_{n-1}^-) of each section of the linear array.

$$\Gamma_n^- = \frac{Z_n^- - Z_o}{Z_n^- + Z_o}\ , \qquad n = N,\ N\text{-}1, ..., 1 \tag{4.1}$$

$$M_n = \frac{S_{12}S_{12}\Gamma_n^-}{1 - S_{22}\Gamma_n^-}, \qquad n = N,\ N\text{-}1, ..., 1 \tag{4.2}$$

$$Z_{n-1}^- = Z_o \frac{S_{11} + M_n + 1}{S_{11} + M_n - 1}, \qquad n = N,\ N\text{-}1, ..., 1 \tag{4.3}$$

$$P_n^- = P_n + P_n^+, \qquad n = N,\ N\text{-}1, ..., 1 \tag{4.4}$$

The incoming power for the n-element (P_n^-) is calculated by equation 4.4, which represents the summation of the radiated power by each element $(P_n \simeq a_n^2)$, where a_n represents the excitation coefficients for each element), and the outgoing power (P_n^+) of each section. It is determined using expression 4.5, where Γ_n^+ can be calculated using equation 4.1, replacing by Z_n^- by Z_n^+.

$$P_{n-1}^+ = P_n^- \frac{\left(1 - \left|\Gamma_{n-1}^+\right|^2\right)\left|1 - S_{22}\Gamma_n^-\right|^2}{\left|S_{21}\right|^2 \left|1 - \Gamma_n^-\right|^2}, \qquad n = N,\ N\text{-}1, ..., 1 \tag{4.5}$$

Once obtained, the values of: Z_{n-1}^+ and P_{n-1}^+ and the antenna impedance Z_{n-1} are calculated for each section using expression 4.6. Then a fit polynomial expression that relates the impedance of the antennas as a function of the slot length can be used to calculate the respective slot length for each antenna section.

$$Z_{n-1} = \frac{Z_{n-1}^{+} P_{n-1}}{P_{n-1}^{+}}, \quad n = N, N-1, ..., 1 \tag{4.6}$$

Figure 4.6 and Figure 4.7 show the results of the synthesis implemented in MatLab for a linear array of 18 elements with center feed. Two amplitude taper distributions corresponding to Taylor-25 dB $\bar{n}$=4 and Chevishev -25 dB are considered. The program requires as input parameters: the s-parameters of the serpentine lines for H and V polarizations; the polynomial functions of the antenna impedance (real and imaginary) of the two- and four-port antenna elements; and the number of elements and coefficients for the taper distribution. The s-parameters of the serpentine lines were obtained from simulations using Ansoft Designer. Figure 4.5 shows the geometry of the serpentine lines for H and V polarizations. The width of the serpentine line (W_F) and the length of the transmission lines (L_F) were optimized to minimize the return losses (S_{11}, S_{22}) and insertion losses (S_{12}, S_{21}), considering a line impedance of 100 Ω with a phase of 360°. Results of the s-parameters are detailed in Table 4.3. The step transition in the center of the serpentine line in V (see Figure 4.5) is added to compensate for the inductive part of the serpentine lines due to its multiple bends. The dimensions were estimated using the model in [56].

Table 4.3. S-paramaters of the serpentine lines for H and V polarizations.

S-parameter	V	H
S_{11}	0.00331+0.00282i	-0.00869-0.05081i
S_{12}	0.97361-0.01376i	0.97507-0.01448i
S_{21}	0.97361-0.01376i	0.97507-0.01448i
S_{22}	0.00347+0.00293i	0.00161+0.06590i

Figure 4.6 shows the output results for a linear array of 18 elements using Taylor's taper distribution of -25dB $\bar{n}$=4. In a), the phase excitation for H and V for each element presents an accumulative phase error which increases for both polarizations.
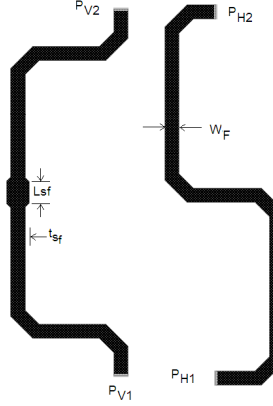
Figure 4.5. Serpentine line to interconnect the inner four-port ACMPA for H (rigth) and V (left) polarizations. L_{sf}=1 mm, t_{sf}=0.2 mm, W_F=0.68 mm

This can be attributed to small phases induced in each section of the serpentine lines and to the imaginary part of the antenna element impedance, which is slightly higher in H than V. Illustration b) shows the calculated amplitude excitation for H and V in each section of the half array. The average errors of 1.5% and 1.3% in H and V are estimated with respect to the ideal coefficients. Illustrations c) and d) show the slot length and patch length synthesized for each element in half of the linear array. Illustrations e) and f) show the linear antenna patterns for each half array (dash lines) and also the superposition of both to obtain the antenna full pattern for 18 elements of the array, for both polarizations. Each half array presents a beam shift of $\pm0.125°$, which is produced by accumulative phased errors in the serpentine lines. This beam shift can be critical when values exceed $\pm0.25°$. The full patterns in e) and f) present a first sidelobe level of 25.4 dB for H and 25.3 dB for V. Figure 4.7 shows the output results for an array of 18 elements using a Chevishev taper distribution for a -25 dB sidelobe level. Similar performance to that in the previous case was obtained for this taper distribution.

It seems that the synthesis method proposed is limited by the losses and reactance characteristics of the serpentine lines. Even with carefully designed serpentine lines,
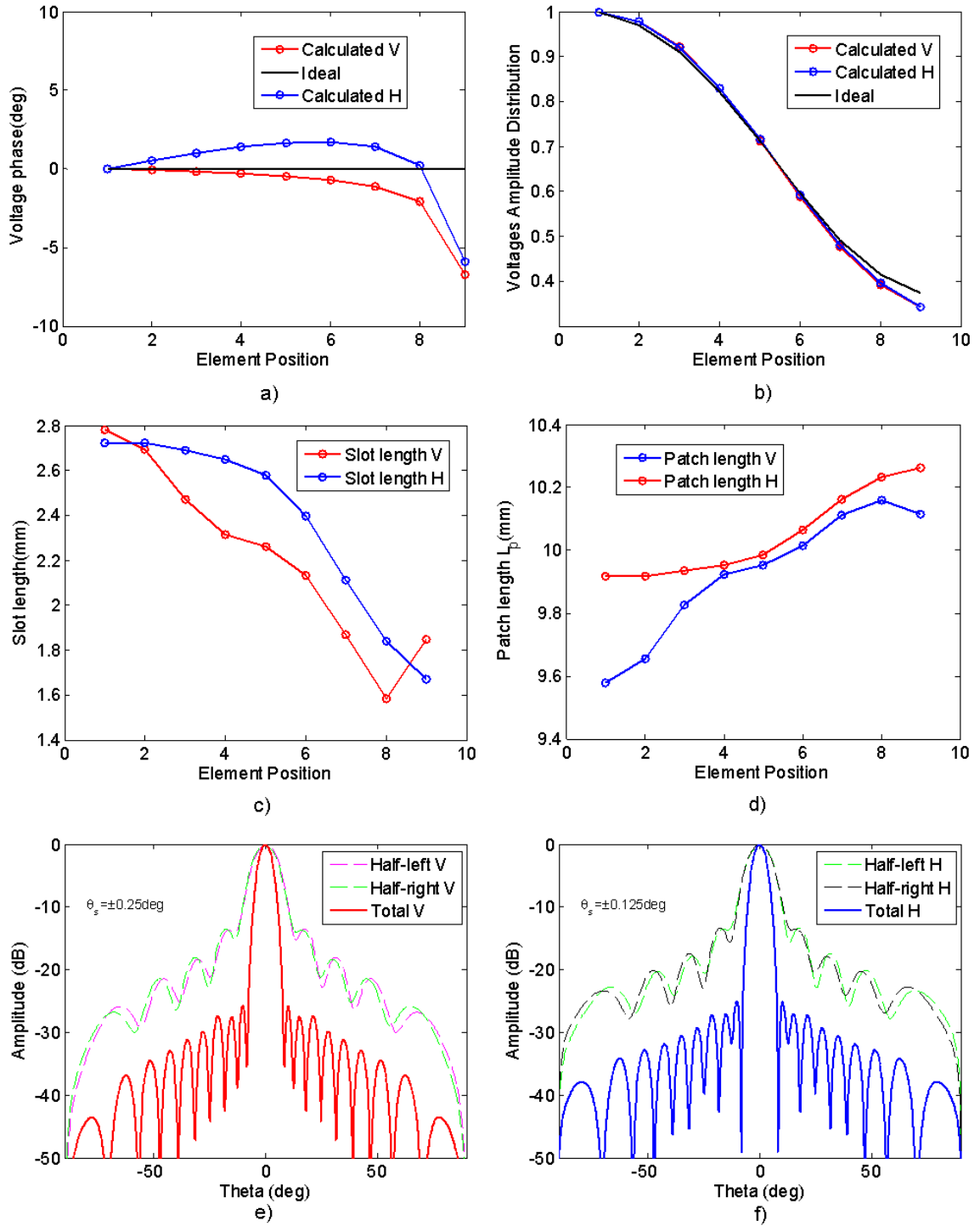
Figure 4.6. Calculated results based on synthesis method proposed for a series-fed linear array of 18 ACMPA elements for a amplitude distribution of Taylor -25dB, $\overline{n} = 4$ a) Excitation phase of half of the array normalized with respect of the center element for H and V b) Voltage excitations of half linear array antenna for H and V c) Length of the slots in H and V for half of the linear array d-e) Calculated patterns for the left and right half array and also the patters of the full array
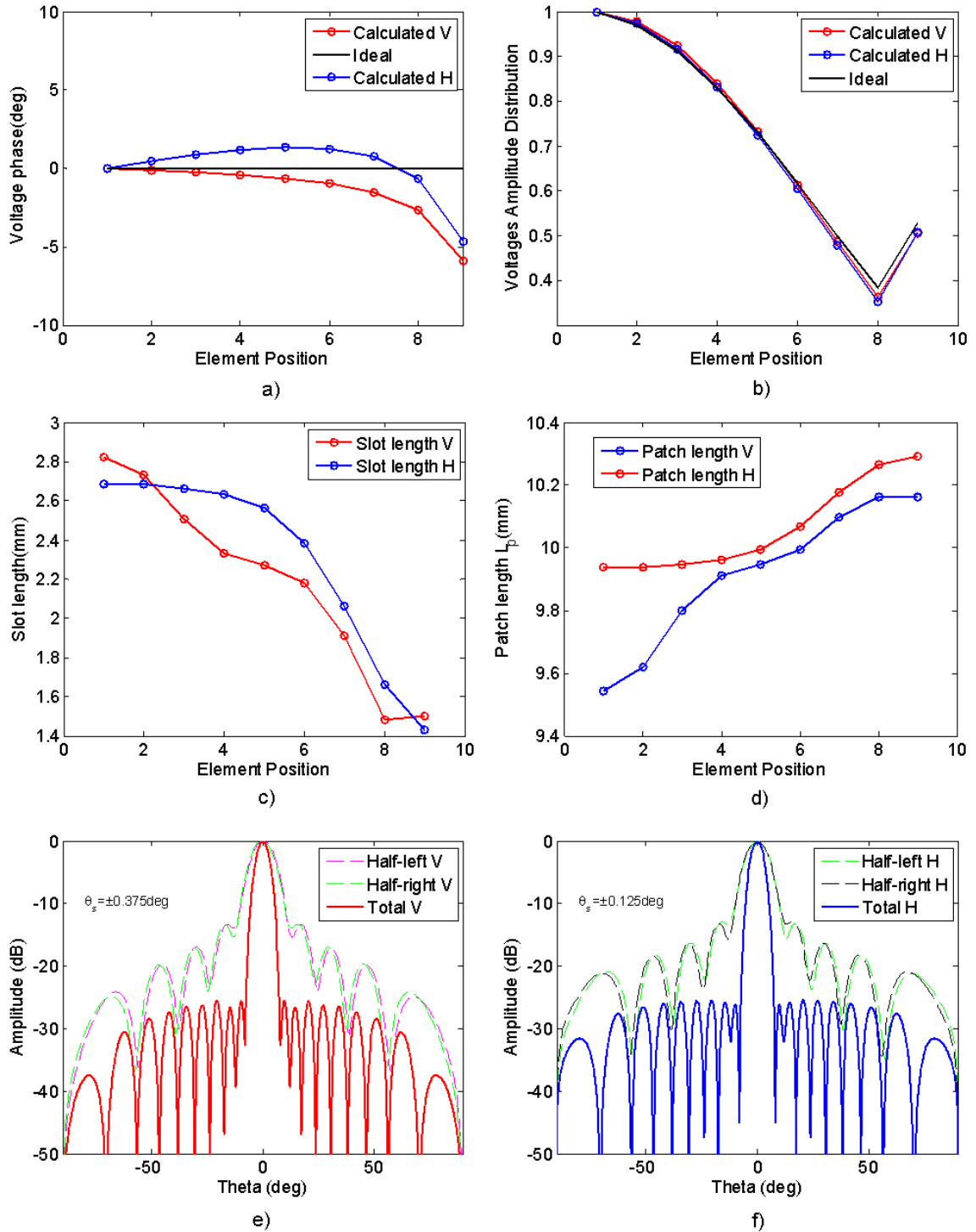
Figure 4.7. Calculated results based on synthesis method proposed for a series-fed linear array of 18 ACMPA elements for a amplitude distribution of Chevishev -25dB a) Excitation phase of half of the array normalized with respect of the center element for H and V b) Voltage excitations of half linear array antenna for H and V c) Length of the slots in H and V for half of the linear array d-e) Calculated patterns for the left and right half array and also the patters of the full array

the method loses accuracy ($>$12%) when the number of elements are higher than 32 elements. A higher number of elements implies larger errors in phase excitation, making the beam shift larger than $\pm 0.25°$ and significantly affecting the first sidelobe. In addition, the losses produced in the serpentine lines significantly affect the gain of the antenna array. A tentative solution of increasing the size of the slot length (to increase the antenna impedance and compensate for radiation loss) is not possible because the space constraints associated with bigger slot lengths degrade cross-polarization and backlobe beam radiation.

Figure 4.8 shows the output results applying the synthesis method for a linear array of 32 elements using a Taylor -25dB $\overline{n}$=4. The phase excitation for H and V for each element produces a larger accumulative phase error (higher H and than V). This makes the half beam patterns reach the maximum beam shift (± 0.25 °) possible to still guarantee accurate results in the first sidelobe levels. One possibility for minimizing this beam shift consists of improving the s-parameters of the serpentine lines. In b), the amplitude excitation for H and V is compared to ideal voltage coefficients. The calculated excitation does not accurately fit within given ideal values. The average error for H and V is 9.23 % and 5.8 %, respectively. Besides errors in amplitude coefficients and phase, the patterns illustrated in d) and e) provide acceptable performance in terms of sidelobe: 24.96 dB is obtained for V and 25.79 dB for H. Similarly, for the Chevishev -25 dB amplitude distribution, the results in Figure 4.8 show larger errors for H in phase and amplitude compared to V. In amplitude, the average error is about 12 % for H and 4.2 % for V. The errors in phase make a beam shift in H of about ± 0.25 ° and about ± 0.125 ° for V. The patterns in e) shows that the sidelobe level is off by 1 dB due to errors produced.
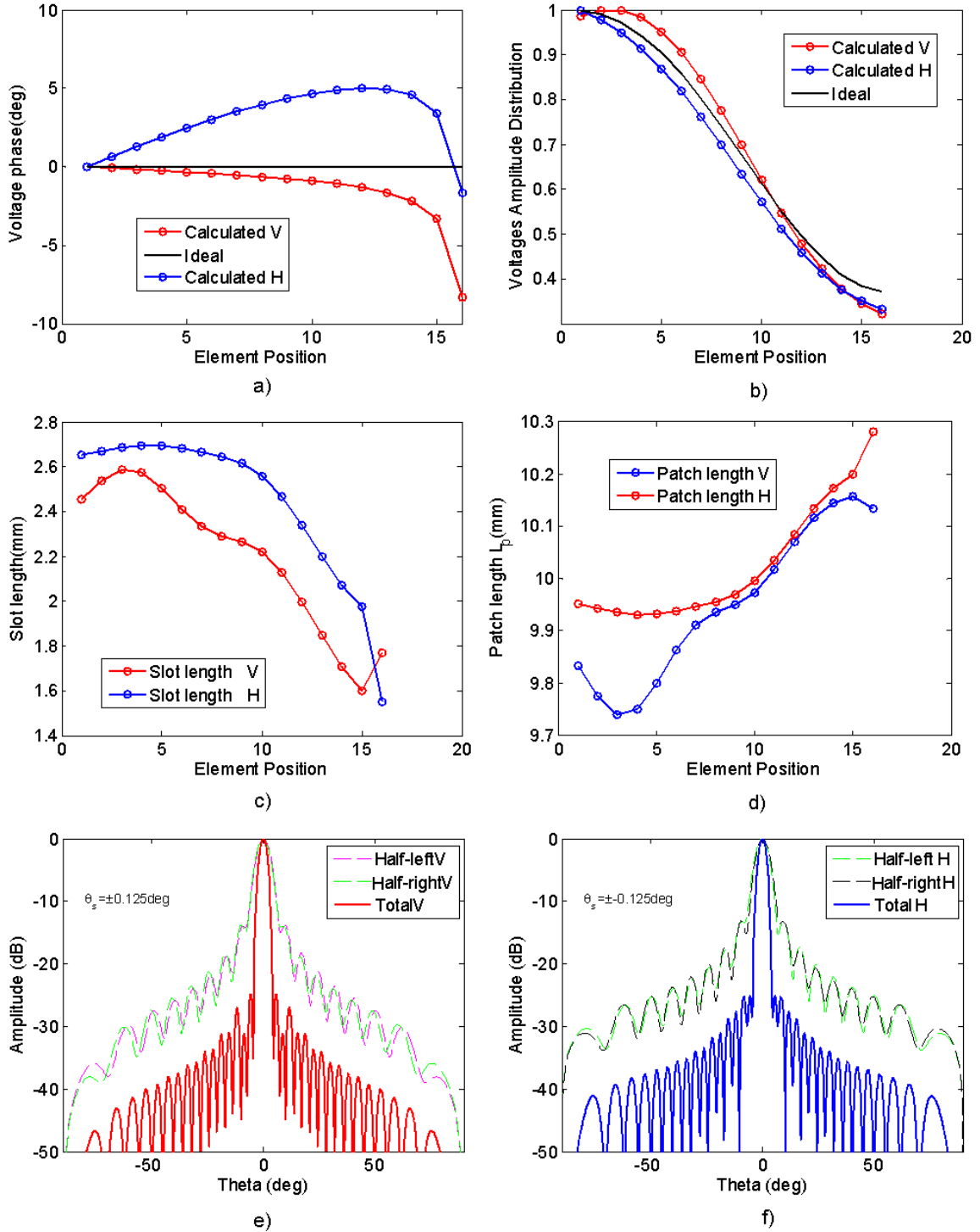
Figure 4.8. Calculated results based on synthesis method proposed for half of the series-fed linear array of 32 ACMPA for a amplitude distribution of Taylor -25dB, $\overline{n} = 4$ a) Estimated phase normalized to the center element for H and V b) Ideal and estimated voltage excitations of half linear array antenna for H and V c-d) Calculated length of the slots and patch in H and V for half of the linear array e-f) Calculated patterns for the left and right half array and also the patters of the full array
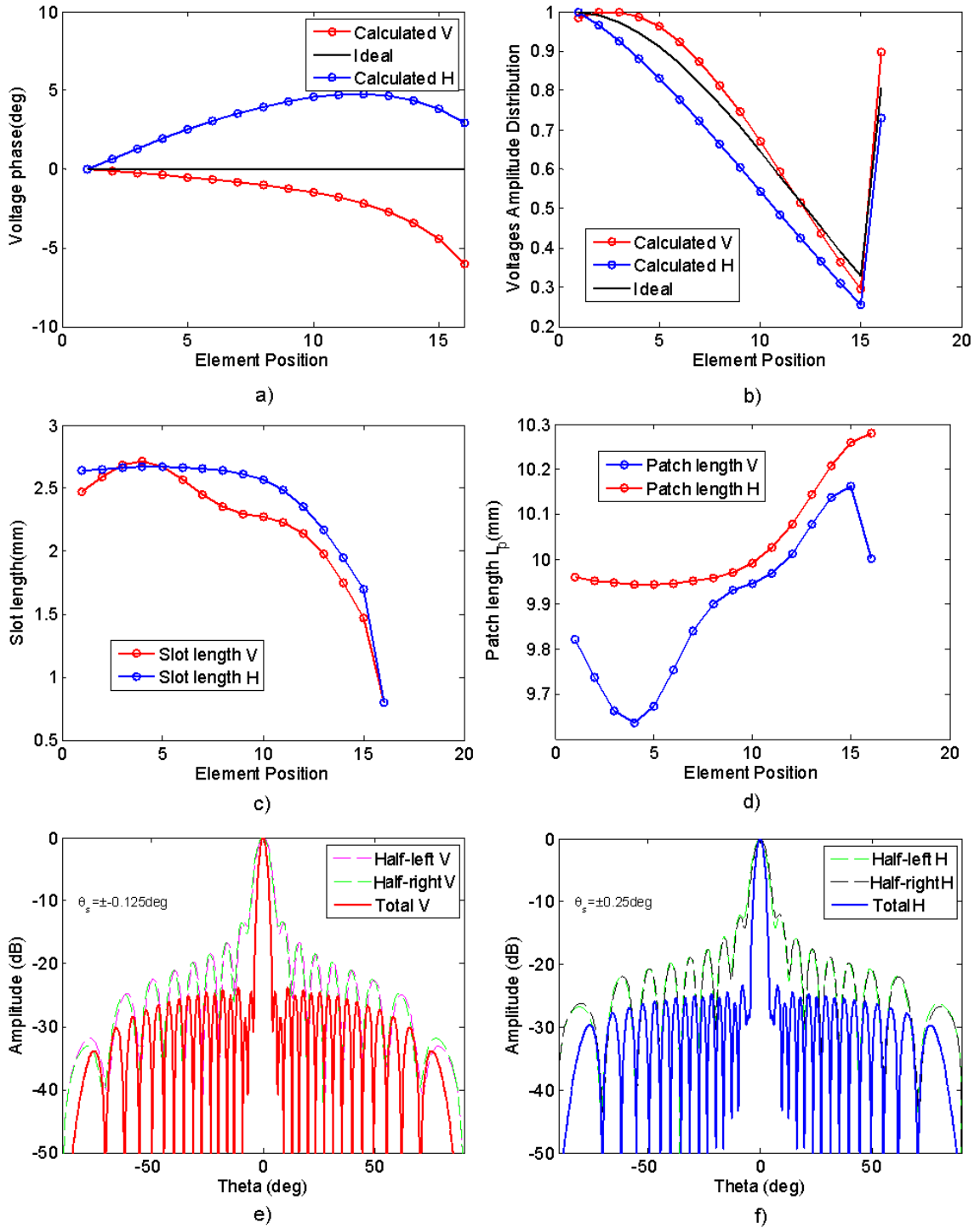
Figure 4.9. Calculated results based on synthesis method proposed for half of the series-fed linear array of 32 ACMPA for a amplitude distribution of Chevishev -25dB a) Estimated phase normalized to the center element for H and V b) Ideal and estimated voltage excitations of half linear array antenna for H and V c-d) Calculated length of the slots and patch in H and V for half of the linear array e-f) Calculated patterns for the left and right half array and also the patters of the full array

4.3.3 Planar array antenna

The planar array antenna composed of 72x32 elements is designed in 4 sub-panels called Line Replacement Unit (LRU) in an effort to facilitate the assembly, and also to reduce the fabrication cost and maintenance. Each sub-panel consist of 18 columns of 32 elements each.
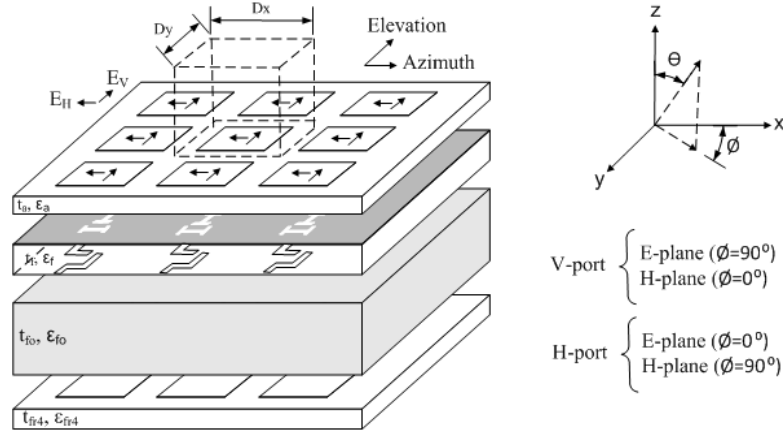
Figure 4.10. Array antenna stack-up using dual-polarized aperture coupled patch antenna and field references, with unit cell dimension of $D_x=D_y=17$ mm $(0.53\lambda_\circ)$.

In the complete array 8 columns (4 on each side only in the azimuth direction) are used as dummy elements in order to minimize the diffraction of the fields across the edges of the antenna. The lattice spacing in the azimuth-plane of 17 mm $(0.53\lambda_\circ)$, equal to that of the elevation-plane, was determined to accommodate the limited space available for the serpentine fed lines and the SMP connectors for each polarization. As a result of an effort toward reducing spacing in the azimuth plane to avoid grating lobes in the visible region, the coupling between feed lines compromised the cross-polarization performance of the antenna. A trade-off between cross-polarization and maximum scanning range was made in order to guarantee good performance of

cross-polarization at maximum scanning range. The next sub-sections show the performance of the cross-polarization at a $\pm 50°$ scanning range even with the presence of the grating lobe at $62.3°$ in the azimuth plane. To evaluate the scanning performance of the array (in the azimuth plane), the effect of the grating lobes and possible excited surface waves on antenna impedance was evaluated for the required scanning range. The scanning performance in the azimuth plane was evaluated using the propagation constant of the antenna unit cell (specified in Figure 4.10), based on simulations using the infinite array approach in HFSS. Then measured values of the active antenna element embedded in an array of 18x32 (LRU) were used to corroborate the predicted mismatch of the antenna as function of the scan angle in the azimuth plane.

4.3.3.1 Propagation constant of surface waves and grating lobes

The mismatch between antenna impedance and scan angle in microstrip patch antenna arrays is attributed to grating lobes, surface waves or both. When the lattice array exceeds half of the free space wavelength ($d > 0.5\lambda_\circ$), the grating lobe appears in the visible region, affecting the antenna matching at some specific beam position. The grating beam can be avoided if the spacing between elements is less than $d < 0.5\lambda_\circ$. Surface waves are excited when high dielectric constants or thick substrates are considered in the design. Stacked substrates with mixed dielectric constants are typically used for applications where large impedance and gain bandwidth are required [57]. Such designs require careful consideration to suppress possible surface waves, fabrication complexity, and costs for the antenna. One simple way to avoid excitations of surface waves in printed scanned array antennas is satisfying the condition $t < \lambda_\circ/4\sqrt{\varepsilon_r - 1}$ suggested by Pozar and Schaubert in [48]. For the phased-tilt array antenna architecture, this criterion cannot be satisfied, therefore an evaluation of the mismatch impedance versus scan angle is required in order to avoid scan blindness or surface waves that can compromise the scanning performance of the antenna. Scan

blindness is produced by the strong coupling between the propagation constant $(k_\circ)$ and the propagation constant of the surface waves (β_{sw}). When this coupling is present, resonances in the substrate can generate undesirable antenna mismatch or blind spots [48],[49]. Due to the complexity of the series-feed in this array architecture, a simplified unit cell of a lattice array of $0.53\lambda_\circ$ with 4-port ACPA elements is used. It includes slot and patch loading effects in the calculation of the propagation constant using the infinite array approach in HFSS (see Figure 4.10). Then the surface wave coupling was examined graphically from the grating lobe and surface wave circles associated with an infinite array using the equations 4.7 and 4.8.

$$(\beta)^2 = (\beta_{sw})^2 = (k_x)^2 + (k_y)^2 \tag{4.7}$$

$$(\beta)^2 = (\beta_{sw})^2 = \left(\frac{2\pi m}{D_x} + k_\circ u\right)^2 + \left(\frac{2\pi n}{D_y} + k_\circ v\right)^2 \tag{4.8}$$

where the m and n are integer indices, $D_x = D_y = 0.53\lambda_\circ$, $k_\circ = 2\pi/\lambda_\circ$, $u = \sin\theta\cos\phi$, $v = \sin\theta\sin\phi$. Term β_{sw} represents the phase constant of the surface waves induced in the antenna substrate.

Figure 4.11 shows the curves of the propagation constant (γ) only for the Floquet modes (0,0) (0,-1) of TE and TM polarizations. When the propagation constant is imaginary, the associated Floquet modes become a plane of waves that propagate along the substrate [57]. For real parts the fields are associated with evanescence modes that are attenuated along the structure. The Floquet modes for $m = 0$ and $n = 0$ are the dominant modes, and represent the waves outside of the array that propagate according to the scan angle. The grating lobes position in the azimuth plane can be obtained using the expression $\theta_b = \sin^{-1}(\lambda_\circ/d - 1)$, which is obtained from equation 4.8 when $\beta = k_\circ$ and $m = 0$ and $n = \pm 1$ (E-plane, H polarization) or when $m = \pm 1$ and $n = 0$ (H-plane, V polarization). Based on this expression, the

grating lobes associated with a lattice array of $0.53\lambda_\circ$ appears at $62.3\,°$. The curve in red represents the propagating surface waves by the modes TE_{-10} and TM_{-10}, which are excited after the grating lobes appear. It seems that the energy of the grating lobes excites the surface waves produced by the antenna structure. Note that the condition given by the equation 4.7 to produce scan blindness (because of surface waves) is satisfied at about $70\,°$.
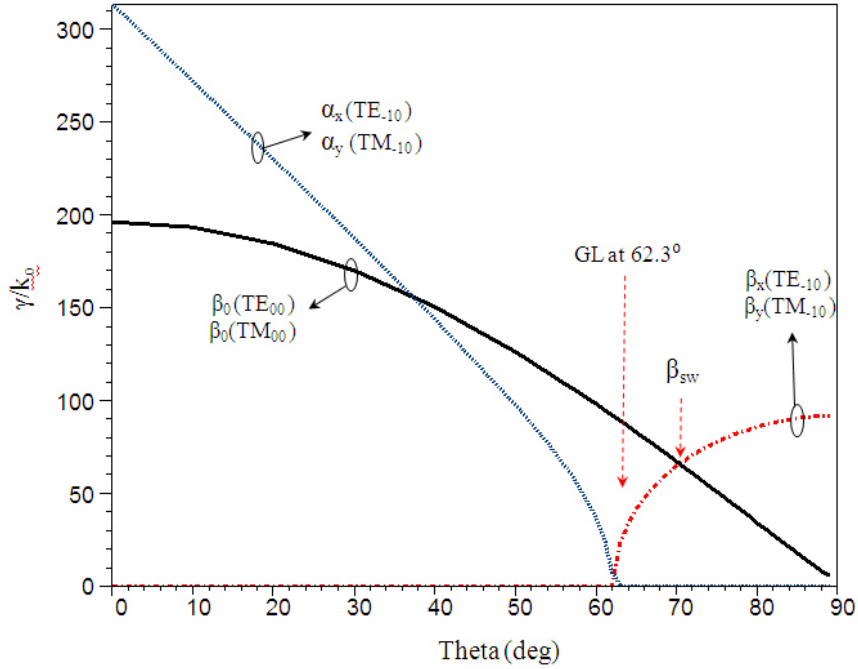
Figure 4.11. Propagation constant (γ) as function of scan angle in azimuth plane for TE and TM modes of a periodic structure of unit cell array antenna described in Figure 4.10

Figure 4.12 shows the maximum scan range versus inter-element spacing or unit cell dimensions in the azimuth plane. Both curves were obtained solving the equation 4.8 for θ based on the propagation constants obtained as described in the previous section. The solid curve is calculated for the grating lobes and the dash curve for the surface waves. Note that, for this antenna architecture and for any lattice dimension selected, the surface waves curve is always behind the grating lobe curve. For a lattice
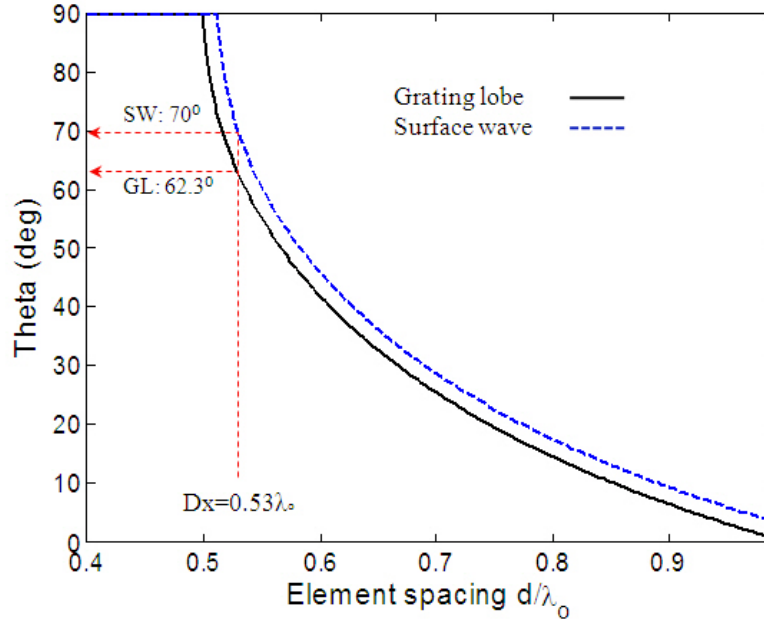
Figure 4.12. Maximum scan range versus lattice dimensions of the phase-til array antenna.

array that satisfies the condition $d < 0.5\lambda_\circ$, surface waves will not be strong enough to produce undesirable resonances affecting antenna mismatch and array scanning performance in the azimuth plane.

4.3.4 Radome

A radome is an integral part that plays an important role in the radar performance system. Its primary responsibility is to protect the array antenna from the ravages of the environment, such wind, snow, ice, rain and temperature changes. In general, any radome should provide electromagnetic transparence and structural strength to protect the antenna. Electromagnetic transparence consists of low reflections, low transmission losses, and minimum distortions in co-polar and cross-polarization antenna patterns. Structural strength is related to wind loading, stability and integrity to mitigate environmental conditions such as temperature, humidity and pressure.

4.3.4.1   Radome requirements for weather radars

For a dual-polarized phased-array weather radar, the radome requirements should satisfy the following criteria:

- *RF performance.* Accurate estimation of rain rate based on polarimetric radar requires a high degree of matching between dual-polarized far-field patterns (principally in the main beam) and near sidelobes. Dual-polarized radar parameters are sensitive to pattern distortion and polarization isolation. Another important requirement for weather radar is minimizing radome insertion losses. A radome with moderate insertion losses ($<$ 2 dB) can be tolerated for radar applications where the transmit power level is not a constraint. However, for short-range weather radars with low transmit power ($\tilde{}$100 W), minimizing radome insertion losses is an important design consideration. Antennas and radomes at X-band are required to have insertion losses better that 1 dB (for the full scanning range).

In presence of rain, water accumulated over the radome can significantly attenuate the radar signal to the point of completely extinguishing the radar signal [15],[58]. In order to minimize water accumulation, a thin film hydrophobic coating must be included in the skin layer so that larger water beads form. Larger beads are more easily blown away by an airstream or gravity.

– *Protection and mechanical integrity.* The radome requires all-weather operation, protecting the radar from wind, rain, snow, hail, sand, animals, UV damage, and wide temperature fluctuation. The radome must be designed to withstand pressures resulting from wind speeds of up to 140 mph. Wind loading associated with extreme weather conditions, such as that from hurricanes and tornados, should be considered in the design process. Radome material should also provide good thermal insulation to keep the internal temperature of electronic parts relatively constant amidst external temperatures ranging from -20 ° C to 50 ° C. It should also exhibit low thermal conductivity to better insulate the antenna from the external environment.

4.3.4.2 Radome design

Three radome configurations were considered as potential alternatives for the CASA phased array radar system. The alternatives were considered in terms of requirements for high RF performance, mechanically integrity and low cost:

a) Foam sandwich wall structure radome.

b) Honeycomb sandwich wall structure radome.

c) Frequency Selective Surface radome (FSS)

The two first radome alternatives are based on a wall structure sandwich radome design, which combines a thin, high-density dielectric material with a thick, low-density/low-dielectric core material, such as foam or honeycomb. The third sandwich radome design consists of two foam dielectric layers with a single FSS layer in between. The design procedure for the sandwich radome was adapted from [63],[64], and the FSS radome design was based on the Jerusalem shape described in [65].

a) *Foam sandwich wall structure radome* - This radome contains a 1/2" thick Rohacell 31HF high frequency performance foam, designed to operate up to 26 GHz. At 10 GHz, the dielectric constant is about ε_r=1.046 and the tangent loss is δ=0.0017. Its 0.0031 gr/cm^3 density provides excellent strength that facilites antenna lamination. The protective skin layer consists of a thin Gore RA7906 fabric, made of expanded polytetrafluoroethylene (e-PTFE). The fabric is resistent to UV and presents hydrophobic properties that help keep the radome dry by making water run-off in rivulets instead of sheeting. It also is resistant to ice adhesion [66]. At 10 GHz, the dielectric constant is about ε_r=1.55 and the tangent loss is about δ=0.0017. As an alternative to Gore RA7906, other materials such as Esscolam 8 and Tedlar can be used, however, Goretex presents much better electrical and mechanical characteristics. Figure 4.13 a) shows the stack of this radome type with the antenna array.

b) *Honeycomb sandwich wall structure radome* - This radome configuration is similar to the previous one, with the exception that the foam was replaced with a

1/2' thick Honeycomb RHR10-1/8-3. Honeycomb RHR10 with similar density (0.0048 gr/cm^3) is based on Aramid reinforced fiber that provides more strength and less water absorption than Rohacell 31HF foam. At 9.37 GHz, the dielectric constant is between ε_r=1.07 and ε_r=1.09, and the cost is relatively similar to the cost of the Rohacell 31HF foam. Drawbacks include fabrication costs and delimitation that can occur since honeycomb has fewer surfaces for contact lamination. Figure 4.13 b) shows the stack for this radome type with the antenna array.

c) *Frequency Selective Surface radome* - The radome consists of a double core dielectric layer and a thin layer of Nelco SI (5 mil) in between to print the FSS shapes. Commonly the dielectric layers are composed of a high-density dielectric material such as Rogers 5880LZ which provides a dielectric constant of ε_r=1.96 and tangent loss of δ=0.0027. However a high density foam dielectric core such as Rohacell 51HF or Eccostock SH-4 can provide lower losses and higher bandwidth response. In this design, Rohacell 31HF was selected, and FSS shapes were printed on Nelco SI (5mil). Figure 4.13 c) shows the stack-up of this radome type with the antenna array. A summary of the materials used for the three radomes proposed are detailed in Table C.1.

4.3.4.3 Radome design procedure

A mathematical model that describes the behavior of electric fields through a flat radome at any angle of incidence and polarization mode was formulated based on the equivalent transmission line method. We consider a multilayer medium with a boundary at $x = t_1, t_2, t_3$ as shown in Figure 4.14 a). Each sandwich radome layer is composed of a homogeneous material with dielectric and magnetic constants (ϵ_n, μ_n). Reflected energy was modeled as a series of reflections as represented in Figure 4.14 b) with a portion of the incident wave energy transmitted into the medium 2 $(x = -t_1)$, at which point some of the energy reflects back from the medium 3 $(x = -t_2)$,
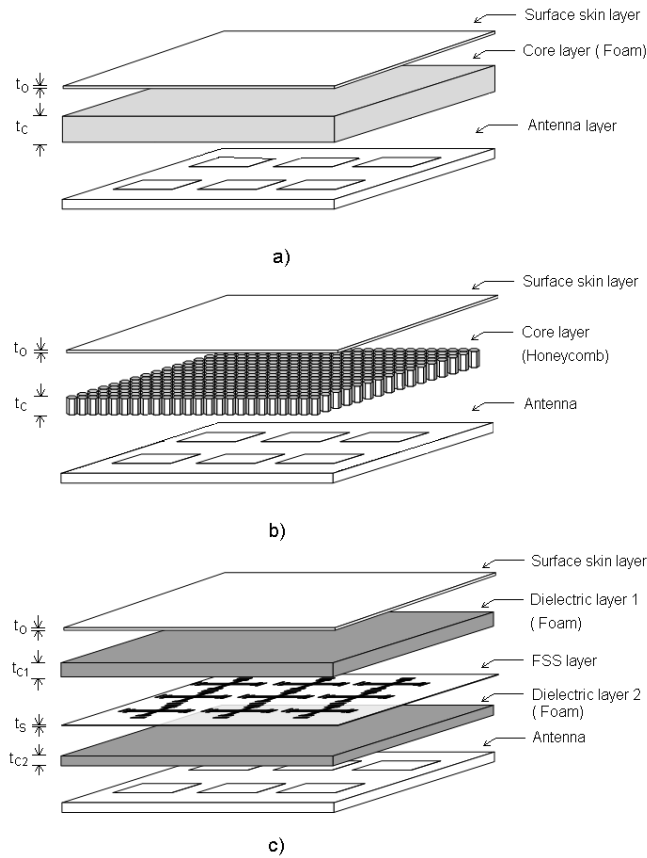
Figure 4.13. Stack-up configuration for radome proposed a) Foam sandwich wall structure radome using Goretex as a skin layer and Rohacell 31HF foam as a dielectric core (t_o=12 mil, t_c=250mil) b) Honeycomb sandwich wall structure radome. using Goretex as a skin material and Rohacell 31HF as a dielectric core (t_o=12 mil, t_c=250mil) c) Frequency selective surface radome using Goretex as a skin layer and Rohacell 31HF as a dielectric core (t_o= 12 mil and t_{c1}=t_{c2}=125 mil).
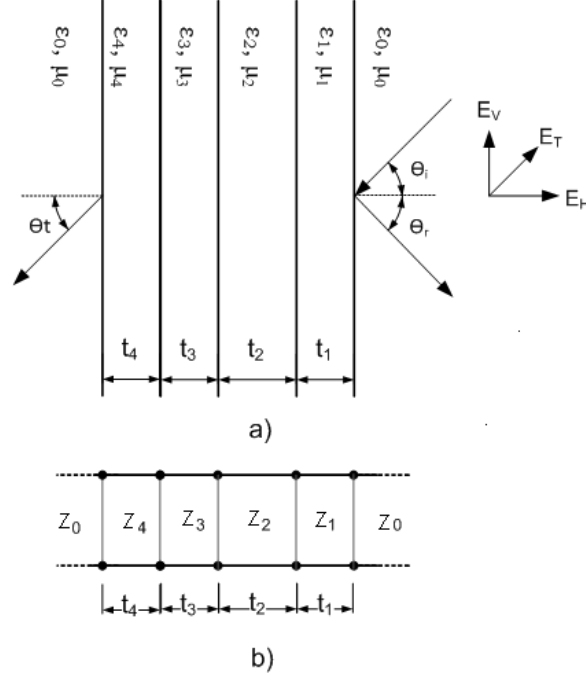
Figure 4.14. Radome model representation a) Multilayer radome and b) Circuital transmission line model

and so on. Assuming an incident plane wave in medium 1, the formulation for the transmission and reflection coefficients for a parallel (horizontal) and orthogonal (vertical) polarization can be represented in equations 4.9 to 4.14

$$\theta_{t(n+1)} = \cos^{-1}\left(\sqrt{1 - \frac{\varepsilon_{r(n)}}{\varepsilon_{r(n+1)}} \sin\left(\theta_{in}\right)^2}\right) \tag{4.9}$$

$$\eta_{tn} = \eta_{(n+1)}\left[\frac{\eta_n + j\eta_{(n+1)}\tan(\beta_{(n+1)}t_n)}{\eta_{(n+1)} + j\eta_n\tan(\beta_{(n+1)}t_n)}\right] \tag{4.10}$$

$$\Gamma_V(t_n) = \frac{\eta_{(n+1)}\cos(\theta_{in}) - \eta_{tn}\cos(\theta_{t(n+1)})}{\eta_{(n+1)}\cos(\theta_{in}) + \eta_{tn}\cos(\theta_{t(n+1)})} \tag{4.11}$$

$$\Gamma_H(t_n) = \frac{\eta_{(n+1)}\cos(\theta_{(tn+1)}) - \eta_{tn}\cos(\theta_{in})}{\eta_{(n+1)}\cos(\theta_{i(n+1)}) + \eta_{tn}\cos(\theta_{in})} \tag{4.12}$$

83

$$T_V(t_n) = \frac{2\eta_{(n+1)}\cos(\theta_{in})}{\eta_{(n+1)}\cos(\theta_{in}) + \eta_{tn}\cos(\theta_{t(n+1)})} \tag{4.13}$$

$$T_H(t_n) = \frac{2\eta_{(n+1)}\cos(\theta_{in})}{\eta_{(n+1)}\cos(\theta_{t(n+1)}) + \eta_{tn}\cos(\theta_{in})} \tag{4.14}$$

The depolarization of cross-polarization introduced by the radome can degrade the performance of the radar system and can be critical for a polarimetric radar system that requires high isolation between polarization channels. To evaluate cross polarization induced by a radome, we use the expression 4.15 defined in [68] and valid for flat radome designs.

$$D_p = \sqrt{\frac{1 - 2K\cos(\phi_H - \phi_V) + K^2}{\cot^2\theta_i + 2K\cos(\phi_H - \phi_V) + K^2\tan^2\theta_i}} \tag{4.15}$$

where K represents the ratio of the transmission coefficients $K = T_H/T_V$, and ϕ_H, ϕ_V represent the respective phases.

Figure 4.15 shows the calculated results using the previous formulation for the first two radomes proposed (wall sandwich radome using Goretex and Rohacell, and A-sandwich radome using Goretex and Honeycomb). For both radomes, the transmission coefficient is lower than -0.4 dB and the reflection coefficient is lower than -25 dB for an incident angle that varies from 0° to 60° in the azimuth plane. The induced cross polarization by these two radomes is very small. A maximum distortion of -34 dB can occur in the incident angle range from 0° to 60°. Small differences between both radomes is due the fact that the dielectric constant in the Honeycomb is slightly higher than that for the Rohacell.

The design procedure for the FSS radome were based on numerical simulations in Ansoft Designer. A unit cell of the FSS periodic structure was computed using an infinite array approach for an incident plane wave (in the azimuth plane). The shape
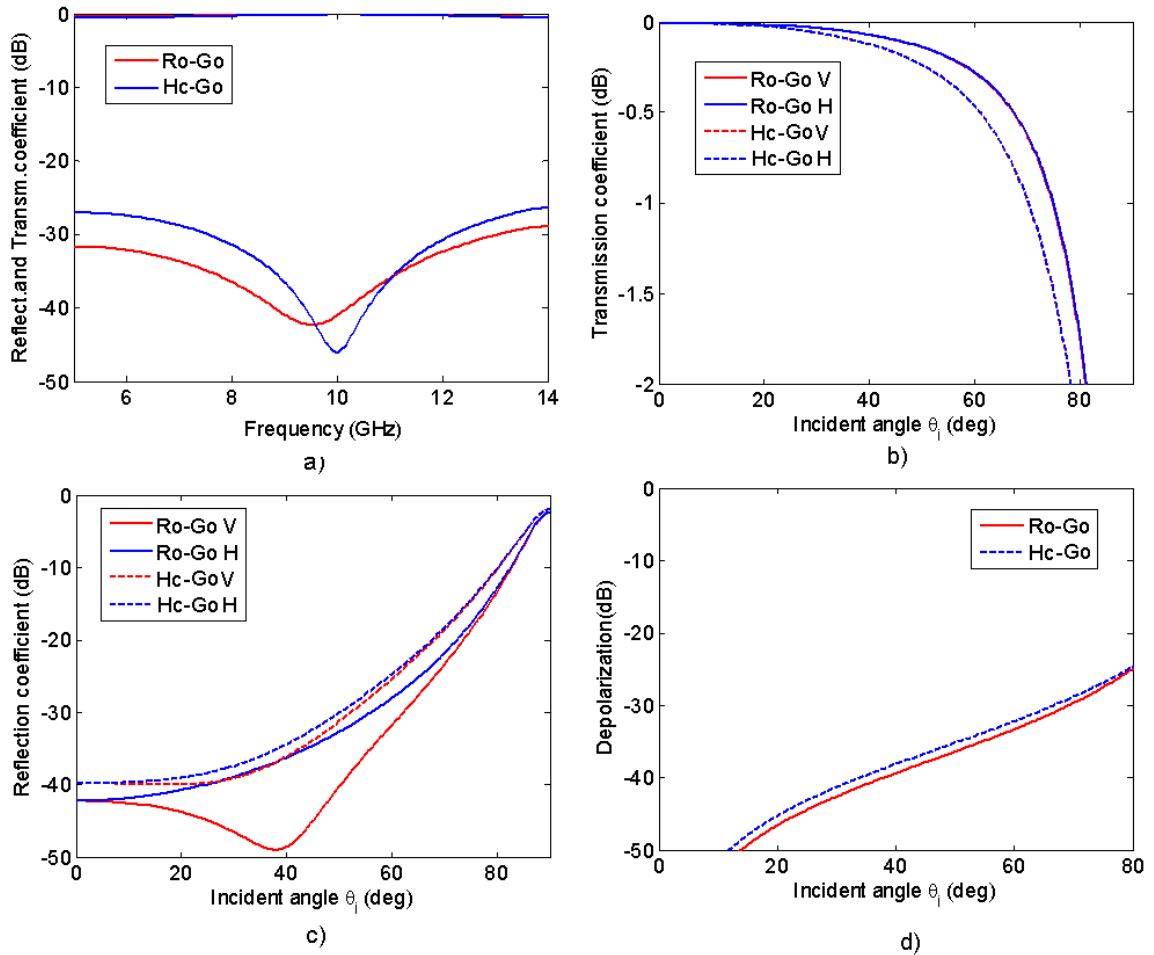
Figure 4.15. Calculated results of A-sandwich radomes using Gortex -Foam, and Gore- Honeycomb. a) Transmission and reflection coefficients versus frequency b) Reflection coefficients versus incident angle (azimuth plane) for H and V. c) Transmission coefficients versus incident angle (azimuth plane) for H and V. d) Cross poalrization depolarization ratio versus incident angle (azimuth plane)

used corresponds to a modified version of the Jerusalem Cross, which is been used for dual-polarized applications [65]. The shape differs from the conventional Jerusalem Cross shape in the additional transmission lines added between the "arms" of the cross, this in order to add capacitances that help obtaining the target resonant frequency for a given unit cell size of D_x=17 mm, D_y=17 mm (See Figure B.1). Figure 4.16 a) Shows results for transmission and reflection coefficients versus frequency. At 9.36 GHz, insertion losses equal -0.09 dB and a reflection coefficient of -47 dB exists for both polarizations (V and H). At a -10 dB return loss, the modified Jerusalem Cross shape can operate in a range of 3.5 GHz (7.5 GHz to 11 GHz). Figure 4.16 b) an d) show transmission and reflection coefficients versus incident angle in the azimuth plane for both polarizations. For the H polarization, the reflection and transmission coefficients are significantly affected in comparison with the V polarization. This can be attributed to the projections of electric fields in H with respect to the incident angle in the azimuth plane. The transmission and reflection coefficients can permit acceptable values for an incident angle of 30° with the level of depolarization constrained to scanning in a maximum range of 5°.

4.3.5   Transmit and Receive (T\R) module

A set of Transmit and Receive (T\R) modules controls the scanning capability of a phased-array radar system. The cost of these key modules represents about 45 % of the overall radar cost. Based on the antenna array architecture proposed, only 64 T\R modules are required to excite the antenna array, which offers the advantage of making more area available for T\R module board design. This enables more flexibility for increasing power per T\R module and adding to radar functionality.

With respect to radar requirements described in Chapter 2, each T\R module must provide a transmit power of 1.0 W to satisfy the requirement of having a total transmit power higher than 50 W. In the reception mode, the noise figure required
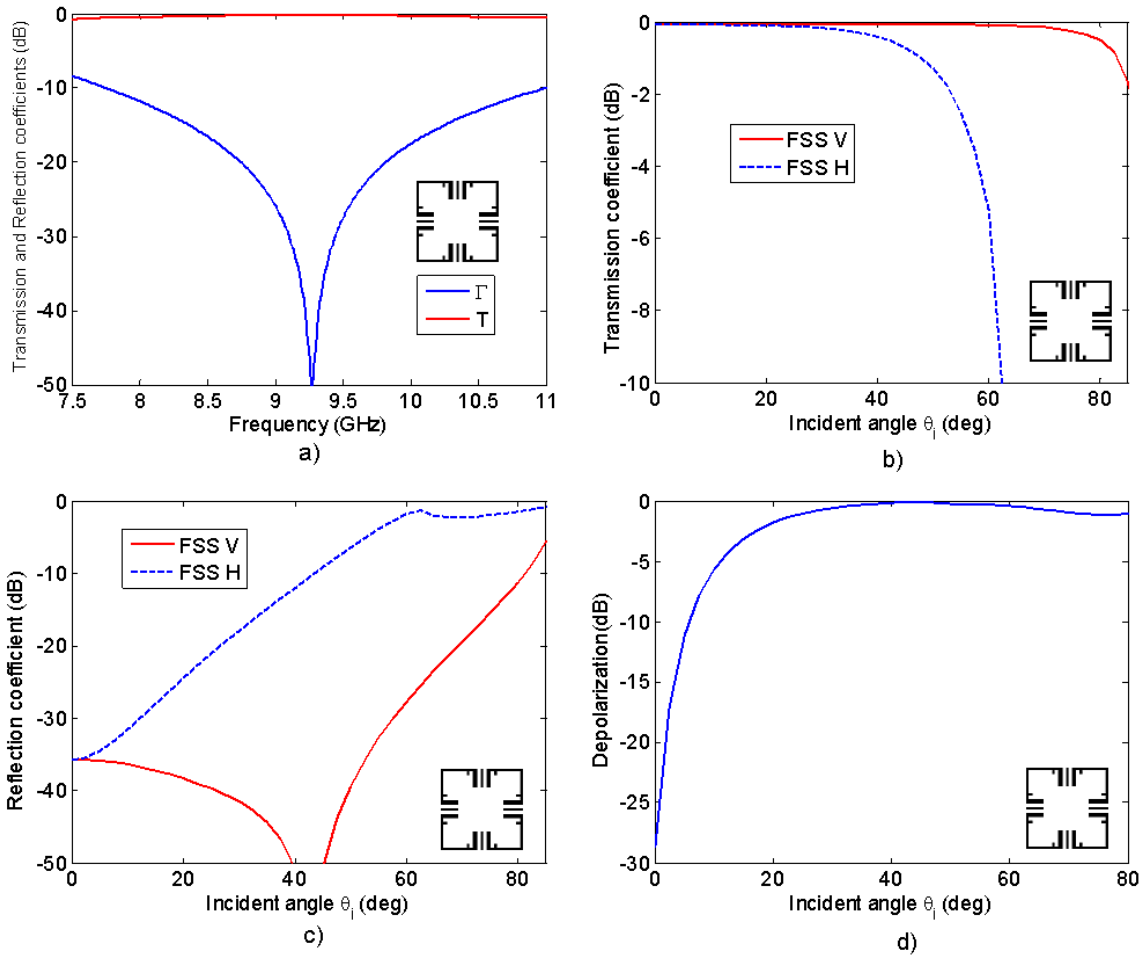
Figure 4.16. Simulated results of FSS sandwich radomes using Goretex, Rogers and Nelco SI. a) Transmission and reflection coefficients versus frequency b) Transmission coefficients versus incident angle (azimuth plane) for H and V. c) Transmission coefficients versus incident angle (azimuth plane) for H and V. d) Depolarization ratio versus incident angle (azimuth plane)

must be better than 5 dB and a switching capability with port isolation better than -20 dB is required to support the Alternate transmit and Alternate Receive polarization mode.

A beam steering resolution (θ_{sr}) of 1° is required for the CASA radar system in order to provide continuous sampling in the azimuth plane considering a 50 % overlapped beam. To provide a mean spatial resolution of better than 500 m, the antenna aperture size has been designed to provide an antenna beamwidth of 2°(in azimuth plane). Obtaining the minimum number of bits in the phase shifter requires that a phase shift ($\Delta\phi_s$) to obtain a 1° beam position must be less than the phase-shifter resolution $\Delta\phi_{FS}$ defined in Equation (7.30) in [36]

$$\Delta\phi_s < \Delta\phi_{FS} \tag{4.16}$$

$$kd\sin(\theta_{sr}) < \frac{2\pi}{2^N} \tag{4.17}$$

where $k=2\pi/\lambda_o$, $d_x=0.53\lambda_o$ and $\theta_{sr}=1°$. Solving equation 4.18 for N we can find the expression that defines the minimum number of bits in a phase shifter.

$$N > \ln_2\left(\frac{2\pi}{Kd_x\sin\theta_{sr}}\right) \tag{4.18}$$

Substituting the respective values for k, d and θ_{sr}, the minimum number of bits required in a phase shifter is 7.

A large number of bits in the phase-shifter provides better resolution and less quantization errors induced in the amplitude and phase excitation. However choosing the larger number of bits in the phase-shifter or attenuator can increase insertion losses and the costs significantly.

To define the minimum number of bits in a digital attenuator, the expressions (7.31) and (7.32) in [36] relating the peak sidelobe to the number of bits in an attenuator can be used. A digital attenuator of 5 bits is required for achieving -25 dB sidelobes.

A block diagram of the TR module proposed is given in Figure 4.17. The T\R module uses a "Common Leg" configuration that permits sharing the phase shifter and attenuator for transmission and reception paths [59].
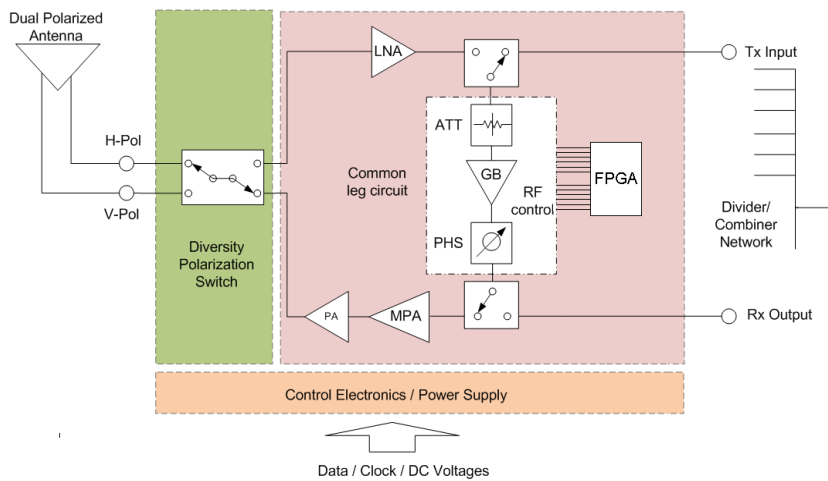
Figure 4.17. Block diagram of the T\R module

This configuration was selected to achieve the polarization mode required (ATAR) and while minimizing the most expensive component in the T\R module (7-bit phase -shifter). The T/R module RF subsystem requires a design using commercial-off-the-shelf (COTS) GaAs MMICs, produced at low cost, high reliability, and high volume.

4.4   Conclusion

The design of the antenna array for the CASA phased-array antenna was presented. The antenna aperture consist in a uniform rectangular array composed of 64 elements in the azimuth plane and 32 elements in the elevation plane. In the elevation

plane a subarray of 32 elements interconnected in a series-fed network is considered. Each subarray or column is exciting by a T\R module which provides amplitude, phase and polarization diversity.

A novel antenna array architecture which provides dual-polarized capability was designed and implemented in a multilayer structure. The radiating antenna element is dual-polarized aperture coupled microstrip patch antenna which is excited with two orthogonal dog-bone slots arranged in T-configuration. The antenna element presents excellent performance in gain and cross-polarization and is ideal for of a series-fed linear array antenna. A center and symmetric series-feed network were used to interconnect the 32 element array in the elevation plane.

A customized synthesis method was implemented to obtain the geometry dimensions of the linear antenna array geometry according with Taylor -25dB ($\overline{n}$=4) amplitude taper distribution to obtain -25 dB sidelobe level. The model was implemented in Matlab using a transmission line circuital model and then it was validated with simulated and measured results. The maximum number of elements that can be synthesized using this method is 32 elements. For a higher number of elements, the losses in the dielectric and serpentine lines demand large slot apertures, which are not practical considering the limited space due to the need for serpentine lines for both polarizations. Another factor that limits the maximum number to 32 elements is the maximum size for which a multilayer PCB fabrication process can be performed. Simulation process were performed in Ansoft Designer and HFSS. To include the effect of the mutual coupling in the azimuth plane. Two adjacent elements were incorporated in the design process.

To protect the antenna from the ravages of the environment, such as wind, snow, ice, rain and temperature changes, three wall radome designs based on foam, honeycomb and FSS were evaluated. A detailed radome design procedure for a multilayer

90

wall structure, which includes the formulation for attenuation, reflections and depolarization ratio is discussed.

A wall sandwich radome composed with a thick core dielectric material based on a foam and a skin hydrophobic material presented the optimal performance. The radome provides excellent electromagnetic transparence. The insertion losses were lower than -0.4 dB, the reflection was below -25 dB, and an induce cross-polarization ratio below -34 dB was obtained. The combination of Rohacell foam and Goretex provides a excellent thermal properties and mechanical strength. Goretex is designed to provide long durability (up to 40 years) and can provide a breaking load of 165 lb/in, good enough to support winds with speeds up to 200 mph.

CHAPTER 5

MEASURED PERFORMANCE OF THE CASA PHASED ARRAY ANTENNA PROTOTYPE

5.1 Introduction

This chapter describes the fabrication integration and testing of the antenna array prototype composed of 72x32 elements for CASA phased-array radar operating above 9.3-9.4 GHz. The low-profile antenna array (thickness $\approx 0.63\lambda_o$) was fabricated using a high quality printed circuit board fabrication process. This prototype is the first dual-polarized phased-array antenna that has been built and tested for weather radar applications, and in this regard serves handily as a proof of concept for a well-performing, low-cost alternative for weather radar systems. Figure 5.1 shows a picture of the full array antenna.

5.2 Linear array

The measurement results presented in this section will focus on the prototype that corresponds to a single LRU (18x32 elements). The size of the LRU was defined according to the maximum design size of the linear array antenna (discussed in Chapter 4) and also based on the maximum size permitted for a standard PCB fabrication process, which can permit high volume production lines. The PCB process was selected to permit a trace tolerance of about ± 0.8 mils, a route tolerance of about ± 5 mils, a minimum slot of 10 mils, and a lamination thickness tolerance of about ± 5 mils. These tolerances help to guarantee that the errors due to the manufacturing process do not exceed the maximum rms that the antenna array can tolerate to
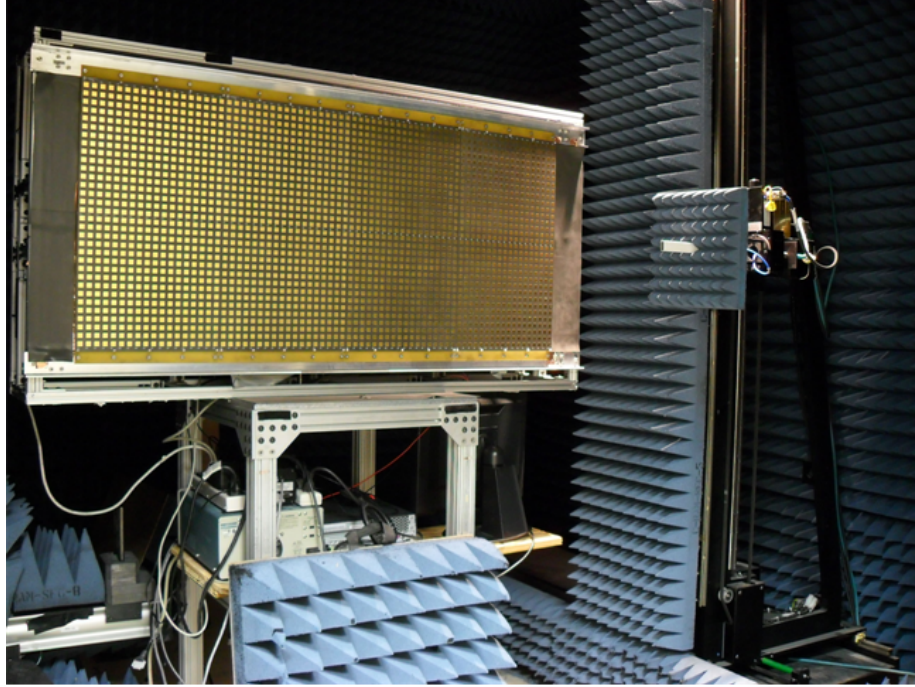
Figure 5.1. CASA Phased-array antenna in CASCA Near-field range at UMASS.

achieve the -25 dB SLL performance required. As depicted in Figure 5.2, the patch antennas were etched onto the side of 20 mil thick Rogers 5880. This layer was bonded with a 31 mil thick Rogers 5880 dielectric layer, where the two orthogonal dog-bone slots were etched on one side, and serpentine lines were etched on the other side. The bonding process was performed using 2 mil thick Gore Speedboard C prepreg LM (ε_r=2.15 and tanδ=0.00035) The antenna reflector array was etched in a 125 mil thick FR4 dielectric layer. The spacing between the antenna layer and the reflector layer was obtained using a high performance Rohacell 31 HF foam with a 250 mil thickness. The lamination of the antenna, foam and reflector layer was performed using a 2 mil thick epoxy glue.

Figure 5.3 presents the measured and simulated return loss and isolation of three columns (8, 9 and 10) embedded in panel 1 and panel 2. The return loss in V polarization shows good agreement between measured and simulated results using Ansoft
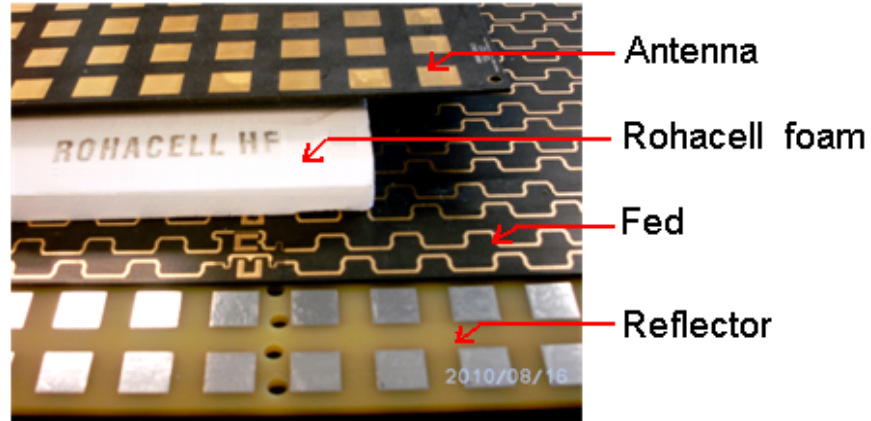
Figure 5.2. Representation of the differente layers in the antenna array. The Antenna and the fed is laminated. In the picture a second antenna was flipped to shows the series-feed art. The Rohacell foam is placed between the antenna layer and the antenna reflector layer.

Designer. However, in H polarization the return loss does not follow the characteristics of simulated results. It seems that the method used to include the mutual coupling in the characterization of the antenna impedance, adding two adjacent elements in the synthesis proposed, is not effective enough to incorporate the mutual coupling in the antenna characterization in H polarization. Even so, the measured return loss (for both polarizations) is better than -11 dB for the antenna bandwidth required (9.3 GHz -9.4 GHz). Isolation between H and V ports is better than -32 dB.

Figure 5.4 show the results of measured and simulated mutual coupling of the antenna array in azimuth plane. The simulation results were obtained using Ansoft Designer for a linear array of 18 elements in the azimuth plane, considering that the simulation of 18 columns (each with 32 elements) requires large computational resources. Besides the difference in the arrays, the measured and simulated results
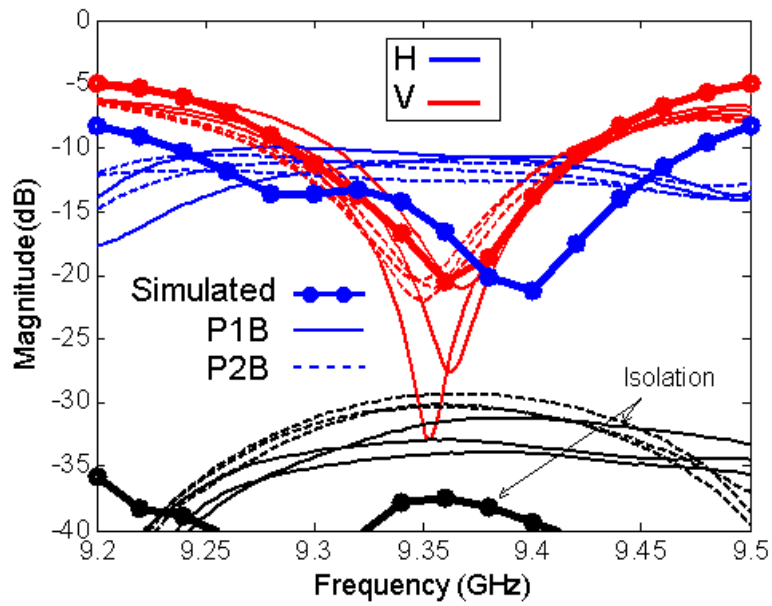
Figure 5.3. Measured return loss and isolation versus frequency for the embedded column 9, 10 and 11 compared with simulation results of isolated column in Ansoft Designer.

present similar characteristics. Stronger mutual coupling is observed for H polarization compared with the field in V.
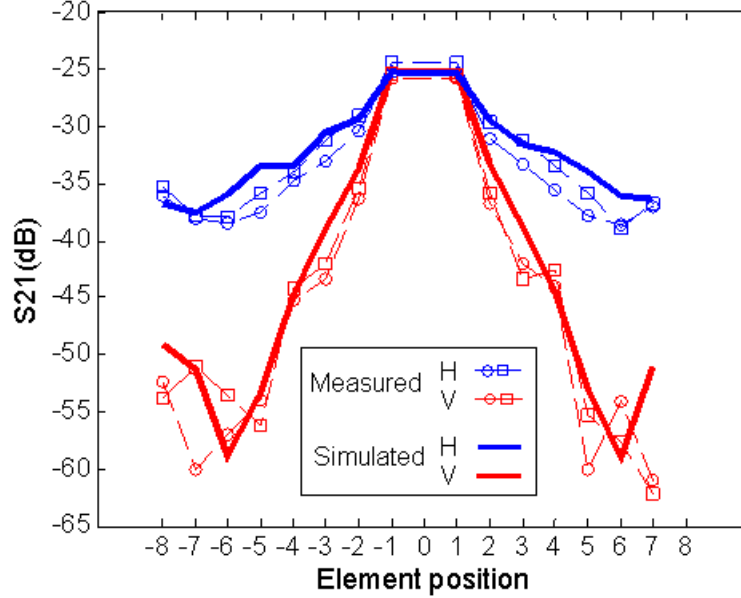
Figure 5.4. Measured mutual coupling in panels (P1B and P2B). Each LRU panel of 18 column of 32 antenna elements separated about $dx=0.53\lambda_o$ and simulated mutual coupling in linear array of 18x1 elements in azimuth plane for $dx=0.53\lambda_o$.

The measurement of antenna patterns was performed in the two antenna range systems of the Center for Advanced Sensor and Communication Antennas (CASCA) antenna laboratory at UMASS. The taper far-field range was initially used to evaluate the antenna patterns in the elevation plane and embedded element patterns in the azimuth plane. Even though the length of the chamber does not satisfy the minimum far-field distance for one LRU (panel of 18x32 elements), the resulting elevation patterns show characteristics similar to those of the simulated patterns. Figure 5.5 a) present results comparing a simulated isolated column to measured results for the 9th column embedded in an array of 18x32 elements. For both polarizations, the first sidelobe is below -25 dB and the sidelobe roll-off characteristic consistently follows simulated results, except at the ends where the edges of the antenna array affect the

last sidelobes. Figure 5.5 b) shows the cross-polarization performance of the eleva-
tion patterns. At broadside, a null with -38 dB in H and a null with -34 dB in V
are observed. Simulated cross-polarization values differ by about 4 dB (for H) and 2
dB (for V), which can be attributed to error in the alignment of the antenna and the
probe, and also to the diffracted fields at the edge of the array. This issue appears in
the next section in the discussion for the results of the embedded element pattern in
the array .

5.3   Planar array

The planar array is composed of 4 LRU array panels of 18x32 elements each. The
four LRU's were mounted in a prototype aluminum frame based on 80/20. Figure
5.7 shows a picture of the four antenna array panels (LRU's) integrated with the 64
T\R modules, backplane and manifolds. The T\R module is a result of a customized
design implemented in a printed circuit board (PCB) which comprises 6 circuit layers
fabricated on a hybrid construction of Rogers 4350 and FR4. A laminate of 10 mil
Rogers 4350 is used to implement the RF circuits with a coplanar transmission line
and a high power diversity switch. On the other hand, four FR4 laminates, including
the bonding adhesives, were used to implement the analog and digital ground/power
planes and to distribute the control signals. The RF components are commercial-off-
the-shelf (COTS) plastic packed microwave monolithic integrated circuits (MMICs)
that use Gallium Arsenide (GaAs) technology. The module has an enclosure weight of
140 g and has dimensions of 2.6 in x 4.41 in. The T/R module PCB is designed with
a low thermal impedance from the power amplifier footprint through the baseplate of
the board enclosure, which acts as a heat spreader, as shown in Figure 5.7. A thermal
patch isolates the PCB from the baseplate and avoids short-circuiting between them.
The maximum output power of this module (1.25 W) and the moderate duty cycle
of the radar (<30%) results in low average dissipated power, and hence leads to a
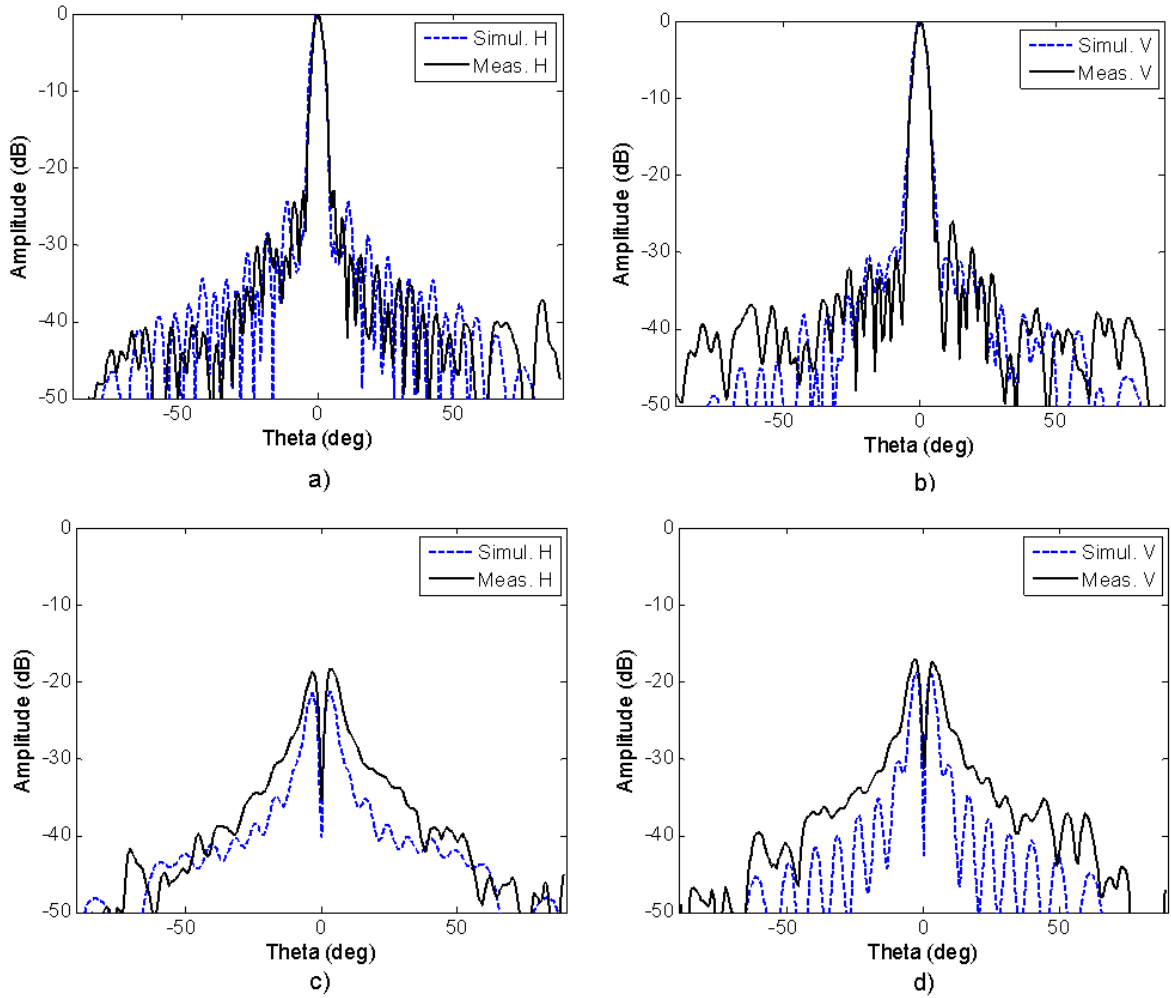
Figure 5.5. Elevation antenna array patterns. In blue simulation results of isolated column 18x1 array with infinite ground plane. In black measured patterns of embedded column 9th in an antenna array of 18x32 elements a) Co-polar for H c) Co-polar for V c) Cross-polar for H and d) Cross-polar for V.
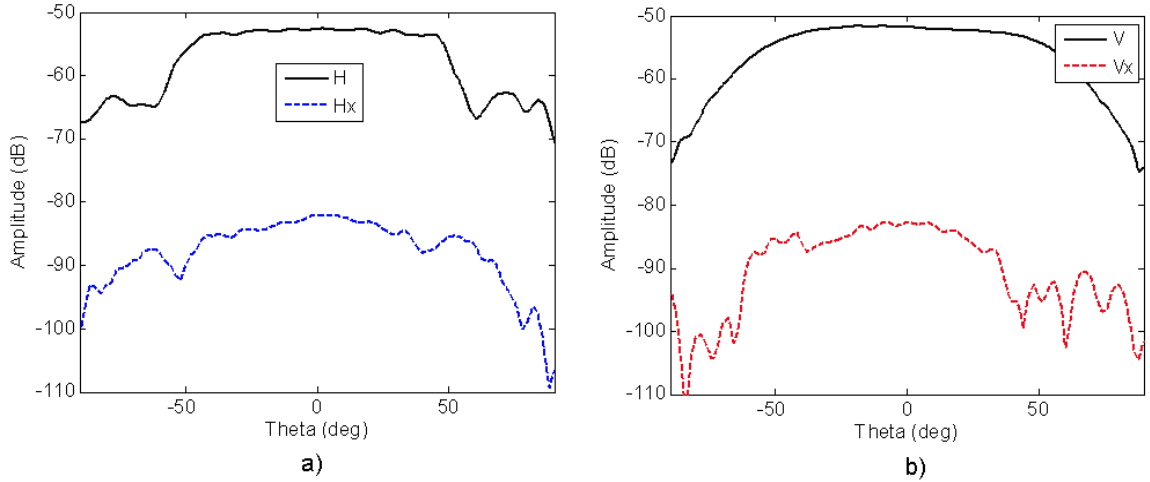
Figure 5.6. Measured embedded element pattern in column 9th in a LRU array of 18x32 elements. a) H polarization b) V polarization

relatively simple thermal design. Measured results of the T\R module parameters are detailed in Table 5.1. Details of the TR module measured performance is given by Medina at [59]

The next results correspond to the embedded element patterns in the array in the azimuth plane. Those measurements were initially taken in a taper far-field range system for one LRU without the T\R modules. The results are shown in Figure 5.6 for both polarizations, and these were used to correct the effects of the probe placed at $4\lambda_o$ from the antenna in the NSI planar near-field range system that belongs to CASCA antenna laboratory at UMASS.

Figure 5.8 illustrate the embedded element antenna patterns of a few elements (columns) in some specific places in the array (in azimuth plane) as it is indicated in Figure 5.10 a). Only 10 elements were measured due the limited time available for the measurements. The elements were strategically chosen in order to evaluate the effect of the discontinuities between panels, and also to evaluate the edge effects in the
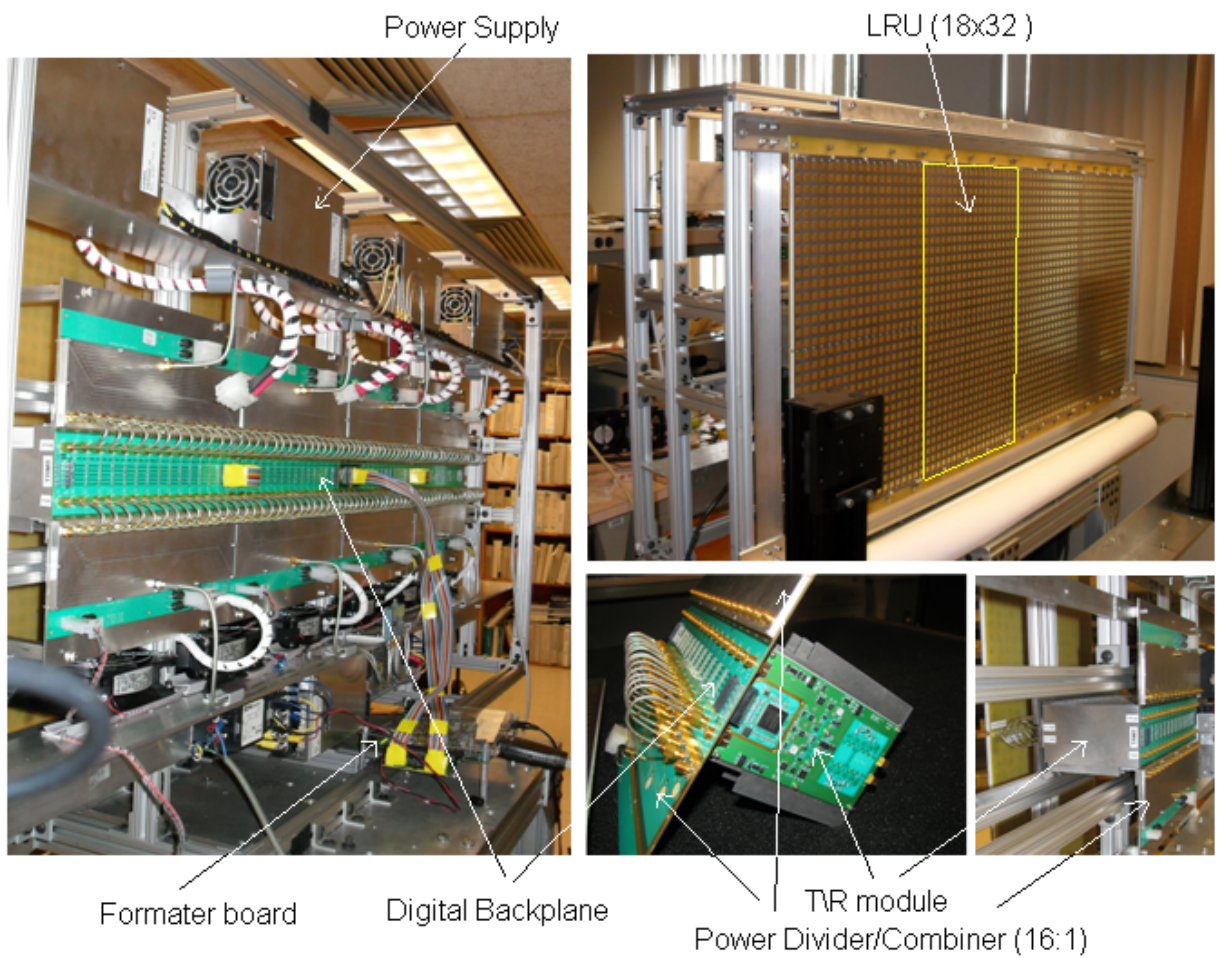
Figure 5.7. CASA Phased-array antenna integrated.

Table 5.1. T\R module measured performance

Parameter	Units	Value
Operational Frequency	GHz	9.36
Bandwidth	MHz	400
Tx. gain	dB	25.3
Tx. input return loss	dB	-13.9
Tx. output return loss	dB	-14.0
Tx. input 1dB comp.	dBm	4.0
Tx. saturation power	dB	31.0
Rx. Gain	dB	25.5
Rx. input return loss	dB	-13.6
Rx. output return loss	dB	-13.3
Rx. input 1dB comp.	dBm	-13.0
Minimum noise floor	dB	4.3
Isolation between Tx and Rx	dB	>62
Isolation between V and H	dB	>45
Module efficiency	%	<20

array. The element positions are also indicated in each plot, and these corresponds to the following elements: 10, 18, 19, 32, 36, 37, 41, 54, 55 and 63.

Figure 5.8 and Figure 5.9 show the embedded element patterns (co-polar and cross-polar) for the 10 elements considered. For all of them, the measured results show the presence of ripples in the co-polar patterns, where stronger ripples occurs when the antenna elements are polarized horizontally due the coupling of diffracted fields at the edges of the array. Figure 5.8 a-b) show the results for elements 10 and 63 (closest to the edges), the ripples are relatively high in both polarizations, about 2.4 dB for H and 1.4 dB in V. However, in the inner edges of each LRU (elements 18, 19, 54, 55, 36 and 37), the diffracted fields in the discontinuities between panels produce ripples of about 0.46 dB for H and 0.15 dB for V. As expected, the ripples are lower in the center of each LRU. The average values between elements 32 and 41 represent ripples with magnitudes on the order of 0.40 dB and 0.13 dB (for H and V respectively). Table 5.2 summarize the amplitude of the ripples measured (peak to peak) for each of the

10 elements measured. Regarding the cross-polarization performance, it seems that the diffracted fields produced in the internal and external edges of each LRU affect the cross-polar components oriented in horizontal polarization (Vx). In all embedded element patterns, the cross-polarization is higher in Vx than in Hx. Figure 5.10 shows a diagram of the position of the elements in the array. An overlapped element pattern for H and V is shown, as well as the respective average patterns of the 10 elements for H and V respectively.

Figure A.1 present the measured elevation antenna patterns (for H and V) for the lower (9.3 GHz), center (9.36 GHz) and upper frequency (9.4 GHz) of the required bandwidth (100 MHz). For all frequencies, the patterns show a well defined main beam with enough low SLLs to satisfy the radar requirements. Figure A.2 a) show the measured embedded element patterns (for H and V) for the lower (9.3 GHz), center (9.36 GHz) and upper frequency (9.4 GHz). Small variation in the ripples is observed as function of frequency. Figure A.2 b) shows the active reflection coefficient for all frequencies (between 9.3 GHz and 9.4 GHz) and also as function of scan angle (azimuth plane). This parameter was calculated based on the measured active element pattern, using the expression 37 in [50]. For the entire scanning rage ($\pm 45°$) a maximum reflections of -10 dB can be produced for 100 MHz bandwidth operation.

Figure 5.11 presents antenna measured patterns of the full phased-array antenna in the azimuth plane. A calibration process for the phased array was performed in a near-field antenna range. During this process, a sampling probe is positioned in front of each radiating element, with that element in either transmit or receive mode and the remaining array elements terminated in matched loads. The amplitude and phase of each radiating element is accurately measured through each T/R module amplitude, phase state amplitudes and phases as indicated by the measurements. The temperature dependence on the s-parameters is entirely dominated by the active components of the antenna, since the temperature variability associated with the RF
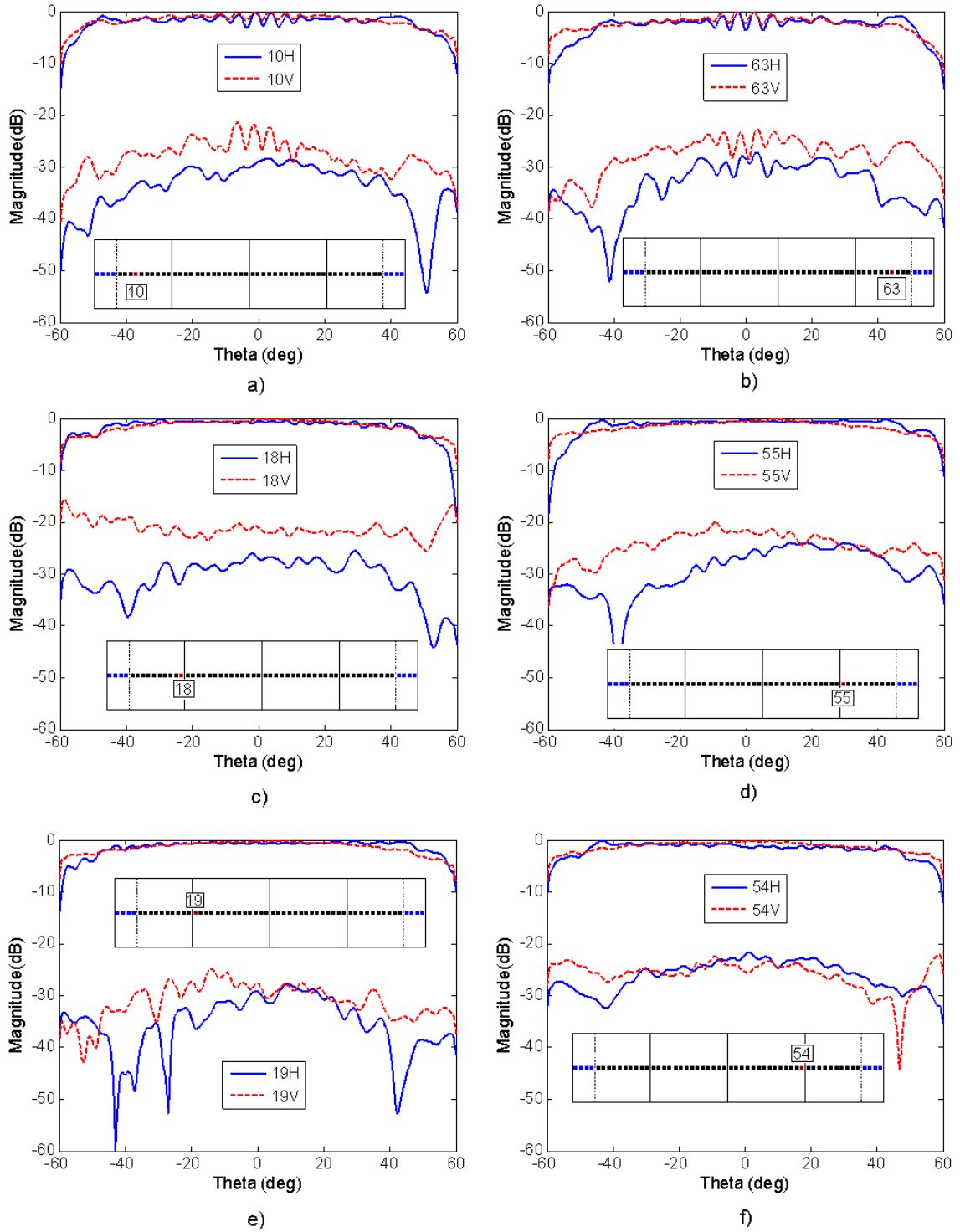
Figure 5.8. Measured embedded element patterns for: a) Element 10 b) Element 63 c) Element 18 d) Element 55 e) Element 19 and f) Element 54.
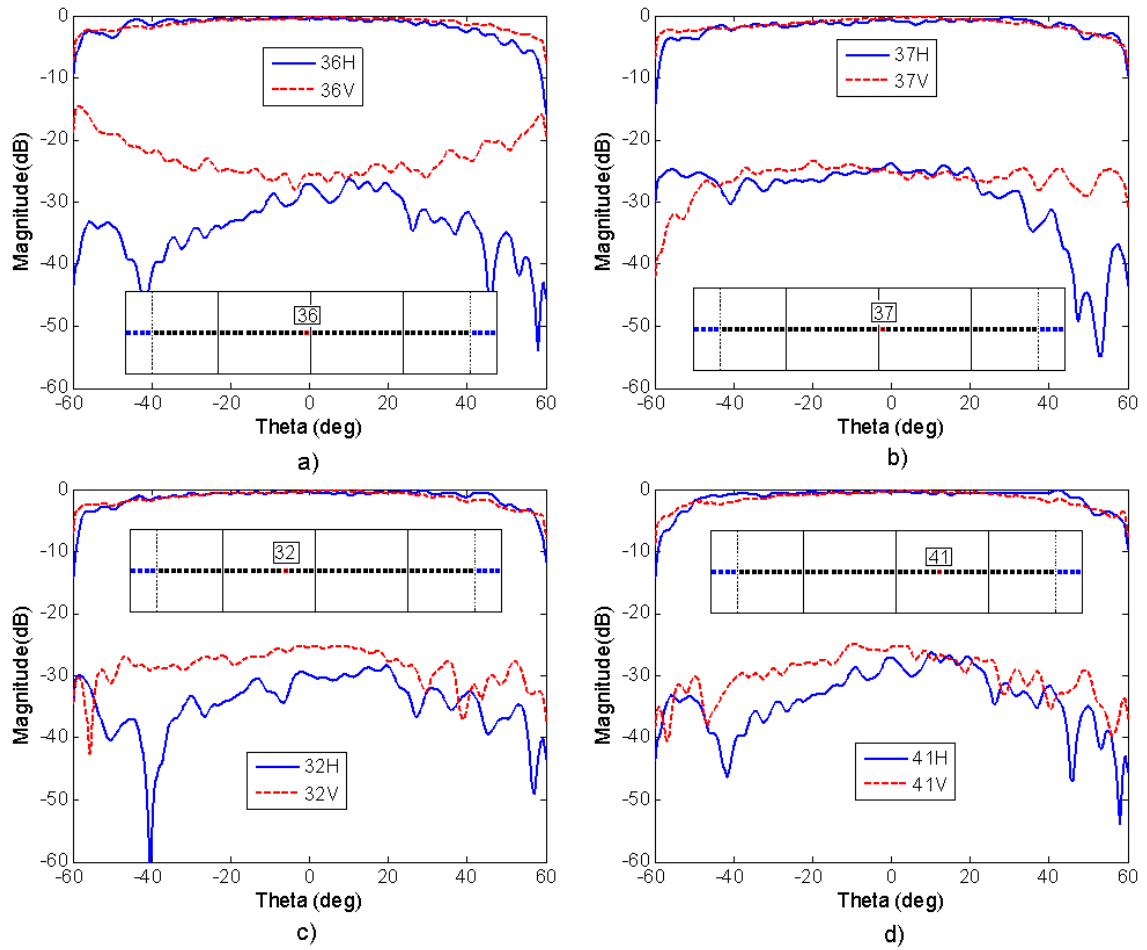
Figure 5.9. Measured embedded element paterns for: a) Element 36 b) Element 37 c) Element 32 d) Element 41 and e) Average
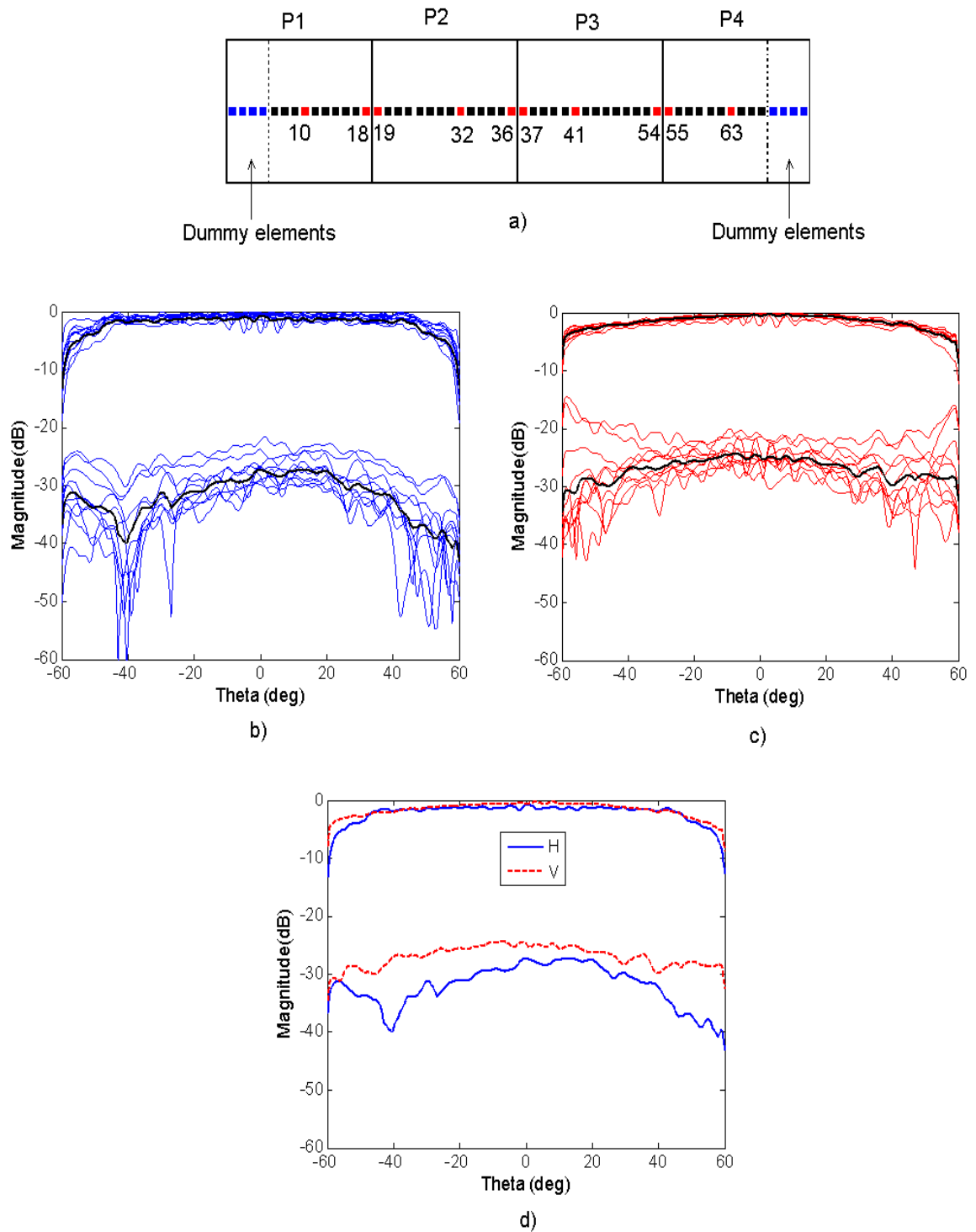
Figure 5.10. Measured embedded element patterns. a) Positions of elements measured b) Pattern of embedded elements: 10, 18, 19, 27, 32, 36, 37, 54, 55 and 53 in H polarization and c) Pattern of embedded elements: 10, 18, 19, 27, 32, 36, 37, 54, 55 and 53 in V polarization and d) Average of embedded patterns for H and V polarizations.

105

Table 5.2. Ripples performance in embedded element patterns

Region	Element	Ripples (dB) H	Ripples (dB) V	Ripples (dB) (Average) H	Ripples (dB) (Average) V
External edge (left)	10	2.58	1.59	2.41	1.43
External edge (right)	63	2.24	1.27		
Internal edge	18	0.56	0.05		
Internal edge	55	0.41	0.24		
Internal edge	19	0.60	0.20	0.46	0.15
Internal edge	54	0.40	0.05		
Internal edge	36	0.23	0.15		
Internal edge	37	0.53	0.18		
Center element (LRU$_2$)	32	0.51	0.09		
Center element (LRU$_3$)	41	0.30	0.17	0.40	0.13
Average				0.84	0.39

manifolds, cables and the antenna panel is negligible over the T/R module. Therefore, a simple cooling fan system that controls the T/R module temperature is enough to mantain the s-parameters at values associated with different constant temperature values.

Antenna patterns for scanning positions 0°, 15°, 30° and 45° were taken in reception mode, and for both polarizations were calibrated for an amplitude taper distribution which corresponds to Taylor -25 dB for $\bar{n}=4$. Figure 5.11 and Figure 5.12 show the measured (co-polar and cross-polar) patterns normalized to broadside beam for H and V polarizations. The first sidelobe levels for both polarizations are below -25 dB, except at 15° and 30° in V polarization, where the first sidelobe levels are 1.8 dB higher (-23.2 dB). The sidelobe roll-off for H and V decrease from the main beam, indicating small errors in the excitation of the array elements. The cross-polarization levels corresponding to each beam position are below -30 dB for H polarization and below -27 dB for V polarization. Figure 5.13 shows the overlapped scanned beam patterns (co-polar and cross-polar) in the azimuth plane for H and V polarizations,

with the embedded element patterns of the 32nd column and the average of the 10 elements. The plots indicate the main beams and cross-polar beams follow the shape of the embedded element patterns.

Table 5.3. Scanning performance Phased-array antenna in azimuth plane

Scan	H-polarization					V-polarization					
	θ_{3dB}	Eco_n	Ex_n	SLL_1	θ_S	θ_{3dB}	Eco_n	Ex_n	θ_s	SLL_1	MM
	(°)	(dB)	(dB)	(°)	(dB)	(°)	(dB)	(dB)	(°)	(dB)	(%)
$\theta_s = 0°$	1.77	0.00	-29.9	-25.5	0.0	1.77	0.00	-27.5	0.0	-25.1	1.2
$\theta_s = 15°$	1.79	-0.23	-32.4	-25.2	15.0	1.79	-0.09	-27.0	15.0	-23.2	1.8
$\theta_s = 30°$	2.05	-1.12	-36.9	-24.6	30.0	2.05	-0.86	-27.8	30.0	-23.3	4.8
$\theta_s = 45°$	2.45	-2.53	-51.7	-26.1	44.7	2.45	-2.05	-31.8	44.7	-25.1	7.2

Figure 5.14 illustrate the co-polar array antenna patterns for the full array of 64x32 elements. The array patterns in V were normalized to H polarization in order to estimate the mismatch co-polar patterns assuming the variations in gain in H and V due to the ripples were calibrated. The results (also presented in Table 5.3) shows that measured mismatch between co-polar patterns is lower by 7.2 % when the antenna is scanned from broadside to ±45°.

5.4   Radome

Figure 5.15 a-b) shows the two sandwich wall structure radomes implemented and tested according to the procedure and design considerations presented in section 4.2.4. Both radomes composed of Rohacell-Goretex (Ro-Go) and Rohacell-Honeycomb (Ro-Hc) were laminated using a thin layer (~2 mil) of epoxy glue. Better lamination was obtained with the Ro-Go since a larger contact surface is obtained compared to Ro-Hc. The first test consisted of measuring antenna patterns without the radome and then with both radomes. The center embedded element pattern corresponding to the 9th column in the LRU array (18x32 elements) was measured in the taper far-field
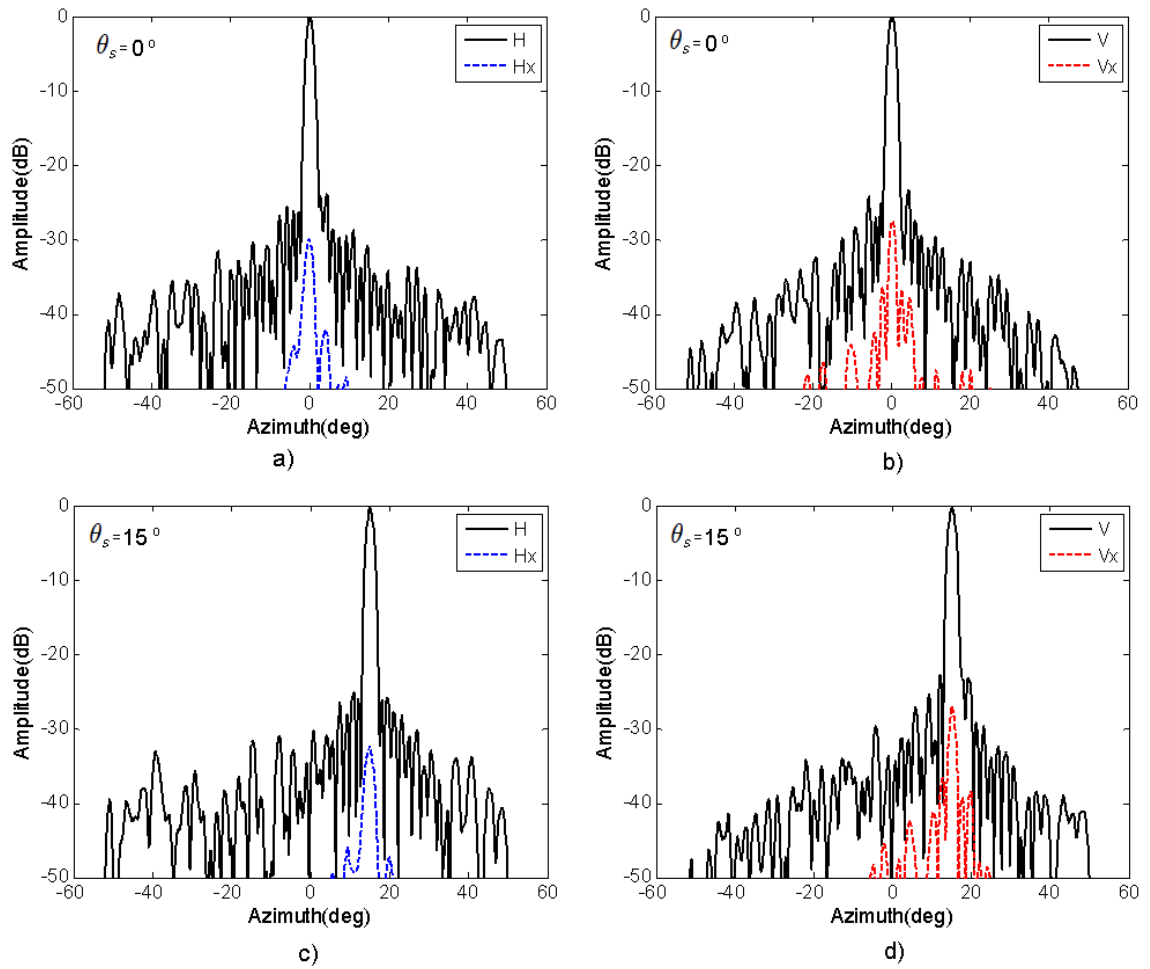
Figure 5.11. Measured patterns of phased-array (64x32 elements) in the azimuth plane for a-b) θ_s =0° c-d) θ_s =15°
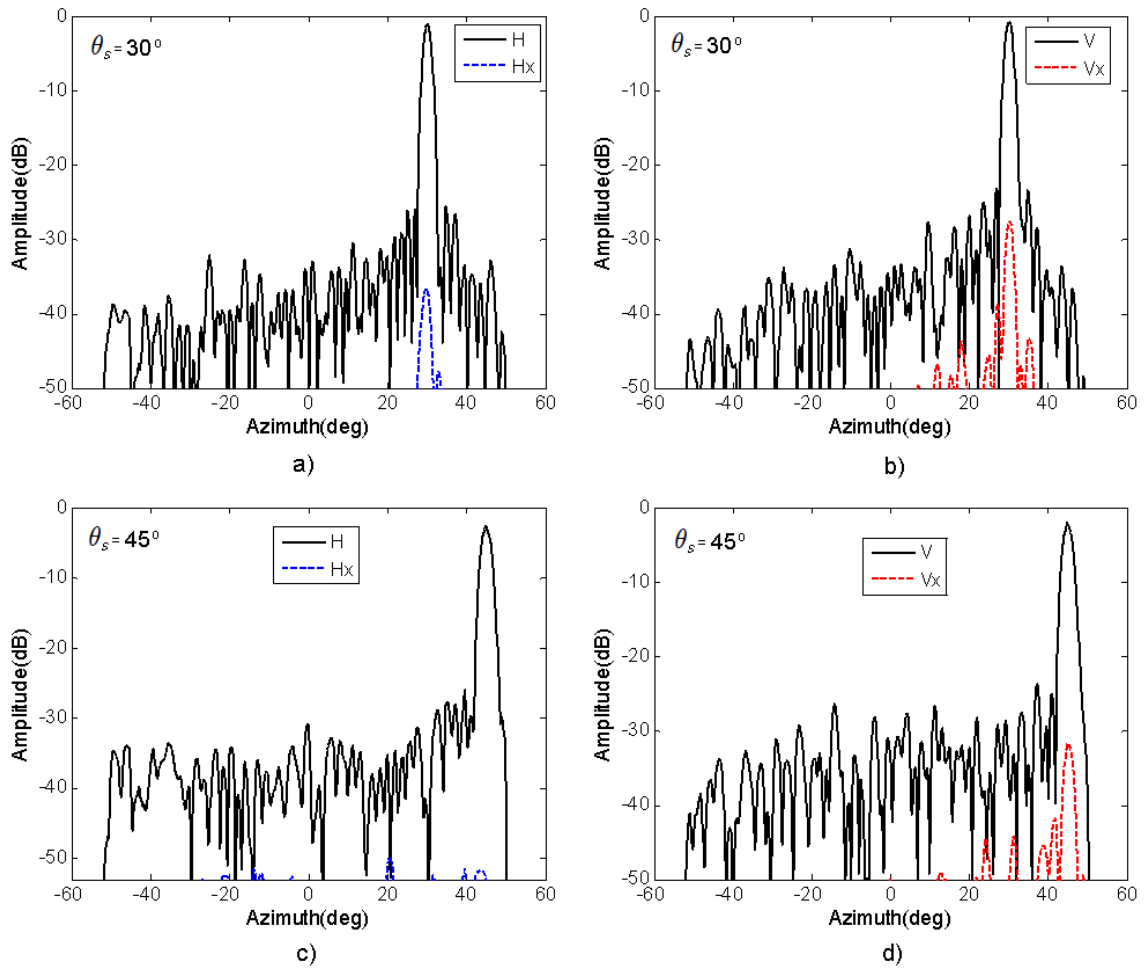
Figure 5.12. Measured patterns of phased-array (64x32 elements) in the azimuth plane for a-b) $\theta_s = 30°$ c-d) $\theta_s = 45°$
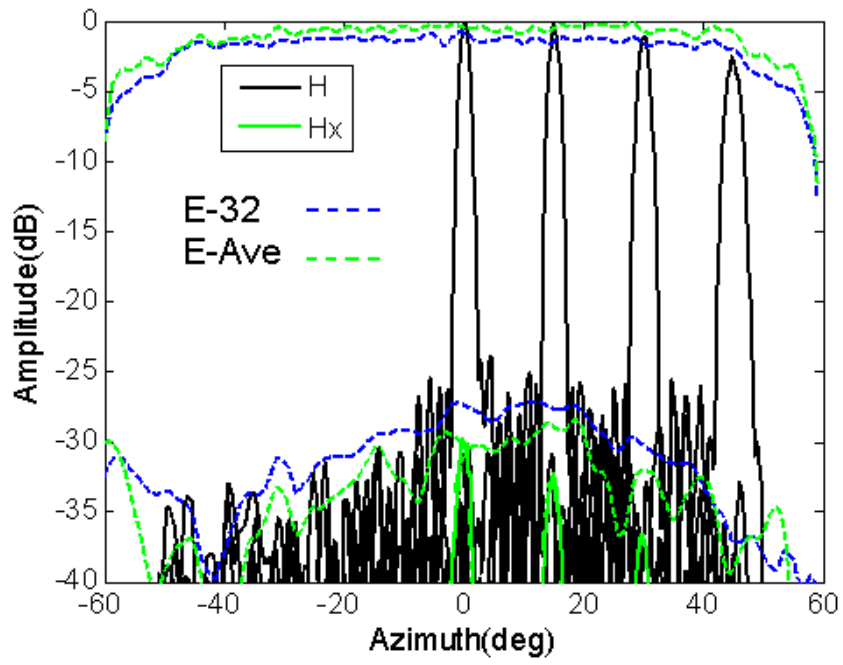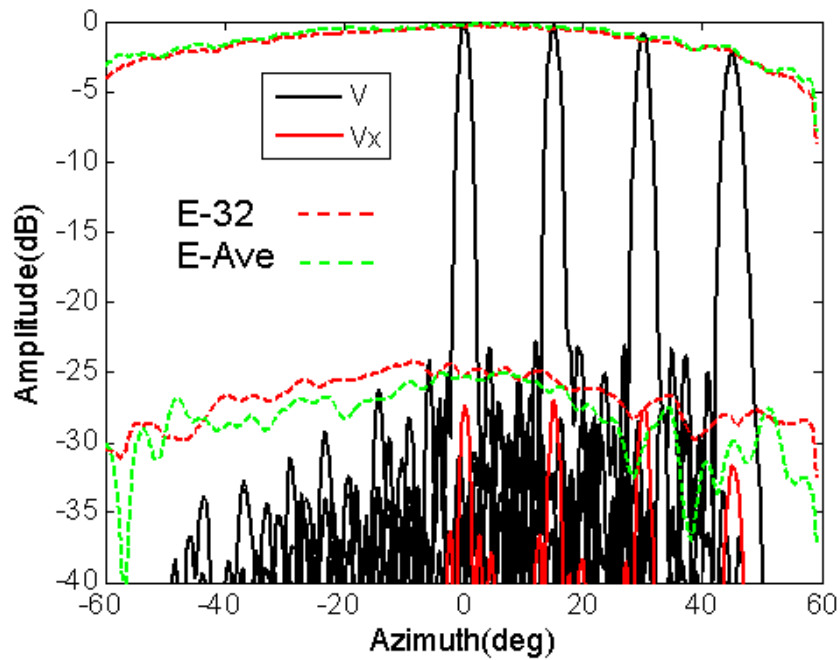
Figure 5.13. Measured scanned antenna patterns in azimuth plane overlapped with embedded element pattern of column 32 and also with average element pattern for H and V polarization

110
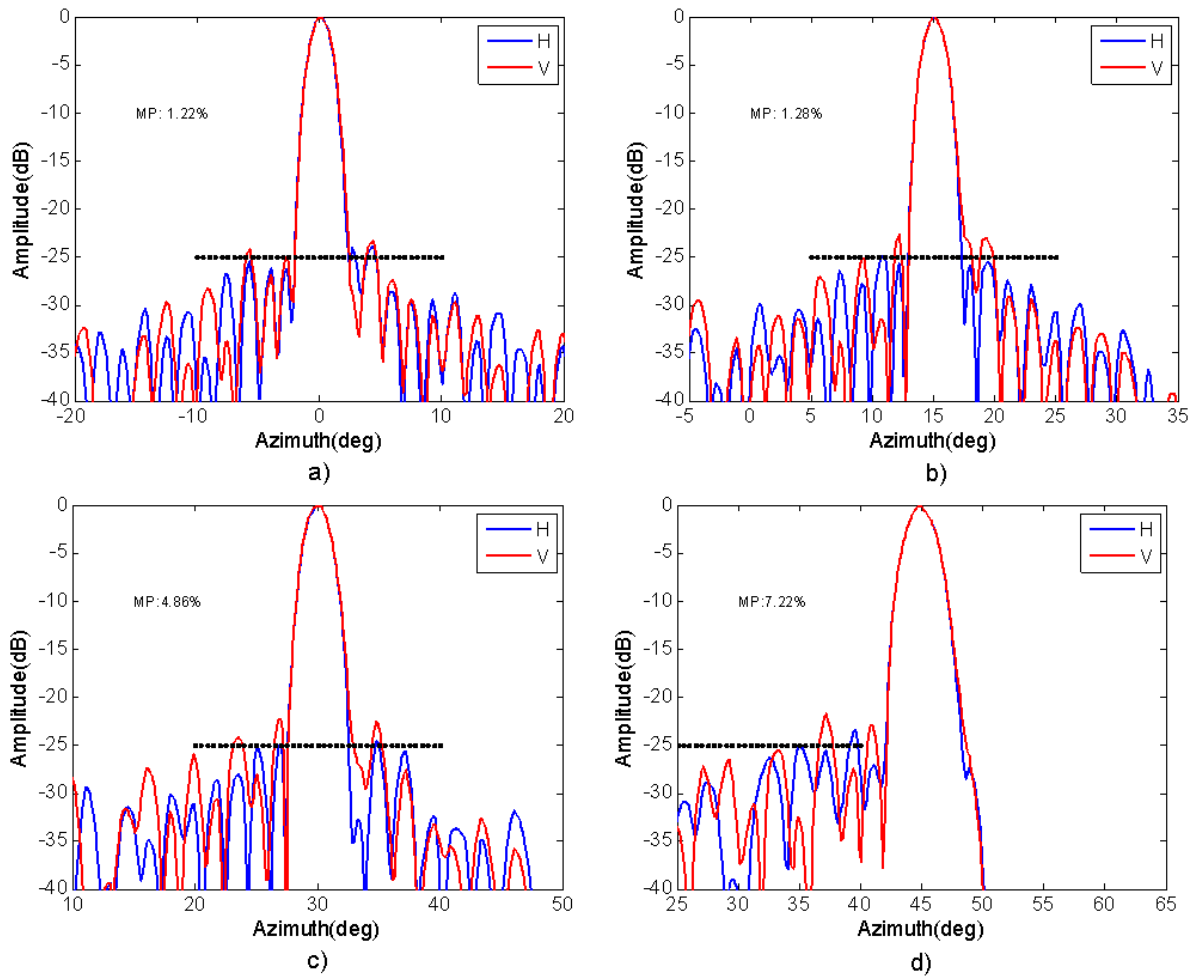
Figure 5.14. Measured mismatch between normalized co-polar array antenna patterns of full array (64x32 elements). a) $\theta_s = 0$ °, b) $\theta_s = 15$ °, c) $\theta_s = 30$ ° and d) $\theta_s = 45$ °

range system. Figure 5.15 b-c) presents the measured far-field patterns of the 9th embedded element for H and V polarization. Numerical results are summarized in Table 5.4. For both polarizations, the radome Ro-Go shows lower losses in comparison with Ro-Hc. The effect of the radomes on cross-polarization is insignificantly small (about 1 dB higher). The radome based on Ro-Hc show larger losses in H (about 1.1 dB higher than V). One reason for this difference could be the asymmetry in the honeycomb cells. A smaller cell size in the H direction is observed compared to the V direction, and this difference suggest that the effective dielectric constant in H can be higher, since more walls of Aramid-fiber are present for the same unit of length in both directions.

Table 5.4. Radome performance in embedded element pattern 9th in LRU (18x32 elements)

	Losses for H (dB)				Losses for Hx (dB)			
Radome	0°	15°	30°	45°	0°	15°	30°	45°
Ro-Go	-0.02	-0.03	-0.05	-0.21	-0.36	-0.20	-0.27	-0.4
Ro-Hc	-1.13	-1.17	-1.08	-1.23	+1.17	+1.09	+0.96	+0.56
	Losses for V (dB)				Losses for Vx (dB)			
Radome	0°	15°	30°	45°	0°	15°	30°	45°
Ro-Go	-0.03	-0.02	-0.01	-0.15	-0.41	-0.12	-0.5	-0.64
Ro-Hc	-0.01	-0.04	-0.01	-0.09	-1.21	-0.84	-1.02	-1.19

Figure 5.15 b-c) corresponds to a far-field pattern for the full array taken in the NSI near-field range system in the azimuth plane for H polarization. Only two scanning positions ($\theta_s=0°$ and $\theta_s=45°$) were measured. Both co-polar and cross-polar patterns are slightly affected by the radome. In the main beam a loss in broadside of about -0.02 dB was observed, and at $\theta_s=45°$ a loss of -0.34 dB was observed. The cross-polar patterns are affected in less than 3 dB in the sidelobe regions.
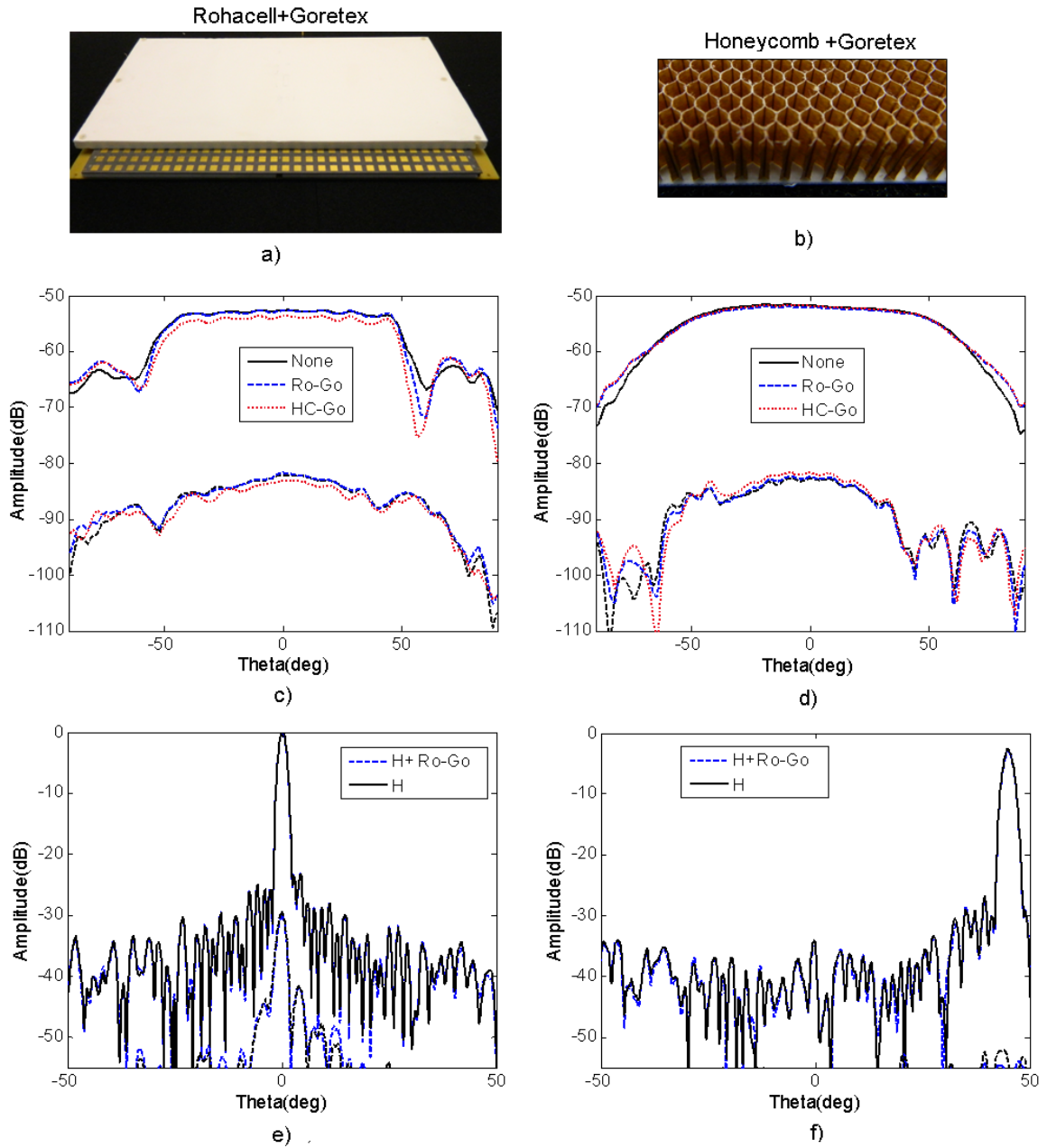
Figure 5.15. Antenna radome implementation and measured results. a) Ro-Go radome b) Ro-Hc radome c-d) Embedded element pattern of column 9th in array of 18x32 elements with and without radomes for H and V polarizations respectively. e-f) Measured azimuthal pattern in the full array (64x32 elements) with and without radome (Ro-Go) at $\theta s=0°$ and $\theta s=45°$ in H polarization only.

5.5 Conclusion

The entire array was fabricated as a multilayer PCB and assembled as a set of modular 18x32 sub-panels. The results (s-parameters and radiation patterns) presents good agreement with calculated and simulated results. A small disagreement between the measured and simulated results in the return loss for H-polarization can be attributed to how the antenna impedance versus slot length was characterized. It seems that using only two adjacent elements to include the mutual coupling effect was not the correct approach. Besides this disagreement, the return loss in H polarization are better than -11 dB for the bandwidth required (9.3 GHz to 9.4 GHz).

Measured antenna patterns of the passive array antenna panels (18x32 elements) were first measured in the taper anechoic chamber of the CASCA antenna laboratory at UMASS. Even though the length of the chamber does not satisfy the minimum far-field distance for the antenna size, the resulting elevation patterns show good matching with simulated and calculated patterns. For both polarizations, the first sidelobe is below -25 dB and the sidelobe roll-off characteristic consistently follows simulated results, except at the ends where the edges of the antenna array affect the last sidelobes. At broadside, a null with -38 dB in H and a null with -34 dB in V are observed. Simulated cross-polarization values differ by about 4 dB (for H) and 2 dB (for V), which can be attributed to error in the alignment of the antenna and the probe, and also to the diffracted fields at the edge of the array.

Full array (64 columns with 32 elements each plus 8 columns as dummy elements) were measured in the Near-Field range chamber of the CASCA antenna laboratory at UMASS. The cross-polarization for each beam position (0 °, 15 °, 30 ° and 45 ° in the azimuth plane) are below -25 dB (5 dB better than required). The peak sidelobe level is below -23 dB (2 dB, worse than required for CASA weather radar). The measured results shows that the mismatch between co-polar patterns is lower by 7.2 % when the antenna is scanned from broadside to ± 45 °.

Embedded element antenna patterns for 10 of thr 64 elements were measured in the Near-Field range chamber. The purpose of these measurements was to characterize the ripples produced by the surface waves at the edges of the antenna array (internal and external edges). The position of the elements (or columns) was selected such that both middle and edge elements of each panels were tested. The highest ripples observed were 2.58 dB for H polarization and 1.59 dB for V polarization. In elements near to the internal edges (panels 18x32), the average ripple values observed were 0.46 dB for H and 0.15 dB for V. And the average values of ripples for elements in the center of each panel is 0.40 dB for H and 0.13 dB for V. while the averge amplitudes across the 10 elements were about 0.84 dB for H and 0.39 dB for V.

With respect to the cross-polarization for V, an increment of ~10 dB was produced in elements 18, 36 and 54 in the scanning range region between 40 ° to 60 ° . This effect can be attributed to the diffracted fields produced by the discontinuities between panels.

The measured antenna of the full array were overlapped with the center embedded element patterns and also with the average antenna element pattern. The main beam and cross-poalrization patterns follow consistently with the embedded element antenna patterns.

The active reflection coefficients versus frequency and scan angle were estimated from the embedded element patterns. Values below -10 dB were obtained for a scanning range of ± 50 ° and a required frequency range between 9.3 GHz to 9.4 GHz.

Two- wall radomes using Goretex and foam Rohacell and Goretex and Honeycomb were implemented and tested. Measured antenna patterns of the embedded element pattern, elevation patterns and azimuth patterns were performed with and without the radomes. The radome based on Goretex and foam Rohacell consistently presents the better electrical performance based on both the calculated and simulated results. At 45 ° it attenuates about -0.21 dB for H and -0.15 dB for V, with less than 0.5 dB

variation with respect to cross-polarization values. Scanned measured patterns in H polarization at 45 ° presents an attenuation of -0.34 dB and a variation of less than 3 dB of the cross-polarization.

CHAPTER 6

RADAR PREDICTED PERFORMANCE

6.1 Introduction

In this chapter the predicted performance of the polarimetric CASA phased array radar as a function of the scanned measured antenna patterns is presented. The measured patterns in combination with predicted antenna patterns based on the measured embedded element patterns were used to estimate the accuracy of the two polarimetric radar parameters (Z_{dr} and ICPR$_2$). In Chapter 2, the minimum requirements for a polarimetric radar using the ATAR polarization radar mode to achieve less than 0.2 dB errors in the Z$_{dr}$ were presented. In this chapter, an accurate representation of the antenna patterns, based on the embedded element pattern, the array factor affected for rms random errors, which represents the errors induced in the calibration process, were utilized to estimate Z_{dr} and ICPR$_2$.

Considering that meteorological radar are meant to operate in the presence of rain, a model to predict the radar performance under rain conditions is then introduced. To validate this model, a numerical simulation in HFSS and experimental data obtained using radome samples under rain were compared. In addition, radar data obtained from the NEXRAD radar and CASA IP1 radar were compared.

6.2 CASA phased array radar predicted performance

The bias in differential reflectivity (Z_{dr}^b) and two way integrated cross-polarization ratio (ICPR$_2$) has been estimated for the CASA phased array antenna as a function predicted by array antenna patterns. A set of antenna patterns was calculated using

the measured embedded element pattern (32nd column) and the array factor for 64 elements, for each beam position from -50 ° to +50 ° in the azimuth plane. To obtain more realistic array patterns in the azimuth plane (similar to the measured patterns), Gaussian RMS random errors were introduced in the amplitude and phase excitation of each column array. The rms random errors that match the antenna measured patterns are aproximated 0.22 dB in amplitude and 1.66 ° in phase. Figure 6.1 illustrates the comparison of the azimuth patterns measured and predicted for $\theta_s=0$ ° and $\theta_s=45$ ° for both polarizations, respectively. In both cases the sidelobe roll-off of predicted patterns follow the measured values. A better match between predicted and measured patterns is obtained at broadside than at 45 °, and this can be attributed to mutual coupling and edge effects which are not accurately included when patterns are estimated by multiplying the center element and the array factor .

Figure 6.2 illustrates the bias in the differential reflectivity (Z_{dr}^b) and the standard deviation of the Z_{dr}^b for beam position in the azimuth plane (separated every 5 °). The bias in the differential reflectivity (Z_{dr}^b) represented by a dash blue line, varies from -2.6 dB to 4.34 dB, principally due to the effect of the difference in the gains of H and V (due to the ripples in the element patterns previously discussed). The standard deviation results from estimating 300 times the antenna patterns with Gaussian random values in order to represent the excitation with RMS values obtained from the measured antenna patterns ($\sigma_a=0.22$ dB and $\sigma_\phi=1.66$ °). The standard deviation of the Z_{dr}^b is represents the uncertainty conditions of the calibrated antenna which can affect the bias in Z_{dr} with maximum values at ±0.25 dB and average values of ±0.08 dB in the scanning range from -50 ° to 50 °.

Figure 6.3 illustrates the ICPR$_2$ of the array antenna based on the predicted antenna array patterns using the measured embedded element pattern. The results show that, for both polarizations, the ICPR$_2$ are better than -50 dB for the overall scanning range ($\pm$ 50°) and for both polarizations. ICPR$_2$ represents the integrated

118
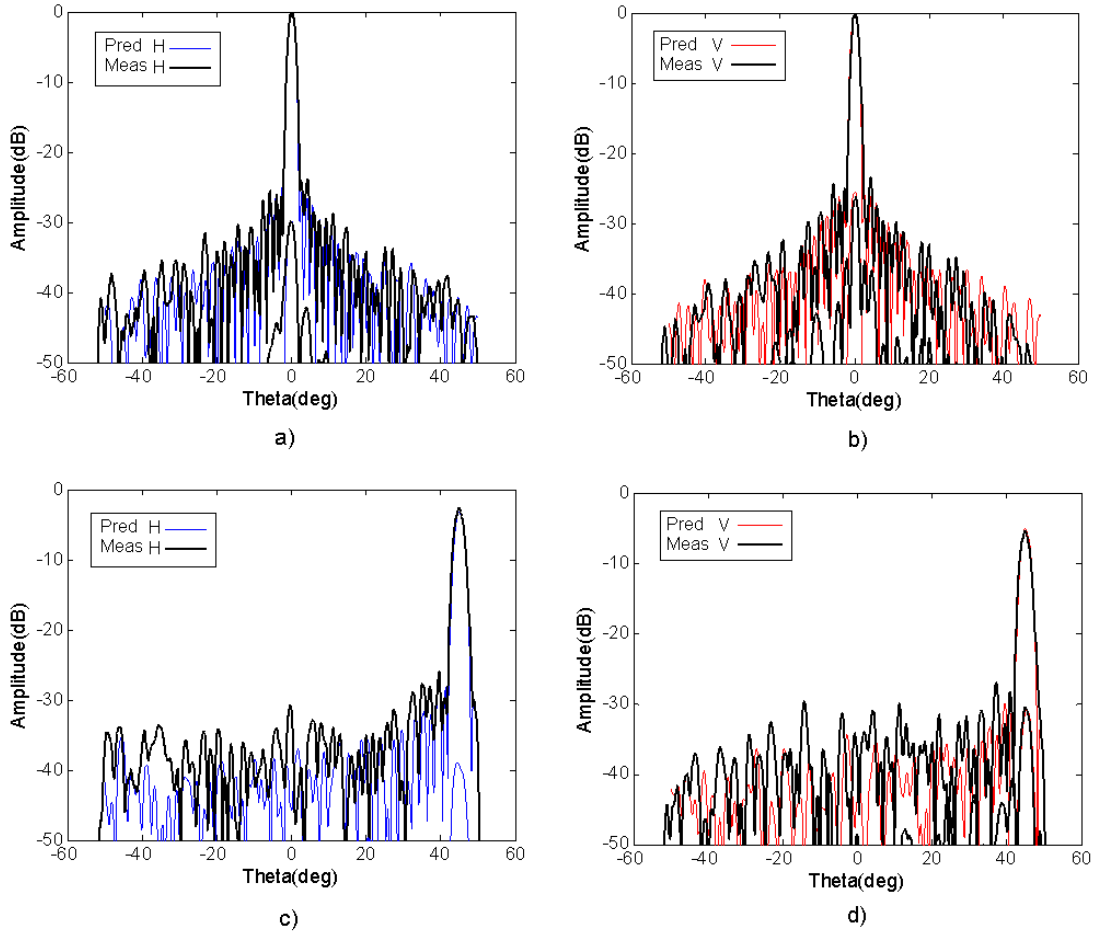
Figure 6.1. Predicted scanned patterns in azimuth plane using the embedded element pattern 32nd and rms Gaussian random errors σ_a= 0.22 dB and σ_ϕ= 1.66 ° a-b) Pattern for H and V polarizations at θ_s=0° and in c-d) Pattern for H and V polarizations at θ_s=45°
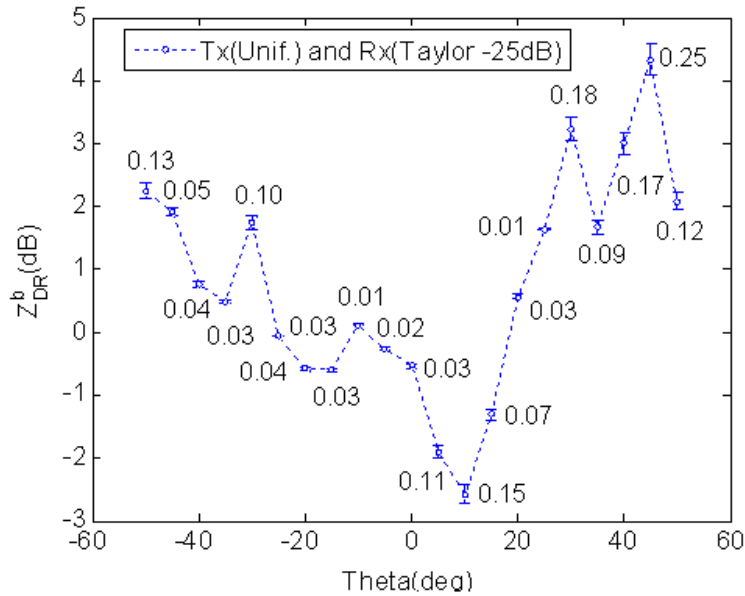
Figure 6.2. Estimated bias differential reflectivity (Z_{dr}^b) of CASA phased array radar based on predicted array antenna patterns in azimuth plane.

cross-polarization of the two-way patterns (transmission and reception). The one-way integrated cross-polarization is below -25 dB for the overall scanning range, which is better by 5 dB than the required values for a CASA radar in ATAR polarization radar mode.

6.3   Phased-tilt radar predicted in rain conditions

For meteorological radars, the electromagnetic characteristics of the radome is one of key factors in the overall performance of the radar since weather radar are meant to operate in the presence of rain. Dual polarized radars typically require high polarization isolation (higher than -20 dB) and a high degree of matched beam patterns (less than 5% integrated power over the main beam for H and V) to accurately estimate rainfall rate. When a radar is operating under rain conditions, the amount of water accumulated over the antenna radome may or may not affect the radar performance.
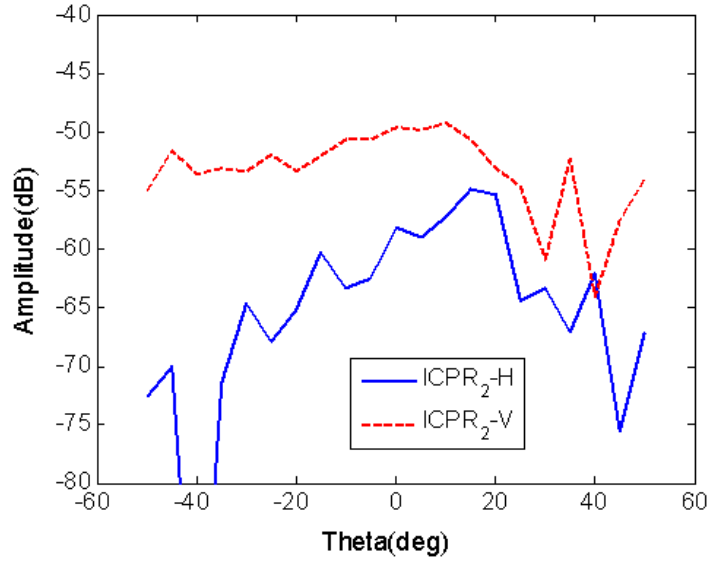
Figure 6.3. Estimated two-way integrated cross polarization ratio (ICPR$_2$) versus scan angle for CASA phased array radar based on predicted array antenna patterns in azimuth plane.

At higher frequencies, for example at 10 GHz, the dielectric constant or water is ε_r=56+37j (for 10°C). Depending of the amount of water on the radome surface, the radar signals can be attenuated, reflected, and also depolarized. The effect of water accumulation on radome surfaces has been extensively studied in terms of additional attenuation and depolarization effects in RF communication systems [21], [22], [67] and [23] and meteorological radar systems [15], [58]. Because it is difficult to accurately model the electromagnetic effects of water accumulated on radome surfaces, evaluation of radome performance has involved experimental measurements and computer simulations. Early models estimate the distribution of rain based on laminar flow and surface tension for the radome. This method does not include hydrophobic surface properties [21],[23]. Currently most antenna radomes for meteorological applications include hydrophobic skin materials to mitigate the negative impact of rain on radome performance. To evaluate and characterize the radome performance under

the influence of rain, experimental measurements were the most trustworthy method. Although the experimental method can provide a better understanding of physical phenomena, it requires (in addition to the radome), expensive RF equipment (disdrometeor, network analyzer, generator and calibrated antennas) and enough space to create artificial rain and deploy the experiment. An example of an experimental estimation of the attenuation by a wet X-band radome is presented by Bechini at [24]. In this study Bechini demonstrates how a large two-way attenuation (~12 dB - 14 dB) can occur under artificial rain of 156 mmh^{-1} over the cylindrical radome surface.

The method proposed in this section is a simple, inexpensive and effective way to evaluate any wet radome. The radome can be spherical, cylindrical or flat, and the internal structure can be composed of a small number of layers and different materials, including hydrophobic and super-hydrophobic surfaces. To validate this model a numerical simulation in HFSS and experimental data obtained in radome samples under rain were compared. In addition, radar data obtained by the NEXRAD radar and the CASA IP1 radar were compared.

6.3.1   Wet radome model

For a given rainfall intensity, the amount and type (droplets, rivulets and water film) of water accumulated on a radome surface are influenced principally by the shape, size and skin material used in the radome. Spherical shapes offer less surface area than semi-spherical-cylindrical radomes. Flat radomes provide much less surface and less water accumulation on the surface compared to other shapes. As an example, semi-spherical-cylindrical radome surface of the CASA IP1 radar system, represents 25 times the surface required for a in flat antenna with the same beamwidth.

The decades old method of applying a hydrophobic coating to the outer radome layer is still the most effective way to prevent rivulets and thin films of water from

accumulating on the radome. A hydrophobic coating or water repellent separates the continuous film of water or rivulets into separate beads. Figure 6.5 c) illustrates an example of two common materials used on radome surfaces. On the right, a sample of Fiber Glass (non-hydrophobic) illustrate the formation of undesirable water film and permanent rivulets on the radome. On the left, a sample of Teflon (hydrophobic) naturally repeals water film and rivulet formation on the radome surface.

6.3.1.1 Water film model

A radome surface untreated for repelling water can lead to catastrophic consequences for a radar or communication system. It has been demonstrated in the past that water sheeting over the radome can seriously reduce the effectiveness and coverage of a radar system by attenuating a signal drastically, almost to the point of extinction [22], [15]. The relationship between rain intensity and the thickness of a water film formed over the radome without repellent treatment has been mathematically modeled in the past. The thickness of the mass flow of fluid moving along a semi spherical radome can be estimated using the Gibble's equation 6.1, presented in [21].

$$t_s = \sqrt[3]{\frac{3\mu Ga}{2\rho g}} \tag{6.1}$$

where G represents the volumetric flow rate or rain rate in ms^{-1}, running on the radome surface, u is the kinematic viscosity of the water in kgm^{-1}s^{-1}, ρ is the density of the water in kg.m^{-3}, g is the gravitational acceleration in ms^{-2}, and a is the radius of the radome sphere in m.

A flat inclined surface can be modeled using expression 6.2 used by [69] to characterize a laminar flow down an inclined surface. The width of the surface is represented by W in m, and θ_t represents the angle of inclination of the radome surface.

$$t_f = \sqrt[3]{\frac{3\mu G}{W \rho g \sin(\theta_t)}} \qquad (6.2)$$

Figure 6.4 a) illustrates an example of two types of radomes (spherical and flat) at 10 GHz affected by a accumulation of water over their surfaces. The spherical radome has a diameter of 2.7 m to protect a dish antenna that provides an antenna beamwidth of 2 °x 2 °. The flat radome protects an flat PAR antenna of area 1m x 1m that also provides an antenna beamwidth of 2 °x 2 °. A uniform film of water has a calculated thickness based on the expression in 6.1 for a semi-spherical radome and 6.2 for a tilted flat radome. Knowing the thickness of the water film and the dielectric constant, one additional layer was added at the front of the dry radome model presented in section 4.3.4.2. Figure 6.4 b) shows the one-way attenuation versus rain rate for the flat radome for different tilt angles. As expected, the larger surface area of the semi-spherical radome tends to accumulate more water, and consequently more attenuation is obtained with respect to the tilted plane radome.

6.3.1.2 Droplet model

The model for droplet formation on a radome surface is subdivided into four parts, as illustrated in Figure 6.5. The first part estimates the drop size distribution (DSD) of a rain event. In this approach, the DSD is assumed to follow a Gamma distribution. Drop spectra $n(D)$ are calculated as follows:

$$n(D) = N_o D^u \exp(-\Lambda D) \quad (0 < D < D_{\text{max}}) \qquad (6.3)$$

where D represents the drop diameter, and u, Λ, N_o are model fit parameters defined in [70], [20]. Based on this rain-rate dependent DSD, the second part of the model estimates the distribution of liquid water droplet sizes $n_R(D)$ over the flat tilted radome surface area (A_u):
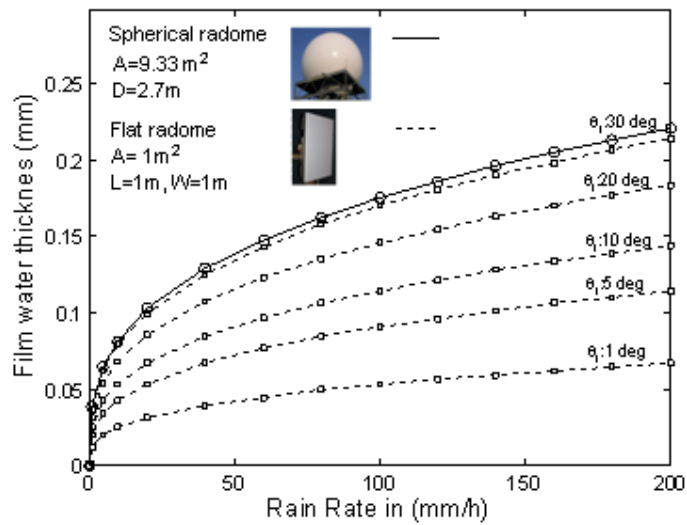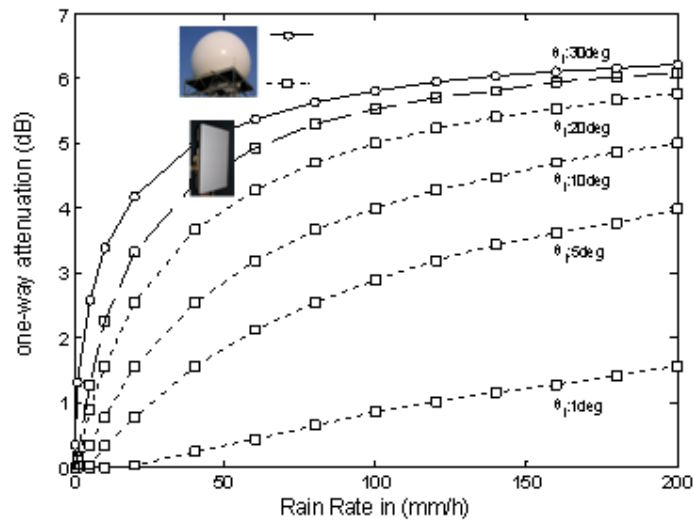
Figure 6.4. Comparison of thickness of the water film and the rain-induced attenuation on a spherical radome versus on a planar array, both non-hydrophobic surfaces, at X-band.

$$n_R(D) = \frac{n(D)}{v(D)A_u \cos(\theta_t)T\Delta D} x 10^6 \quad (0 < D < D_{s-\max}) \tag{6.4}$$

where $v(D)$ is the terminal velocity of the water droplet in air, ΔD is the bin-width of each drop-size class, T represent the integration time, and θ_t the inclination angle of the radome surface [20]

To achieve the DSD modeled in 6.3, a random number generator is used to create a distribution of droplets. To estimate the DSD in a tilted radome surface using 6.4, properties of the radome skin, such as surface tension and contact angle hysteresis, are required to include the drop dynamics and rivulet formation. In a hydrophobic material, the rivulet formation does not occur always at the same place. The origin of each rivulet starts when gravitational force defeats the surface tension of a droplet on the radome surface. The inclination angle and the number and size of droplets defines the number of rivulets on a given surface. A mathematical expression that helps to understand the origin of the rivulets and also permits the characterization of the DSD for an inclined surface is detailed in equation 6.5, given by Nilsson [71]. This expression represents the critical angle, which is the angle where the gravity force defeats the surface tension of the droplet in a given tilted surface.

$$\alpha_{crit} = \sin^{-1}\left(\frac{6k^{-2}\sin\left(\pi - \frac{1}{2}\sin\theta_H\right)(\cos\theta_R - \cos\theta_A)}{D^2}\right) \tag{6.5}$$

where θ_R is the receding angle and θ_A is the advancing angle. The hysteresis angle is then represented by $\theta_H = \theta_R - \theta_A$, and k^{-1} is the capillarity length, which is 2.7 mm for water.

Figure 6.6 a) illustrates the critical angle versus drop diameter for different hydrophobic (Teflon and GoreTex) and super-hydrophobic (TeflonS240, Hirec100 and Cytonix WX2100) material surfaces. Figures 6.6 c-d-e) illustrate the advancing, receding and hysteresis angles of 6 samples obtained based on the drop expansion and
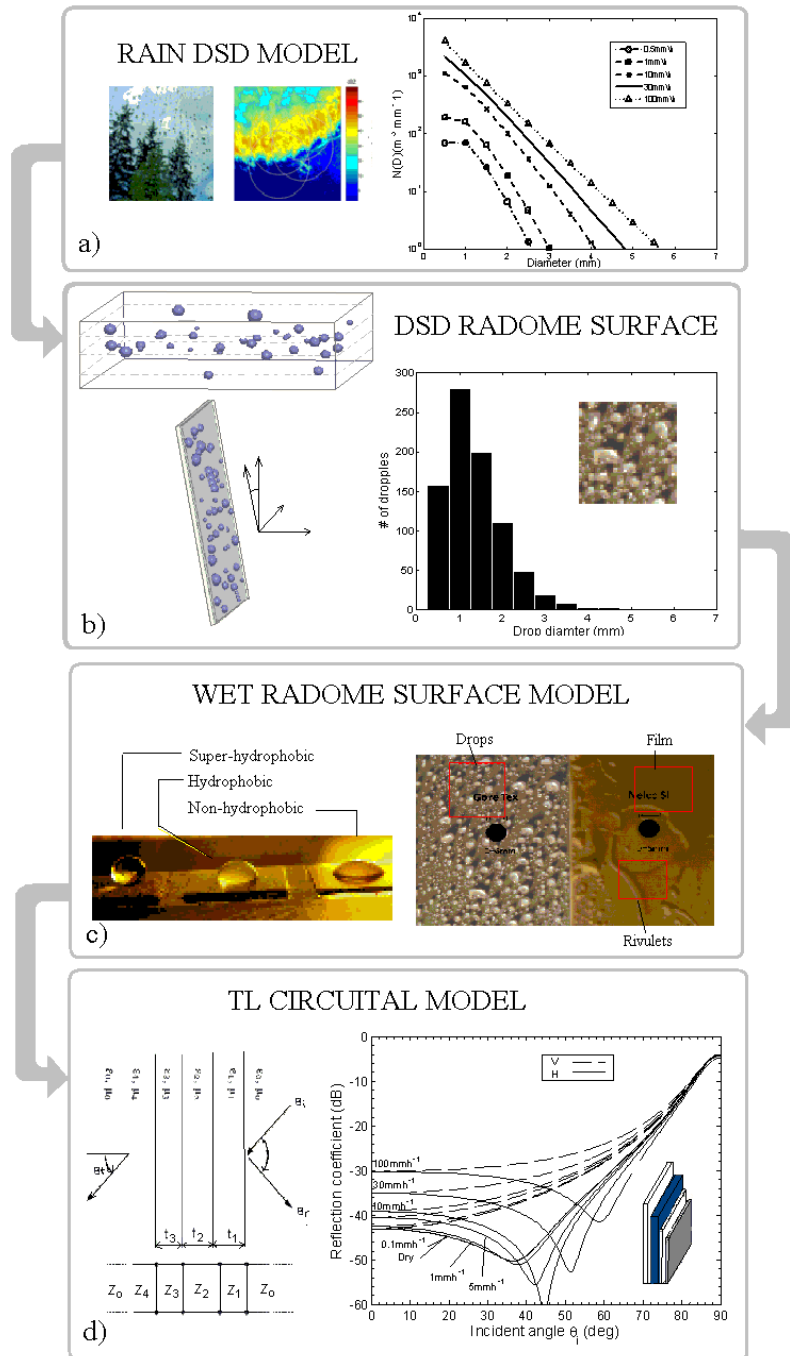
Figure 6.5. Representation of wet radome model a) Rainfall rate and rain DSD model is used to estimate the number of droplets as a function of drop diameter. b) Drop side distribution model on radome surface. c) Droplets, rivulets and film water formation model. d) A transmission line circuit model is used to estimate the scattering performance of the wet radome surface and results.

contraction process in the Fluid Dynamic Laboratory at University of Massachusetts, Amherst [71]. From 6.5, the maximum diameter of a droplet for a given tilt angle (critical angle) (D_{s-max}) was used to adjust the estimated DSD. Details of the advanced (θ_A), receding (θ_R) and hysteresis angle (θ_H) are presented in Table C.2.

Once the drop spectra on the radome surface has been calculated, the next step is to estimate the effective dielectric constant of the wet surface. In the case of drop formation, since the droplets are small compared to wavelength, the Maxwell-Garnet mixing formula in 6.6 is used [73], as follows:

$$\varepsilon_{eff} = \varepsilon_2 + \frac{3f\varepsilon_2(\varepsilon_1 - \varepsilon_2)}{\varepsilon_1 + 2\varepsilon_2 - f(\varepsilon_1 - \varepsilon_2)}10^6 \tag{6.6}$$

where, f is the fractional volume of formed water droplets with dielectric constant (ε_1) over the radome surface with dielectric constant (ε_2).

The fourth and last part of the model consists of estimating the scattering parameters of a flat radome for any angle of incidence (in the azimuth plane) and polarization mode (vertical and horizontal). This model was formulated using the equivalent transmission line method discussed in section 4.3.4 of Chapter 4.

6.3.2 Results and validation

Three samples of Fiber Glass (non-hydrophobic) and GoreTex (hydrophobic) were exposed to moderate rain on September 21-24, 2011. Each sample had a surface area of 9 cm x 9 cm, was tilted -10 °, 0 ° and 10 °, respectively, and then left for an interval of four and a half hours during which rain fluctuated from 0.1 mmh^{-1} to 45 mmh^{-1}. Photographs with a digital high resolution camera were taken at intervals of 30 minutes. The average reflectivity data were obtained from the two near S-band radars in Boston, MA and Albany, NY. Figure 6.7 a) illustrates the average radar reflectivity and the rainfall rate estimated using the expression Z-R, defined in the
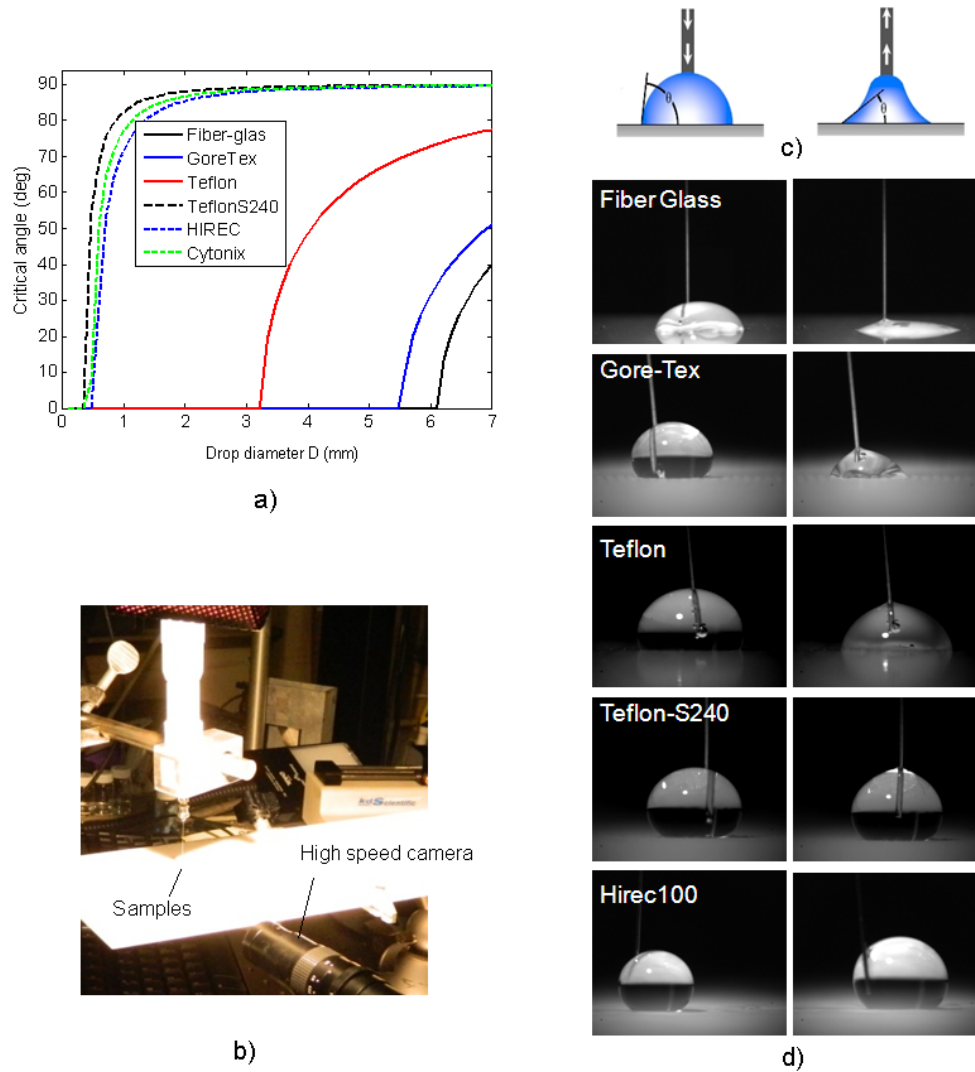
Figure 6.6. Method to characterize the advancing (left) and receding (right) contact angles for Non-hydrophobic (Fiber glass), Hydrophobic (GoreTex, Teflon) and Super-Hydrophobic (Teflon-S240B and Hirec100). Critical angle versus drop diameter for non hydrophobic (Fiber Glass), hydrophobic(GoreTex and Teflon) and Super-hydrophobic (Hirec,Teflon-S240 and Cytonix).

following equation 6.7. where Z is the reflectivity in non-logarithmic units, and R is the rain rate in millimeters per hour.

$$Z = 250R^{1.2} \tag{6.7}$$

Figure 6.7 c) shows pictures of the water accumulated on three Goretex radome samples tilted at -10°, 0° and 10°, exposed for 2 hours and 51 minutes under the same rain event (on September 23, 2011). The droplets were counted and measured manually, and then represented in the histogram plots for each tilt angle (after 2 hours and 51 minutes). As expected, the samples at large tilted angles show more droplets accumulated.

Using the rain rate estimated from the reflectivity of S-band (NEXRAD) radar using the Z-R relationship given in 6.7 and the radome hydrophobicity properties (hysteresis angle), the drop size distribution was calculated using the expressions 6.3 and 6.4. Figure 6.8 illustrates the comparison results of the drop size distribution on the Goretex sample tilted at 10°. Although the estimated and measured distributions do not match perfectly, the median values of the drop diameter differ only by 0.01 mm.

The fourth and last part of the model estimates the scattering parameters of a flat radome for any angle of incidence (in the azimuth plane) and polarization mode (vertical and horizontal). This model was formulated using the equivalent transmission line method, represented in Figure 6.5 d) and discussed in the section 4.3.2.

6.3.2.1 Measured wet radome radar data

We used the case in which radar data from X and S-band radars were used to estimate radome attenuation of the IP1 CASA X-band radars under rain condition [15]. Reflectivity data for a precipitation event (June 20, 2007) were observed by
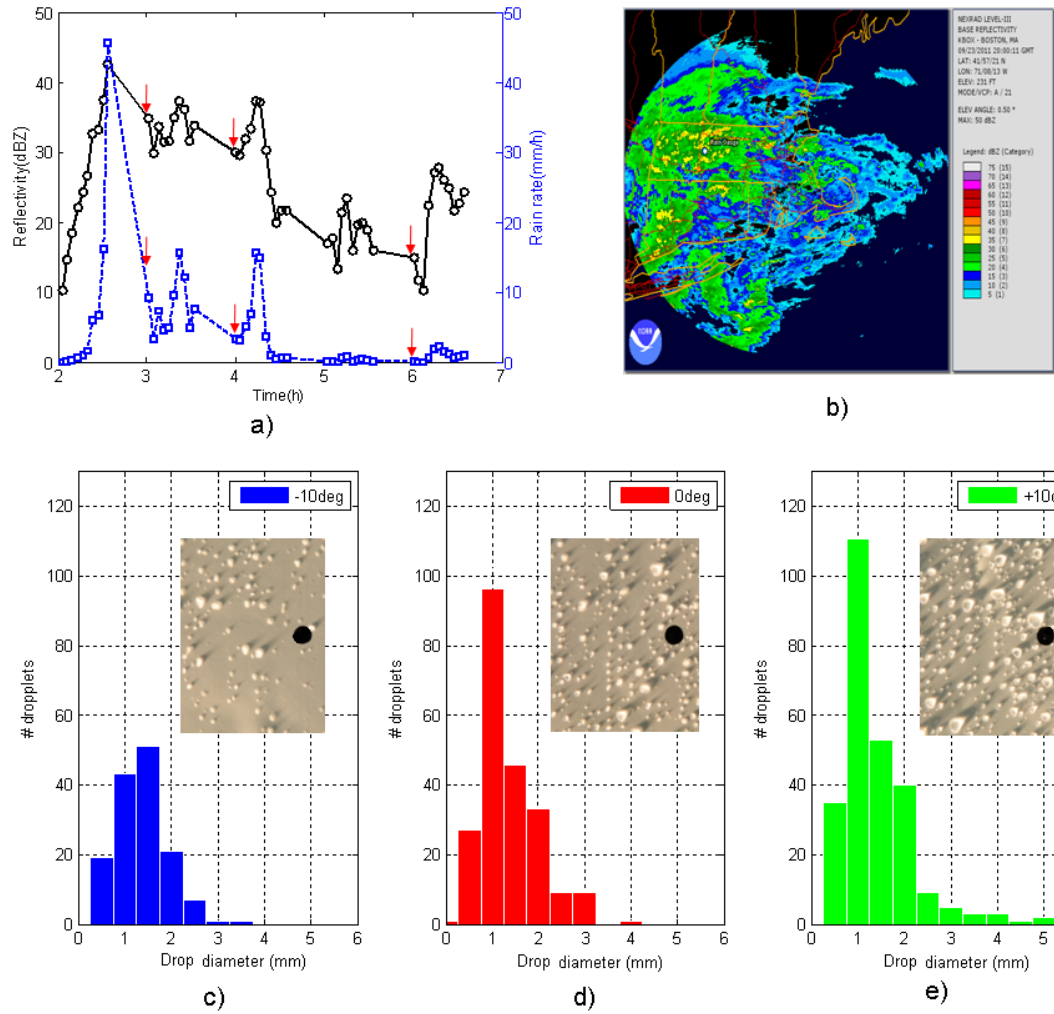
Figure 6.7. DSD on radome surface based on rainfall rate DSD. a) Reflectivity and rain rate obtained from rain experiment IV (Sept. 23th. 2011). b) Reflectivity data from XBOX NEXRAD radar at Boston. c) Picture and DSD of water droplets accumulated in a Goretex surface tilted -10°. d) Picture and DSD of sample of water droplets accumulated in a Goretex surface tilted 0° and e) Picture and DSD of water droplets accumulated in a Goretex surface tilted +10°
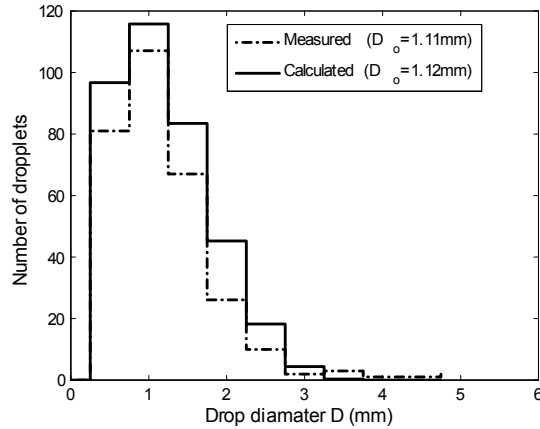
Figure 6.8. Comparison of estimated and measured drop size distribution collected on a hydrophobic (Goretex) radome sample (5cm x 5cm). The measured data corresponds with data obtained in experiment IV of September 23, 2011.

CASA IP1 radar (KRSP) and the WSR-88D (KRTLX). The convective line event seen by S-band KTLX radar came from the Northwest passed through the CASA radar network area (Figure 6.9 a). Data were collected by the four CASA X-band radars and the KTLX S-band radar. The storm extended over more than 140 km in length and 40 km in width, resulting in severe attenuation on three (KCYR, KRSP and KSAO) of the four CASA radars, simultaneously.

Figure 6.9 c) shows a comparison of the reflectivity between the CASA KRSP X-band and the KTLX S-band radars averaged over an area of 750 km². A short period of severe radome attenuation is clearly identified during the half hour ranging from 6 to 6.5 UTC, with a maximum observed attenuation of 7.5 dBZ. The reflectivity estimated over the X-band radar wet radome by the S-band radar is also shown in Figure 6.9 d).

The radome of the IP1 radar systems is a hemisphere-on-cylinder radome design with a diameter of 8 ft, and designed to operate from 9 GHz to 10 GHz. The wall construction (A-sandwich radome) consists of two Epoxy/Fiberglass skin layers and

a Honeycomb core as an inner layer. A thin layer of CRC 6000 hydrophobic coating (with a contact angle of 140°) was applied to prevent the formation of film water.

Figure 6.9 d) shows the corresponding calculated and measured values of the two-way attenuation radar signals for a reflectivity range between 0 dBZ to 50 dBZ. The scatter data was obtained by comparing the difference between the S- and X-band wet radome. Area was averaged over the rain gauge network location with a size of 20 km by 32 km. The calculated data (dashed line) was estimated using the radome characteristics and geometry for a rain intensity equivalent to a reflectivity between 0 dBZ to 50 dBZ, in intervals of 5 minutes. A good fit existed between measured and calculated values, which suggests that the model proposed can be used to estimate the two-way losses of a wet radome surface.

Table 6.1 provides information comparing radome design specification (given by the manufacturer) and calculated values based on the model proposed. It also shows comparison with radar data measured by Trabal [15] in dry condition, and also for 10 mmh^{-1} and 30 mmh^{-1} rainfall conditions. Small differences existed between specified and estimated values of two way losses using this model for dry and wet conditions.

Table 6.1. Summary results of two-way attenuation in a X-band IP1 antenna dish radome.

Parameter	Specified	Calculated	Measured [15]
Two-way loss (dry)	0.8 dB	0.50 dB	No data
Two-way loss (at 10mmh^{-1})	1.6 dB	1.18 dB	1.11 dB
Two-way loss (at 30mmh^{-1})	2.0 dB	1.82 dB	1.96 dB

6.3.3 Case of study

In this section, three different scenarios were selected to illustrate the utility of the wet radome model proposed. The first case represents a situation where a flat antenna radome designed without a hydrophobic surface is tilted about 34°. The second case
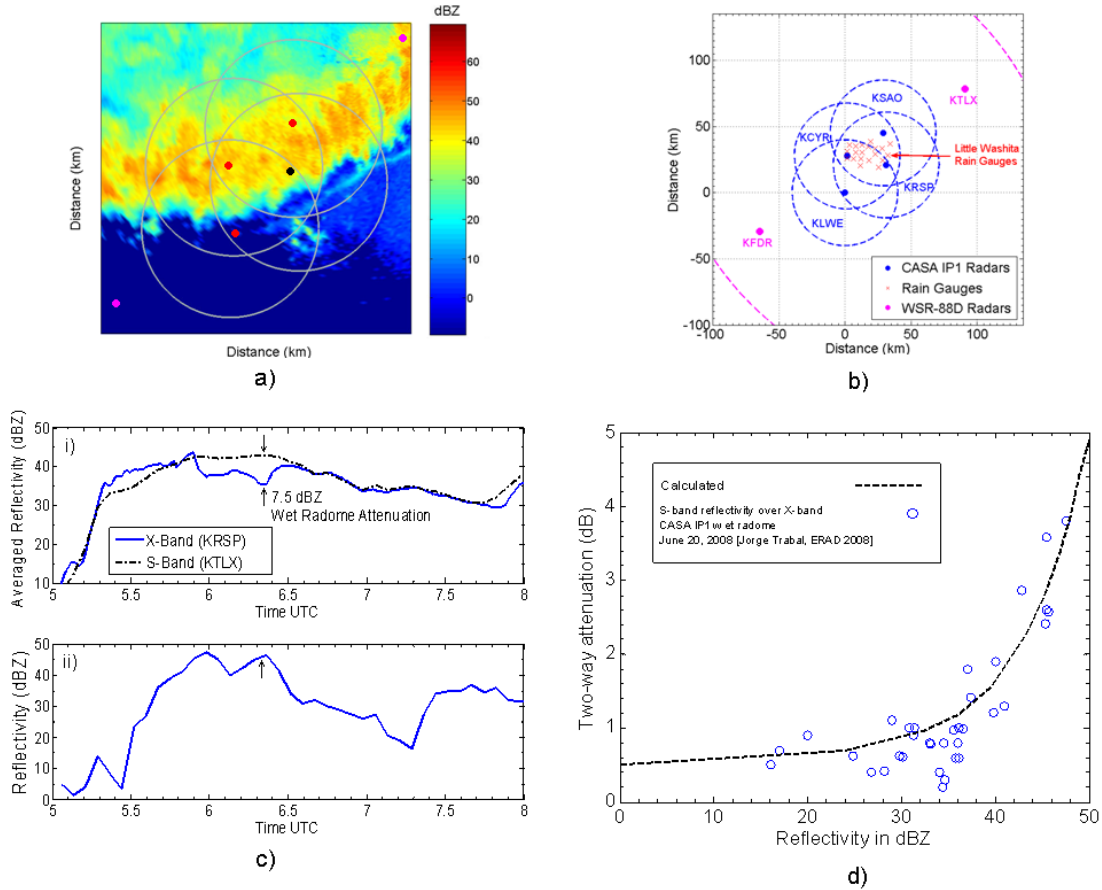
Figure 6.9. Validation results of wet radome model for IP1 X-band radome. a) Storm event (June 20th 2007) in Oklahoma. b) Representation of relative locations of IP1 radar network nodes, NEXRAD radars and rain gauges network. c) Averaged reflectivity for the X- and S-band radars during the storm event (i), and S-band reflectivity over the X-band wet radome during the same time and day (ii) The reflectivity over the X-band radar wet radome by the S-band radar d) calculated and measured values of the two-way attenuation radar signals for reflectivity range between 0 dBZ to 50 dBZ.

also represents a flat antenna radome, but this time designed with the hydrophobic film, also tilted about 34°. A third case uses the same radome, however, the tilted angle is reduced from 34° to 10°. For all three cases, the flat radome considered was designed to operate at 10 GHz, and the radome corresponded to a walled structure composed of one thin layer (12 mil) of Teflon (ε_r=1.55, tanδ= 0.0017) and a thick layer (250 mil) of core foam Rohacell 31HF (ε_r=1.55, tanδ= 0.0017). We assume for these cases a water dielectric constant of ε_r= 60.68+32.79i and tangent loss of tanδ =0.54, estimated for 10 GHz and at 20° C.

6.3.3.1 Flat radome tilted 34° without hydrophobic surface.

Most designs of the antenna radomes for weather applications include a water-repellent surface (hydrophobic and super hydrophobic films) to prevent water film formation or rivulets. This is an effective and inexpensive solution to reduce attenuation, reflection and depolarization of the radar signals. However, one of the biggest concerns with such water-repellent surfaces is their lifetime and their performance degradation over time when exposed to temperature, humidity, ultraviolet rays, air pollution and dust. Weigand at [25] evaluated the contact angle of several radome hydrophobic samples used for an airport surveillance radar. The study shows that weather and pollution reduce the contact angle up to 30° in an interval of time between 3 to 9 months. In 2009, a report by the Support Center for Advanced Telecommunications Technology, [58], presented results of hydrophobic durability performed in a short term (1168 hours in accelerated weathering system) and long term (24 months in real environment) studies. Significant degradation of the contact angle (from 151° to 132°) was found in the short term, and degradation of the contact angle (from 151° to 100°) was found 6 months after the long term experiment had started.

Figure 6.10 presents one-way attenuation, reflections, and depolarization for a flat radome with tilt angle θ_t=34° as a function of rain rate and scan angle in the azimuth

plane. Figure 6.10 a) shows the one-way attenuation, which indicates a significant attenuation (1.6 dB to 4.5 dB) can be produced for moderate and high rain intensities (10 mmh^{-1} to 100 mmh^{-1}). Small variation (less than 0.01 dB) between H and V is observed in the near to broadside, however it increases up to 0.5 dB at a 45° incident angle. Figure 6.10 b) shows the reflection coefficients of the radome. Results shows significant changes in reflection for H and V for a wet radome as compared to dry radome, even for small rain intensities. Reflections can be a concern for values higher than -10 dB, since those can considerably affect the scanning impedance of the array antenna and also the antenna patterns principally in the sidelobe region. Figure 6.10 c) presents the cross-polarization ratio of the radome. At broadside, negligible depolarization is produced. However when the antenna is scanned, the wet radome significantly affects the polarization of the radar signal. At 45° scanning in the azimuth plane, we observe that the radome can degrade cross-polarization by about 20 dB.

6.3.3.2   Flat radome tilted 34° with hydrophobic surface.

In this case we replaced the skin surface with a hydrophobic material (Goretex) since this material (Teflon based) is commonly used for weather radome radars. Figure 6.11 illustrates the one-way attenuation, reflections, and depolarization for a flat radome with tilt angle θ_t=34° as a function of rain rate and scan angle in the azimuth plane. Figure 6.11 a) shows a comparison between the total reflections when the radome is dry and when the radome is wet for different rain intensities. The results indicate that the attenuation is drastically reduced compared to the previous case (non- hydrophobic surface), by about 2.9 dB when exposed to 100 mmh^{-1}. As with the previous case, small differences in attenuation existed between H and V with respect to beam position.
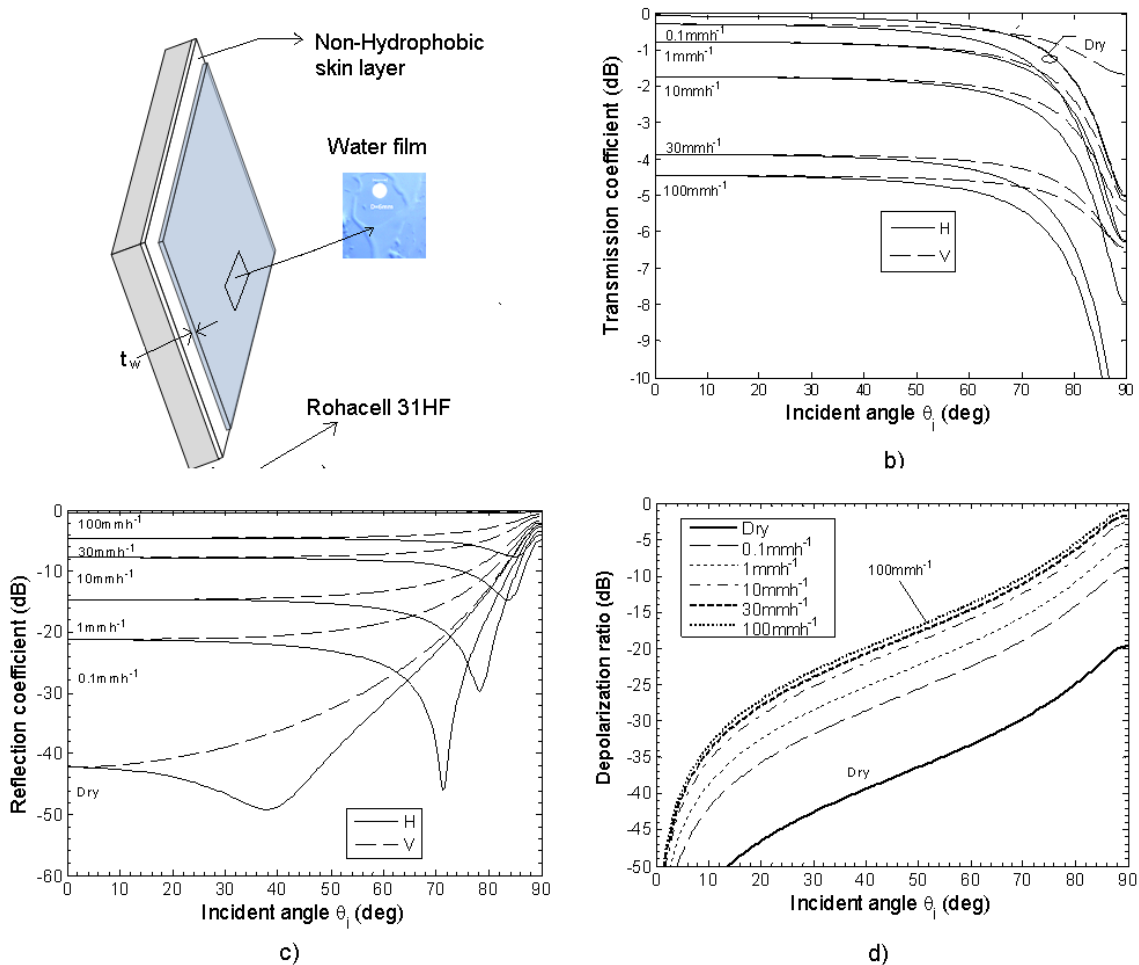
Figure 6.10. Calculated results of non hydrophobic wet radome surface tilted (34 $^\circ$) under different rain intensity (0.1 mmh^{-1}, 1 mmh^{-1}, 5 mmh^{-1}, 10 mmh^{-1}, 30 mmh^{-1} and 100 mmh^{-1}). a) Transmission coefficient versus incident angle b) Reflection coefficient versus incident angle, and c) Depolarization ratio versus incident angle

Figure 6.11 b) shows reflections. In the worst case scenario, for 100 mmh^{-1}, the reflections are below -25 dB for the overall scanning range required ($\pm 45°$). Figure 6.11 c) shows the cross-polarization ratio of this radome. For 45°, the cross-polarization induced by the radome is about 14 dB (16 dB better that in the previous case).
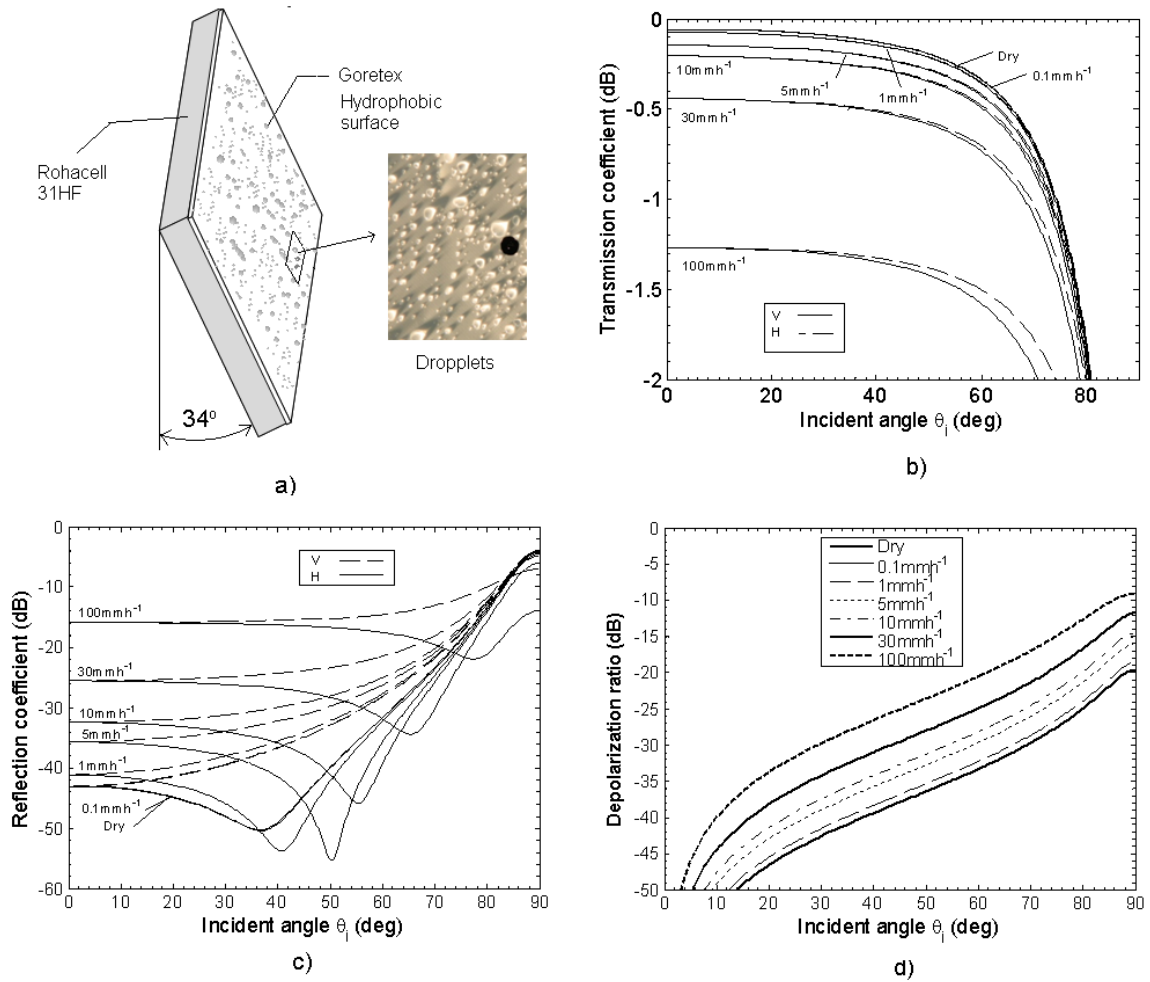
Figure 6.11. Calculated results of hydrophobic (Goretex) wet radome surface tilted (34 °) under different rain intensity (0.1 mmh^{-1}, 1 mmh^{-1}, 5 mmh^{-1}, 10 mmh^{-1}, 30 mmh^{-1} and 100 mmh^{-1}). a) Transmission coefficient versus incident angle b) Reflection coefficient versus incident angle, and c) Depolarization ratio versus incident angle

6.3.3.3 Flat radome tilted 10° with hydrophobic surface

In this case we used the same radome as in the previous case, but reduced the tilt angle from 34° to 10°. Figure 6.12 illustrates the one-way attenuation, reflections, and depolarization for a flat radome tilted $\theta_t{=}10°$ as a function of rain rate and scan angle in the azimuth plane. Figure 6.12 a) compares the transmission coefficient of a dry radome with a wet one for different rain intensities. The results indicate a significant improvement can be obtained in the three parameters under evaluation by reducing the tilt angle of the antenna. For 100 mmh^{-1} at broadside, the improvement for a hydrophobic radome tilted at 34° is about 1.35 dB, and the improvement can be 4 dB for a radome without hydrophobic skin. Figure 6.12 b) shows that in the worst case scenario, for 100 mmh^{-1} the reflections are below -35 dB for the overall scanning range required (±45°). Figure 6.12 c) shows that the cross-polarization ratio of this radome tilted at 10° only degrade the radar signals 8 dB, or 6 dB better that the previous case and 12 dB better when compared to the radome without the hydrophobic skin surface

6.3.3.4 An special case when rivulets are presented.

Modeling the rivulet formation in an inclined surface requires a sound understanding of the dynamics of droplets for a particular surface. Upon simple inspection, non hydrophobic materials tend to spread water on a surface, creating uniform films of water that end in permanent rivulets, as is illustrated in Figure 6.13 a). In a hydrophobic material, the rivulet formation does not occur at the same place. The origin of each rivulet starts when gravitational forces defeat the surface tension of a droplet on the radome surface. The inclination angle, number, and size of droplets define the number of rivulets for a given surface. The mathematical expression that helps to understand the origin of the rivulets and also permits the characterization of the drop size distribution for a inclined surface is detailed in equation 6.5, and can
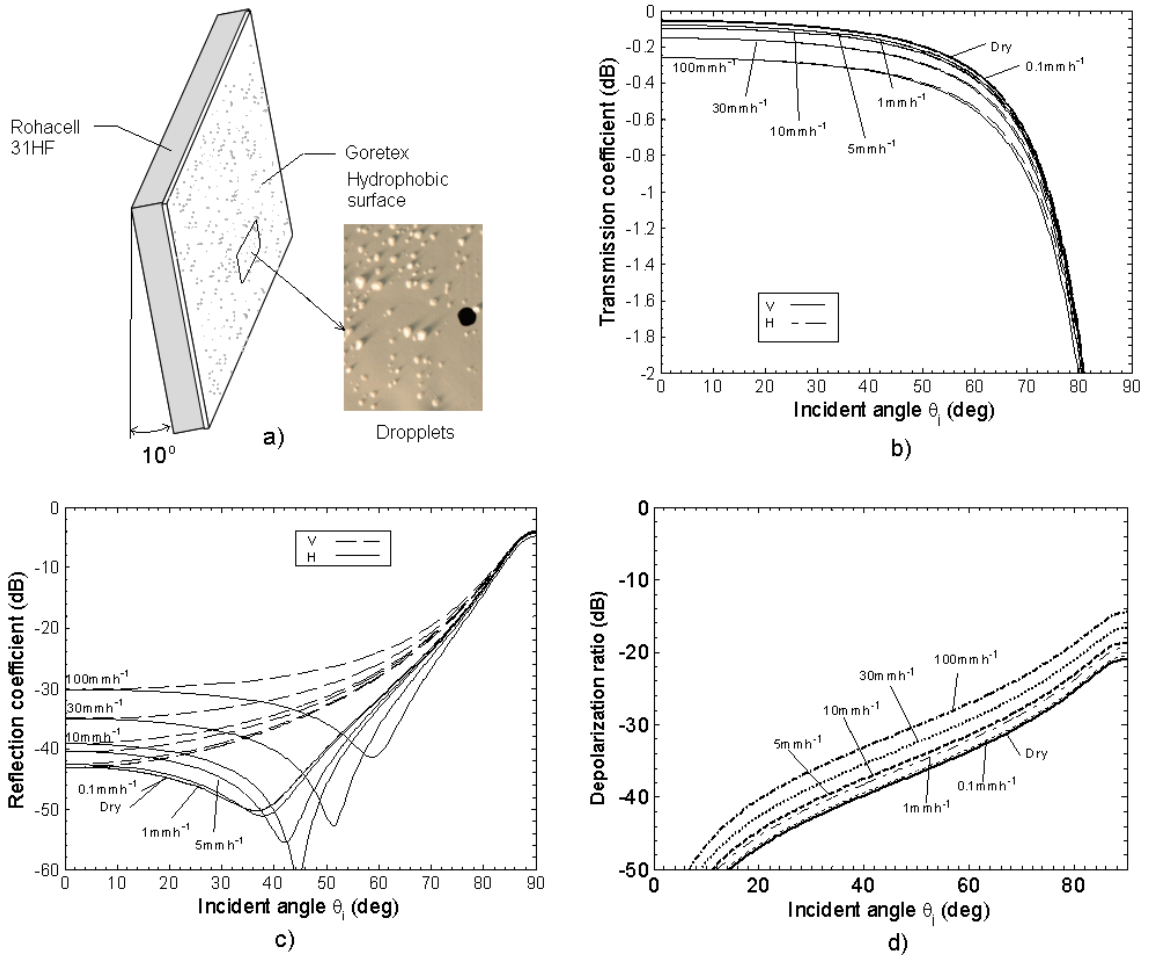
Figure 6.12. Calculated results of hydrophobic (Goretex) wet radome surface tilted (10 °) under different rain intensity (0.1 mmh^{-1}, 1 mmh^{-1}, 5 mmh^{-1}, 10 mmh^{-1}, 30 mmh^{-1} and 100 mmh^{-1}). a) Transmission coefficient versus incident angle b) Reflection coefficient versus incident angle, and c) Depolarization ratio versus incident angle

be used to estimate the number of rivulets. However, it is quite difficult to introduce rivulets in the model proposed. Instead, a numerical model using the full-wave solver Ansys/Ansoft HFSS is used [60]. The HFSS model consists of a unit cell of 17 mm x 17 mm, where the droplets and rivulets were introduced as shown in Figure 6.13 b). Two models were considered; the first one represents the radome with droplets, and in the second one we add one rivulet in the unit cell. The results presented in Figure 6.13 c-d) show the transmission and reflection coefficients versus incident angle relation changes drastically for both polarizations, and changes with incident angle. These preliminary results are important considering that the differences between H and V (due the presence of rivulets in random fashion) can affect the performance of the radar system when it operates under rainy conditions. In addition, simulation results of the radome without the droplets were included in order to demonstrate the TL circuital model proposed.

6.4   Conclusion

Predicted antenna patterns of the full array were estimated using the measured embedded antenna element pattern and the array factor affected by RMS random errors, in accordance with measured antenna patterns. The patterns were used to estimate the bias in the differential reflectivity Z_{dr}^b and ICPR$_2$ produced by the antenna.

The bias differential reflectivity due to the antenna patterns varies from -2.6 dB to 4.34 dB, principally due to the effect of the difference in the gains of co-polar patterns in H and V due to the ripples in the element patterns. A maximum standard deviation of 0.25 dB was found at 45 ° scanning (in azimuth plane) as the result based on estimating the antenna patterns 300 times with Gaussian random number generator corresponding with the RMS obtained from the antenna measured antenna patterns.
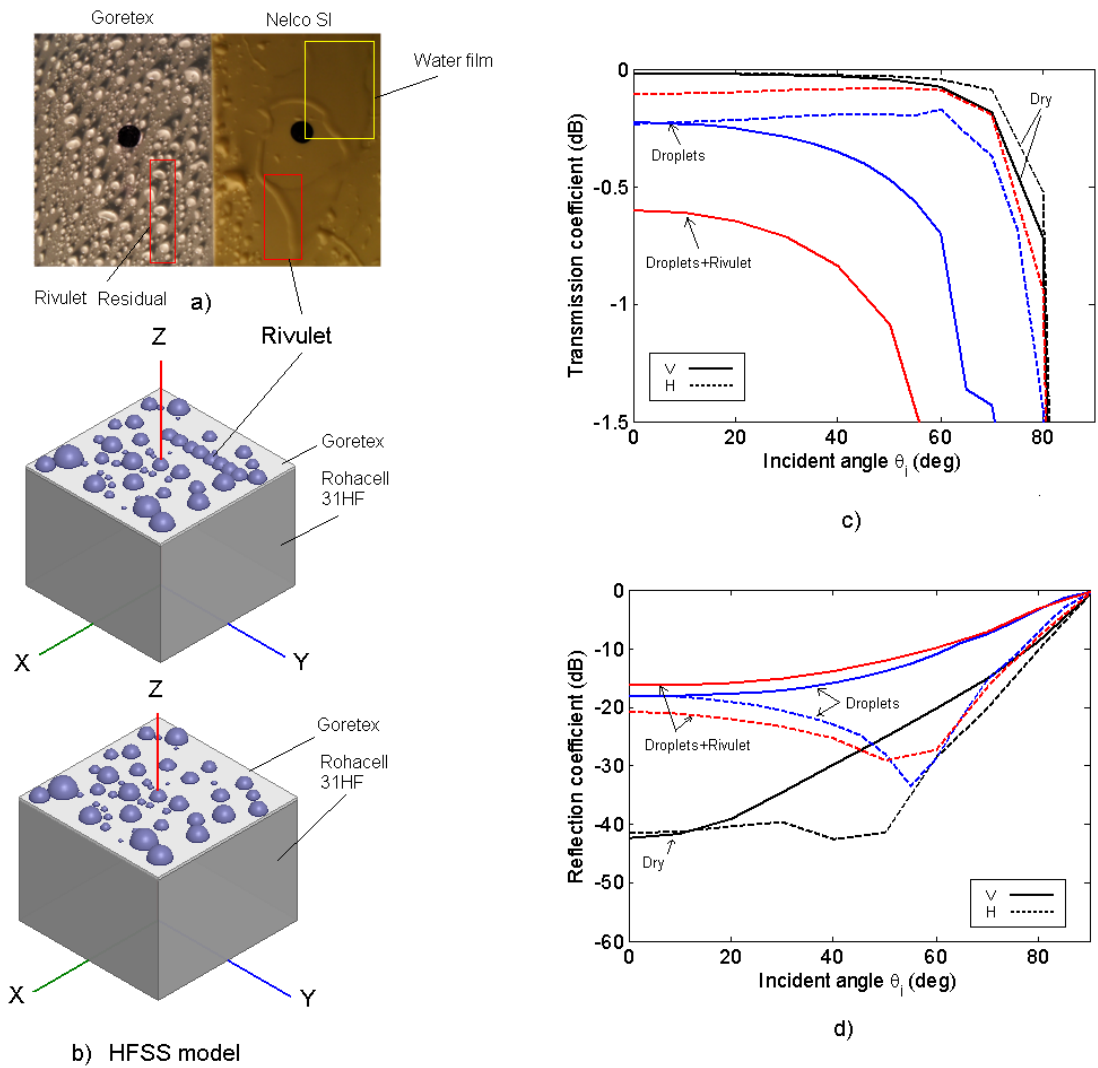
Figure 6.13. Numerical simulation results of wet radome surface (Hydrophobic) with and without the rivulets formation a) Picture of water formation in a radome surface b) HFSS model for wet radome with and without rivulet formation. c-d) Simulated results of transmission and reflection coefficients.

The estimated $ICPR_2$ (two-way patterns) for the overall scanning range ($\pm$ 50 °) is below -50 dB. A maximum mismatch beam pattern of 7.2 % was observed over the main beam.

Weather radar typically operate under rain conditions, and the effect of the water accumulated on the radome surface degrades the performance of the radar system, especially when the radar is polarimetric. Theoretical models consider only the water film to estimate the attenuation of wet radomes. The film model typically overestimate the attenuation of the radome since most of the weather radomes includes a thin hydrophobic coating. For a better estimation of wet radome attenuation, experimental procedures have been used. Experimental methods are expensive and the accuracy depends on the precision utilized to estimate the artificial rain rate. To overcome with these two problems, a new theoretical model to estimate the amount of water accumulated over a radome surface is proposed. The model was implemented and effectively applied to several scenarios (including semi-spherical, cylindrical, flat radomes with hydrophobic and super-hydrophobic skin surfaces). In addition to the attenuation, the model estimates the reflections and depolarization. The results have been validated with numerical simulation in HFSS and experimental data and were found be very satisfactory.

Use of hydrophobic surfaces is the most successful approach to minimize the water accumulation on radomes and prevent the associated high attenuation, depolarization, and reflection. Unfortunately, hydrophobic surfaces are delicate surfaces that can easily loose the hydrophobic properties due to touch, dirt, pollution, rain, erosion, and/or UV rays. The most durable hydrophobic surfaces retain with acceptable hysteresis angles for 3-9 months. After that, the hydrophobicity agent or surface needs to be replaced or repainted.

Flat tilted radome surface have the ability to minimize the water accumulation with the tilting angle. For example, reducing the tilting angle of a flat radome (based

on Rohacell and Goretex) from 34 ° and 10 °, the results indicate a significant improvement in the radome performance. For a rainfall rate of 100 mmh^{-1}, an incident angle of 45 ° (in azimuth), the radome tilted at 34 ° (in elevation), the wet radome presents an attenuation of -1.3 dB (one-way), reflections of -17 dB and depolarization ratio of -25 dB. However, when the same radome is tilted only 10 °(in elevation), the attenuation is reduced to -0.38 dB (one-way), the reflections reduced to -28 dB and depolarization ratio is reduced to -31 dB.

A preliminary analysis of rivulet formation has also been discussed in this chapter. Rivulet formation on a hydrophobic surface starts when the gravity force is larger than the surface tension of a large drop on the radome. When this happens, the drop runs and create a vertical pattern with small droplets. Expression 6.5 can be used to estimate the number of rivulets on an flat tilted radome surface. The positions of the rivulets are random and the rivulets also depend on the tilt angle, surface material, and rainfall rate. Since rivulets presents a vertical pattern, rivulets affect the vertical polarization more than the horizontal polarization. This can be a problem for a polarimetric radar since larger errors can be produced in the channel V but not necessarily in channel H. To demonstrate the effect of rivulets, a wet radome surface with droplets and rivulets was modeled in HFSS. For this specific example, the results at 45 ° (in azimuth) show that in the presence of rivulets on the radome surface, the attenuation in V is 0.8 dB compared to only 0.2 dB without rivulets. A similar effect is observed in the reflections.

CHAPTER 7

COST-PERFORMANCE MODEL

7.1   Introduction

One of the most important benefits of phased array antenna technology results from the way transmitter power is distributed across hundreds, or even thousands, of small active elements, rather than being concentrated in a single source (Magnetron, TWT, etc.). The state of the art of current RF technology offers components, such as power amplifiers, LNA, phase-shifters, and others with a high degree of reliability (< 1 $\times 10^{-6}$ failures per hour at component levels) [28]. Given this level of reliability, phased array radar systems can operate even with 20 % fewer T\R modules. By comparison, failure rates of mechanical moving parts and single power sources are considerably higher. A malfunction in a single component of a conventional mechanically-steered radar based on single RF source can bring the operation of the whole system to a halt. For instance, the magnetron used in the CASA IP1 radar system (for 15 kW operating at 9.41 GHz) has a failure rate of 200×10^{-6} h^{-1}, while the azimuth pedestal has a failure rate of about 50×10^{-6} h^{-1} [30], [74].

This chapter discusses the cost of the CASA phased radar system as a function of performance. Since cost and performance of the system depend on the reliability characteristics of components, we introduce a reliability model for the CASA phased array antennas.

7.2 Graceful degradation

Performance metrics include the following three measures a) the performance degradation of the Effective Radiated Power (ERP), b) the antenna gain in reception (G_R), and c) the mean-squared sidelobe level (MSLL) as function of the failure rate of the phased array antenna. Principally, we evaluate these parameters conservatively as a function of the failure rate (λ_F) of the T\R modules, since these modules have relatively higher failure rates in the overall system. The expressions to estimate the ERP, G_R, and MSLL as function of the failure rate and RMS random errors are presented by [75] and [37] are presented below:

$$ERP = 10 \log_{10} \left[(1 - \lambda_F)^2 (1 - \sigma_a^2 - \sigma_\phi^2) \right] \tag{7.1}$$

$$G_R = 10 \log_{10} \left[(1 - \lambda_F)(1 - \sigma_a^2 - \sigma_\phi^2) \right] \tag{7.2}$$

$$MSSL = 10 \log_{10} \left[\frac{\lambda_F + \sigma_a^2 + (1 - \lambda_F)\sigma_\phi^2}{\eta_a N (1 - \sigma_a^2 + \sigma_\phi^2)} \right] \tag{7.3}$$

where λ_F is the ratio between the number of failed elements (F) and the total number of active elements in the array (N). Terms σ_a and σ_ϕ represent the rms errors for amplitude and phase (discussed previously in chapters 4th and 5th), and η_a represents the aperture efficiency.

Figure 7.1 illustrates the CASA phase array antenna degradation performance versus T\R module failure rate percentage. For this case we assume same failure rate of 2.5×10^{-6} h^{-1} for transmission and reception, N= 64 (number of T\R modules), a taper efficiency of η_a=0.90, (for Taylor -25dB, $\bar{n}$=4), and rms random errors of σ_a=0.22 dB, σ_ϕ=1.66 (which represent the values that fit measured antenna patterns). The peak sidelobe level performance versus failure rate is calculated using the Rice

probability function, which estimates the probability of increase in peak sidelobe level as a function of the MSLL and the error free sidelobe level pattern [79].
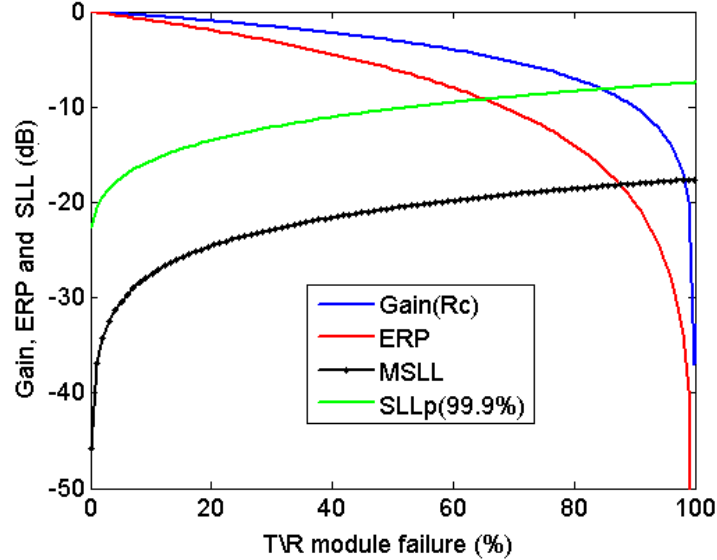
Figure 7.1. CASA phase array antenna degradation performance. (σ_a=0.22 dB, σ_ϕ=1.66 dB, N=64, η_a=0.90)

7.3   Reliability model for CASA phase array

The reliability model for the CASA phased array radar can be represented by two components as shown in Figure 7.2 1) Radar back-end, which consists of: up-down converter, digital receiver, beam controller and host computer and 2) Radar-front-end, which consist of: power supplies, backplane, T\R modules, elevation positioner, array antenna, and radome. In this analysis, the reliability model considers only the radar-front-end.

7.3.1   Radar-front-end reliability model

In the radar-front-end, two categories of components with similar characteristics can be distinguished. First, passive components - transmission lines, power divider-

combiners, array antenna, radome are those which do not require dc bias. Typically, the passive component contribution to life-cycle cost is negligible since the failure rate of a passive component is extremely low (typically less than 0.1×10^{-6} h^{-1} [74]). Second, active components, such as T/R modules, power supplies, and backplanes, are those components which require dc bias, such as transistors, switches, diodes and regulators. In this model, reliability information (failure rate or MTBF) provided by the manufacturers was used.
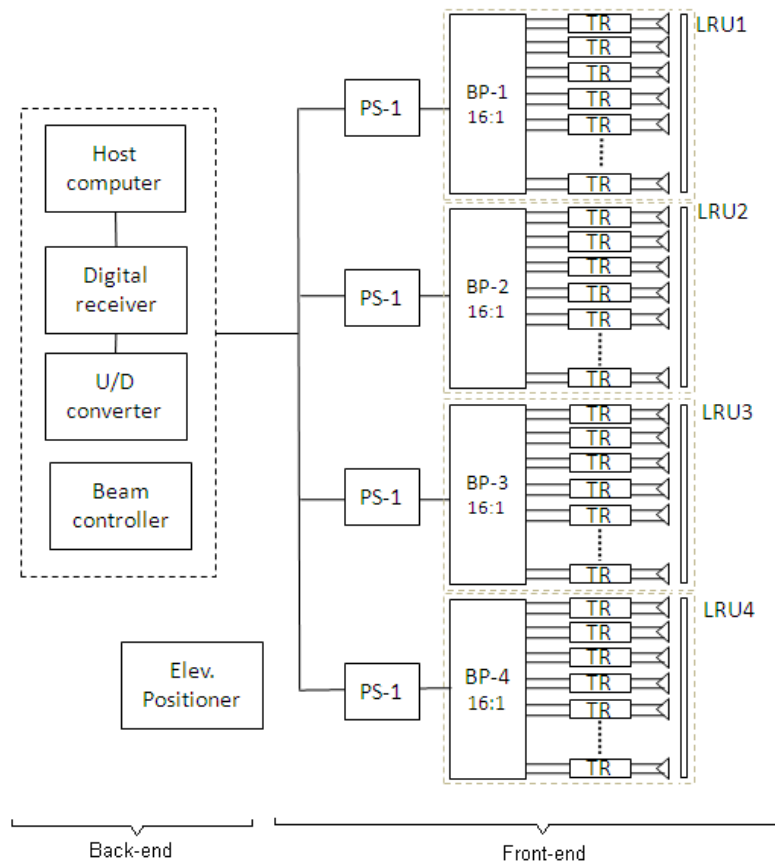
Figure 7.2. Reliability block diagram of CASA phased array radar.

In active phased array antennas (without moving mechanical parts), the components most critical for reliability are T\R modules and power supplies, since these

components drive more power and they operate at high temperature conditions. In the past, typical failure rates for X-band T\R modules are about $4x10^{-6}$ h^{-1} (for reception) and $8x10^{-6}$ h^{-1} (for transmission) [75], [76]. Current values are significantly better. Recently the OMMIC Corporation has announced the introduction of a new range of products to its catalogue which includes 6-bit phase shifters, 6-bit attenuators, and a set of completely integrated core chips at X-band and at C-band, with failure rates of $0.1x10^{-6}$ h^{-1}. The cost of a die in quantities of 10,000 units is about \$ 200 per T\R module [77].

In the CASA phased array antenna, the T\R module is a result of a customized design implemented in a printed circuit board (PCB) which comprises 6 circuit layers fabricated on a hybrid construction of Rogers 4350 and FR4. About 177 components are commercial-off-the-shelf (COTS) components. The RF components are plastic packed microwave monolithic integrated circuits (MMICs) that use Gallium Arsenide (GaAs) technology. The overall failure rate of the T\R module is about $2.5x10^{-6}$ h^{-1}. This value was estimated based on the failure rates of each component in the T\R module provided by the manufacturer. For a few components (resistors and capacitors), where the reliability information was not provided, a generic failure rate was estimated from the MIL-Handbook [74]. Table 7.1 presents the average failure rate (in descendent order) of the principal components in the T\R module. The highest failure rate in the T\R module belongs to the phase-shifter, followed by the LNA, temperature sensor, amplifiers, attenuators and regulators.

Table 7.2 presents the calculated failure rate of the other components in the CASA phased array radar front end, including the elevation positioner. After the elevation positioner, the T\R modules and power supplies are the components in the radar front end with higher individual failure rates. However considering the larger number of T\R modules, these modules represent the dominant component of consideration in the reliability model of the CASA radar system.

Table 7.1. Failure rate characteristics of principal components in T\R module for CASA phased array antenna.

Component category	Qty	$\lambda_F(10^{-6}\mathrm{hr}^{-1})$
Digital phase-shifter	1	0.161
LNA	1	0.113
Temp. sensor	1	0.065
Amplifiers	4	0.039
Digital attenuator	1	0.013
CI Regulators	7	0.048
Diugital CI	3	0.017
Connectors	5	0.016
Diodes	16	0.017
Resistors	58	0.007
Capacitors	65	0.005
IC oscillators	4	0.003
IC switchs	2	0.003
Total T\R module failure rate		2.5

Table 7.2. Failure rate characteristics of principal subsystem in the front-end and elevation positioner of CASA phased array radar. λ_{FT} are the result of multiplying λ_F and the number of components of each sub-system

Subsystem	Qty	λ_F x$10^{-6}(\mathrm{hr}^{-1})$	λ_{FT} x$10^{-6}(\mathrm{hr}^{-1})$
Elev. Positioner	1	10.3	10.3
T\R module	64	2.5	160
Power supplies	4	0.8	3.2
Backplane	3	0.7	2.1
Array antenna	4	0.1	0.4
Radome	1	0.1	0.1
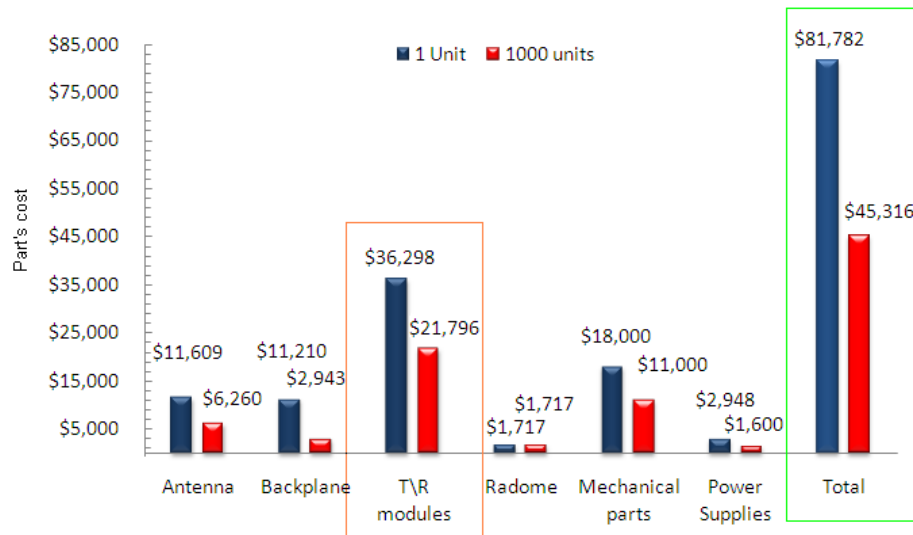
Figure 7.3. Summary of CASA phased array antenna cost-model

7.4 Phased array antenna cost-model

In this section we present the cost-model for the CASA phased array antenna front-end for a single prototype unit, and also for large production volumes (>1,000 units). The cost-model was obtained using formal quotes for quantities of (1, 10, 100 and 1,000 units) of each part of the system. In addition, we added a cost representing manufacturing and assembly. Figure 7.3 presents a summary of the costs for each sub-system of the radar front end. More details of those costs are presented in Appendix D. The overall cost of a single prototype is $ 81,782, and the estimated cost is $ 45,316 for mass production of 1,000 units. A reduction of about 45% of the unit cost can be obtained if large quantities (1,000 units) are produced. The largest proportion of the cost in the front system corresponds to T\R modules, which represent about 44% of the total cost of the radar front end. The cost of each T\R module is about $567.2 (for 100 units), which can reduce to $341 if large quantities (> 1000 units) are produced.

7.5 Life Cycle Parts Cost (LCC) model of CASA phased radar

The Life Cycle Cost (LCC) model for the CASA phased array front-end is determined as the sum of two elements (see 7.4). The first is the initial cost (C_i) of the radar system, which consists of the cost of parts, fabrication cost, and assembly cost. The second is the failure cost (C_F), which represents the cost of replacing components that have failed in the system. The failure cost (C_F) is evaluated using the expression 7.5 as function of time (T), the number of components (N), the failure rate (λ), and individual cost (C) for each sub-system (m) such as the T\R modules, power supplies, backplanes, array antenna, radome, etc.

$$LCC = C_i + C_F \tag{7.4}$$

$$C_F = T \sum \lambda_m N_m C_m \tag{7.5}$$

Figure 7.4 illustrates the calculated cost of failures (C_F) for each subsystem in the radar-front-end. As expected, the T\R modules constitute the major part of the overall failure cost over time. Considering this, the failure cost of the T\R modules can be extracted in 7.5 (expression 7.7). Since the failure cost of T\R modules is always higher than the other components, the expression 7.5, can be simplified in terms of the failure cost of the radar front end, yielding expression 7.9, which considers only the T\R modules.

$$C_F = T(\lambda_{TR} N_{TR} C_{TR}) + T \sum \lambda_k N_k C_k \tag{7.6}$$

$$C_F = C_{F-TR} + C_{F-OTHERS} \tag{7.7}$$

$$C_{F-TR} \gg C_{F-OTHERS} \qquad (7.8)$$

$$C_F = T(\lambda_{TR} N_{TR} C_{TR}) \qquad (7.9)$$
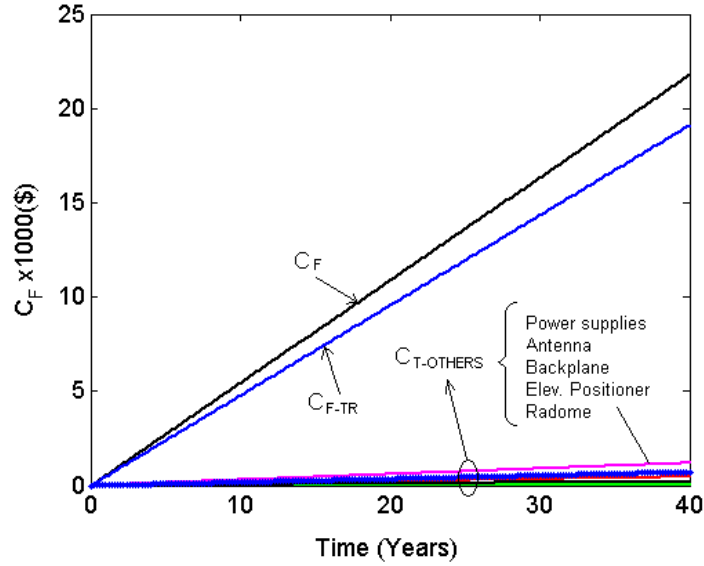
Figure 7.4. Failure cost of CASA phased array antenna subsystems. Cost of T\R modules failures represent the total failure cost in the radar front-end.

The input parameters for the LCC model are: the number of active elements in the array (N=64), the aperture efficiency ($\eta_a = 0.9$ for Taylor -25 dB $\bar{n}$=4),the rms random values for the amplitude and phase excitation of the array (σ_a=0.22 dB and σ_ϕ=1.66 °), the maximum duty cycle of the radar (DC=30 %), the failure rate, and the cost. Figure 7.5 presents the results of the performance model versus time for the gain and ERP loss, and also the degradation in time of the average and peak SLL.

In Table 7.3 the performance results illustrated in Figures 7.5 are combined with the results of the LCC model. The results for a period of 5 years indicate that 8 failures are likely in reception and 5 failures are likely in transmission. Althoug the

failure rate in the T\R module is the same for transmission and reception modes, the duty cycle of 30 % produce different failure rates for transmission and reception. With this number of failures, the receiver gain is reduced by -0.41 dB and the effective radiated power is reduced by -0.35 dB. Both reductions result in a radar sensitivity loss of -0.76 dB. In terms of sidelobe performance, a high probability (~99.9%) that the peak sidelobe level rises to -19.3 dB and the average sidelobe can reach values of -28 dB. The incurred cost to replace the failed T\R modules at the end of the 5th year represents about 4 % of the initial cost.

Table 7.3. Performance-cost model for CASA phase array radar system.

% Failures			Performance				Cost		
Time	Rc	Tx	G_R	ERP	MSLL	SLLp (99.9%)	C_F	LCC	C_F/C_i
(yrs)	(%)	(%)	(dB)	(dB)	(dB)	(dB)	x10^3($)	x10^3($)	(%)
0	0	0	-0.06	-0.06	-45.2	-22.67	0.0	45.3	0
1	2	1	-0.13	-0.12	-32.9	-21.55	0.3	45.6	1
5	8	3	-0.41	-0.35	-28.0	-19.32	1.7	46.9	4
10	15	7	-0.79	-0.65	-25.4	-17.85	3.3	48.6	7
15	23	10	-1.20	-0.96	-23.8	-16.68	5.0	50.3	11
20	31	13	-1.65	-1.29	-22.6	-16.12	6.7	52.0	15
25	38	16	-2.16	-1.62	-21.6	-15.48	8.4	53.7	18
30	46	20	-2.74	-1.97	-20.9	-14.92	10.0	55.3	22
35	54	23	-3.40	-2.33	-20.2	-14.42	11.7	57.0	26
40	61	26	-4.19	-2.77	-19.7	-14.07	13.4	58.7	30

7.6   Conclusion

A performance model was formulated based on the reliability characteristics of the CASA phased array antenna components and the antenna architecture. The design was carefully performed considering high reliable components.

The cost of the radar systems is determined by the T\R modules. Each one represents 45 % of the overall front-end radar cost. Minimizing the number of T\R modules in the array was the primary goal in this antenna architecture. T\R modules

154
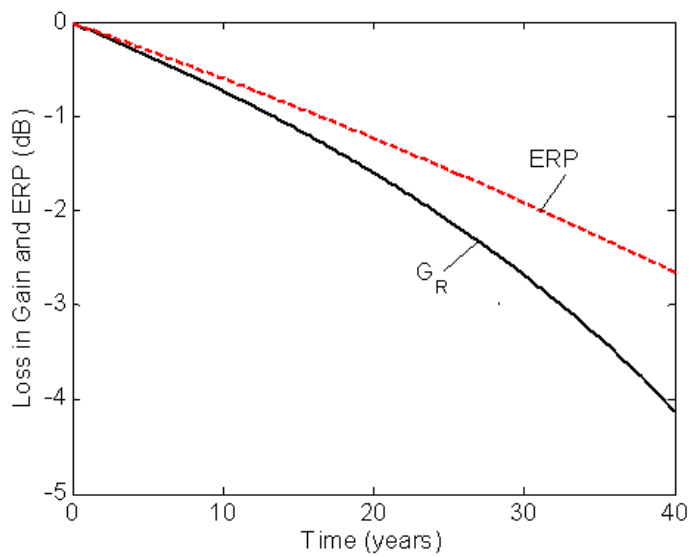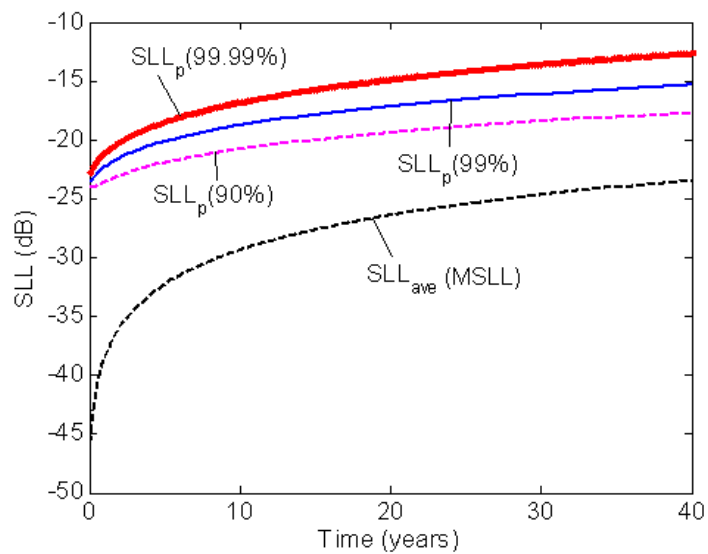
Figure 7.5. Performance model for CASA Phased array antenna. a) Loss in Gain (reception) and ERP versus time b) Average and peak SLL performance versus time.

also define the failure rate of the overall systems. In the radar system (after the servo mechanism) the T\R modules are the component with the highest failure rate. Although the T\R module presents a low individual failure rate ($2.5 \text{x} 10^{-6}$ h^{-1}), the number of them (in our case 64) makes the T\R failure rate a critical component that dictates the performance and cost of the overall radar system.

The overall cost of a single prototype is about \$ 81,782, while the estimated cost for a batch of 10 phased array antennas is \$ 55,888 each. For a volume of 100 units the cost is \$ 46,089 each and for a volume of 1,000 units the cost is \$ 45,316 each.

The performance model, cost model, and reliability model were integrated into one model to estimate the cost as a function of performance and time. The CASA phased array antenna presented a low cycle cost. The model includes only the cost of the radar-front-end, and the cost required to replace the failed component per unit of time.

CHAPTER 8

EPILOGUE

8.1 Summary

This dissertation presents a low-cost dual-polarized X-band phased array antenna for the CASA weather surveillance radar network. The array architecture combines one-dimensional, electronic beam steering with mechanical tilting to satisfy the cost and performance requirements for the CASA radar system. A prototype has been designed, fabricated and tested. The overall cost of a single prototype is about $ 81,782, while the estimated cost considering a 10,000 unit production volume is $ 45,316. The system was carefully designed to maximize the operational life time, and minimize the operational cost. A cost-performance model was developed to predict the radar performance for a 10 year life time constrained such that the incurred cost for repair is less than 12% of the initial part cots. Since its conception (January 2007), three revisions in the antenna array design and two revisions for the T\R modules were performed. In February 2010, a first demonstration of the functionality of the CASA phase array antenna (phase-tilt) were presented. The measured performance antenna patterns of 1 panel (18x32 elements) populated with 16 T\R modules demonstrated the concept of the antenna architecture and low cost. One year later (February 2011) the full array antenna (72x32 elements) populated with 64 T\R modules was completed.

The antenna satisfies the requirements for low profile (1.5 m x 1 m x 0.3 m) and low weight (<200 lb), ideal for field deployment based on existent infrastructure. The maximum uncertainty in the bias differential reflectivity, produced by the antenna,

is 0.25 dB and the two-way integrated cross polarization is better than -50 dB for the overall scanning range of $\pm$ 50 $^{\circ}$. For a volume scan of 90 $^{\circ}$ in azimuth and 12 $^{\circ}$ in elevation, the 50 W power transmitted permits a mean radar sensitivity between 9.4 to 14.3 dBZ. For the same scan volume, the antenna aperture size of 1m x 0.5m permits a mean spatial resolution between 0.39 km to 0.73 km when the CASA radar is operated in a network environment.

The CASA phased array antenna redefines the state-of-the-art of small radars for weather remote sensing. The prototype antenna also serves as a testbed and proof of concept for exploring a potential future network comprised of many antennas arranged in a dense network. The design of the CASA phased array antenna was successfully transferred to the CASA industrial and academic partnership. CASA has licensed the design to companies: ITT, EWR, Vaisala and Raytheon. The Microwave Remote Sensing Laboratory is currently adapting the design for a Space-Antenna Wind Retrieval Weather Radar System. The company, First RF, in collaboration with Raytheon used the CASA phased array antenna concept to implement a low-cost Phased array radar.

8.2   Conclusions

Since 2003, the CASA ERC concept of a network of small X-band radar has been shown to be the most effective solution to improve the lack of coverage of the existing US radar network. The short-range operation provides a fast and adaptive scanning radar that permits higher resolution and faster scanning updates. The benefits of using small radars (~1 m antennas) and transmitters having only tens of watts of transmitted power, implemented in a dense radar grid network with overlapped coverage, represents a new state-of-the-art for weather radar surveillance. CASA expended for each radar node the amount of $ 259 k (parts only) where 67 % of this

cost ($ 117 k) represents the cost in mechanical parts (pedestals, frame and mounting frame and radome) and $ 26 k is necessary to operate the radar each year.

CASA strongly believes that replacing the radar front-end with a phased array antenna can provide substantial benefits in the radar performance and an overall cost reduction in the radar network system. Phase array antenna technology is now a mature technology which has been demostrated to have great advantages in performance (fast scanning update, high temporal resolution, and multifunction capabilities). Eliminating the mechanical moving parts and distributing the performance of a single source across thousands of elements in the aperture array significantly improves the reliability of the overall system, reduces the initial cost, and considerably reduces the operational cost of the radar system. Initially a two-dimensional phased array was considered as an alternative solution for CASA. However the cost reduction expected in the active element (T\R modules) at large production volume did not satisfy the CASA cost requirements (< $ 50 k/panel). Today the commercial price of T\R module IC cores at X-band is $ 250. A 2-D array with 4096 (64x64 elements) represents more than $ 1M per panel. This cost is prohibitive for CASA.

In 2007, the dual-polarized phased array antenna called "Phase-tilt array" was conceived and presented as an alternative solution to improve the scanning radar update and to reduce the cost of the CASA IP1 radar network system. Because the antenna architecture only performs electronically scanning in the azimuth, the overall scanning of the phase-tilt radar also offers better temporal response in comparison with the conventional mechanical dish mechanically steered radar at a significant cost reduction. The antenna array architecture proposed combines an inexpensive (< $11 k) tilting mechanism to perform scanning in the elevation plane with an electronic phased array antenna in the azimuth plane.

System requirements and user needs were reviewed in order to define a set of radar specification to design the phased array antenna for use in weather surveillance in a

radar network environment. A trade-off analysis of the key design parameters of the phased array radar for a isolated single radar node and also as part of radar network was performed. The results of this analysis served to define a new set of radar specifications that then were used as input parameters for the CASA phased array antenna design. For short-range radars, as CASA proposed (less than 40 km), the losses in the antenna gain and beamwidth broadening due the electronically scanning performance does not have significant impact in radar sensitivity and spatial resolution. Comparing the radar sensitivity of the 3 radar nodes, small differences, less than 1.2 dB, can be obtained from the 3 and 4 panels with respect to the mechanically scanned radar. For spatial resolution for the radar node with 3 panels degrades by 25 % while for the 4 panel design resolution degrades 14 % with respect to radar scanned mechanically. When the radar nodes are deployed in a radar network, the mean values of the minimum radar sensitivity improves by 7 dB for the lowest altitude (0.05 km) and in 3 dB for highest altitude (3.2 km) for the three radar node configurations. An improvement factor of about 2.5 in the mean spatial resolution is obtained for a radar network observed at the lowest altitude (0.05 km), and an improvement factor of about 1.5 is obtained when radars are deployed to observed at the highest altitude (3.2 km) for all radar configurations.

To obtain the same radar sensitivity as the IP1 radar system (in a triangular radar network), between 50 W to 120 W peak power and a pulse width between 5 μs to 40 μs is required. Considering a radar network with 4 panels per node and a pulse width of 40 μs, a transmit peak power of 50 W is required to obtain a radar sensitivity (mean values) of 10 dBZ at 50 m altitude and 14 dBZ at 3.2 km altitude.

And novel antenna array architecture which provides dual-polarized capability was designed and implemented in a multilayer dielectric structure. The antenna element is an aperture coupled microstrip patch antenna. A center and symmetric series-feed network was used to interconnect the 32 element array in the elevation plane. A

customized synthesis method were implemented to obtain the geometry dimensions of the linear antenna array geometry. The model was implemented in Matlab and validated with simulated and measured results. The maximum number of elements that can be synthesized using this method is 32 elements. For a higher number of elements, the losses in the dielectric and serpentine lines demand large slot apertures, which are not practical considering the limited space because the serpentine lines for both polarizations. Another factor that limits the maximum number of elements to 32 is the maximum size for a multilayer PCB fabrication process. Simulation process were performed in Ansoft Designer and HFSS.

The array was fabricated and then tested. The results (s-parameters and radiation patterns) present good agreement between the calculated and simulated results.

To protect the antenna from the ravages of the environment, such as wind, snow, ice, rain and temperature changes. A wall sandwich radome composed with a thick core dielectric material based on a foam core and a skin hydrophobic material was designed and implemented. The radome provides excellent electromagnetic transparence. The insertion losses are lower than -0.4dB, the reflection was below -25 dB, and the induce cross-polarization ratio below -34 dB.

A customized T\R module was designed, fabricated, and tested. The design uses a "Common-leg" configuration, in order to reuse the phase shifter, which represents the most critical component in terms of cost and reliability.

Measured antenna patterns of the full array (64x32 elements) were performed in the Near-Field range chamber of the CASCA antenna laboratory at UMASS. The measured results validate the design procedure and confirm that the design satisfies the required performance for the CASA phased array radar. The cross-polarization for each beam position (0 °, 15 °, 30 ° and 45 ° in the azimuth plane) are below -25 dB (5 dB better than required). The peak sidelobe level is below -23 dB (2 dB, better than required for CASA weather radar). The measured results shows that the

mismatch between co-polar patterns is lower than 7.2 % when the antenna is scanned from broadside to ±45 °. The active reflection coefficient versus frequency and scan angle were estimated from the embedded element patterns. Values below -10 dB were obtained for a scanning range of ±45 ° and a required frequency range between 9.3 GHz to 9.4 GHz .

The bias differential reflectivity due to the antenna patterns varies from -2.6 dB to 4.34 dB, principally due to the effect of the difference in the gains of co-polar patterns in H and V due the ripples in the element patterns. A maximum standard deviation of 0.25 dB was found at 45 ° scanning at azimuth plane. Below -50 dB is the estimated $ICPR_2$ (two-way) for the overall scanning range ($\pm$ 50°).

An analytical model to estimate the attenuation, reflection and depolarization of the radar signals of a wet radome surface was proposed and implemented. The model was implemented and effectively applied to several scenarios (including semi-spherical, cylindrical, flat radomes with non-hydrophobic, hydrophobic and super-hydrophobic skin surfaces). The results are very satisfactory and have been validated with a numerical simulation in HFSS and experimental data

A performance model presented was formulated based on the reliability characteristics of the CASA phased array antenna components and the antenna architecture, based on the use of high reliable components. The cost of the radar systems is constrained by the T\R modules. In total, they represents 45 % of the overall front-end radar cost. Minimizing the number of T\R modules in the array was the primary goal in this antenna architecture. T\R modules also constrain the overall failure rate of the system. Although the T\R modules present a low individual failure rate ($2.5 \times 10^{-6} h^{-1}$), the large number of them (in our case 64) makes the T\R failure rate a critical component that dictates the performance and cost of the overall radar system.

The performance model, cost model, and reliability model were all integrated in one model to estimate the cost as a function of performance and time. The CASA

phased array antenna presented a very low cycle cost. The model includes only the cost of the radar-front-end, and the cost required to replace failed components per unit of time.

APPENDIX A

ANTENNA PATTERNS VERSUS FREQUENCY
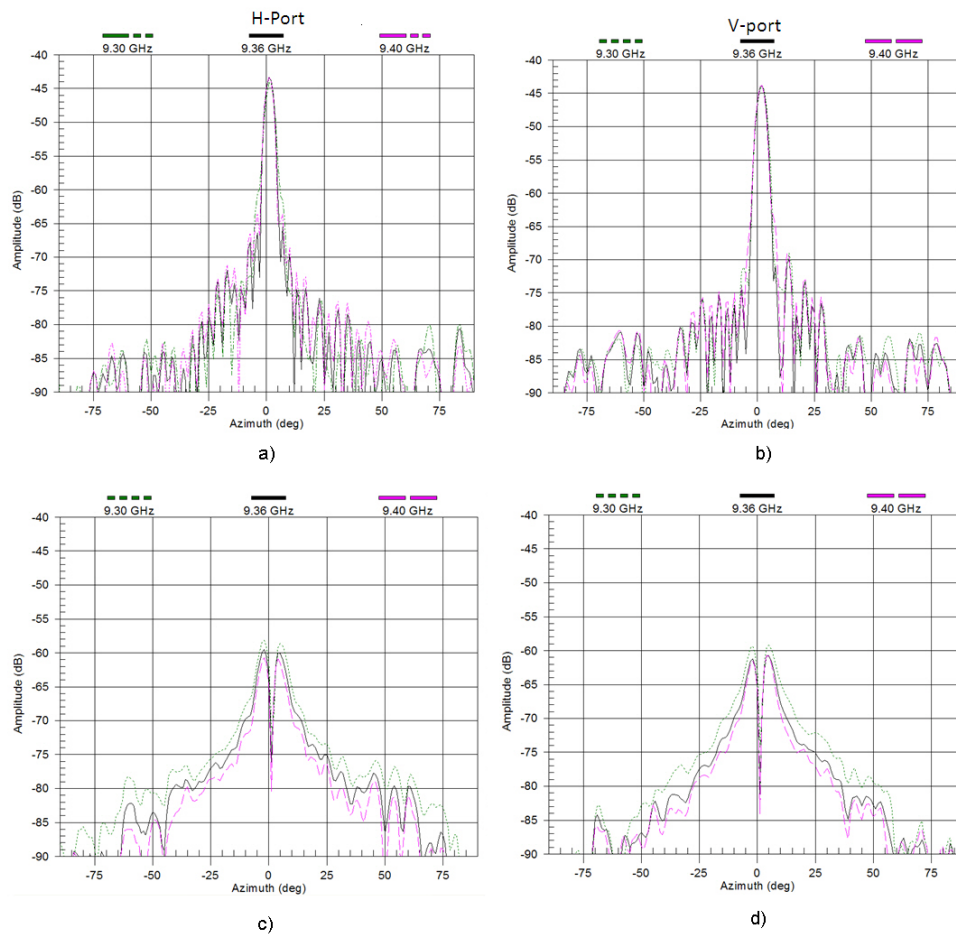
Figure A.1. Measured elevation antenna patterns versus frequency (9.3 GHz, 9.36 GHz and 9.4 GHz) of a column 9th embedded in a array of 18x32.
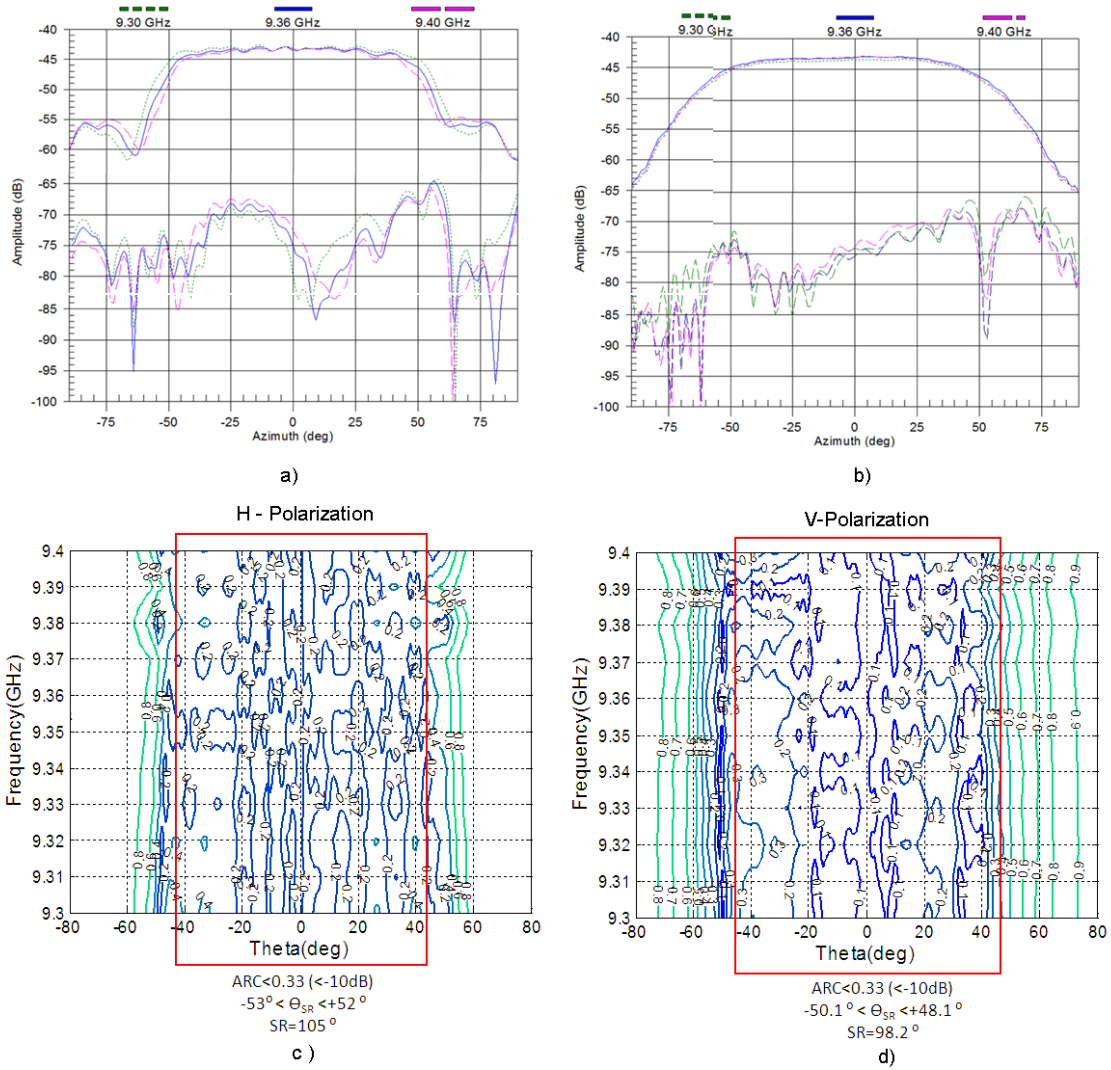
Figure A.2. a-b) Measured embedded antenna element pattern versus frequency (9.3 GHz, - 9.36 GHz and 9.4 GHz) of column 9th in array of 18x32 elements. c-d) Calculated active reflection coefficients as function of the measured embedded element patterns

APPENDIX B

FSS RADOME UNIT CELL GEOMETRY
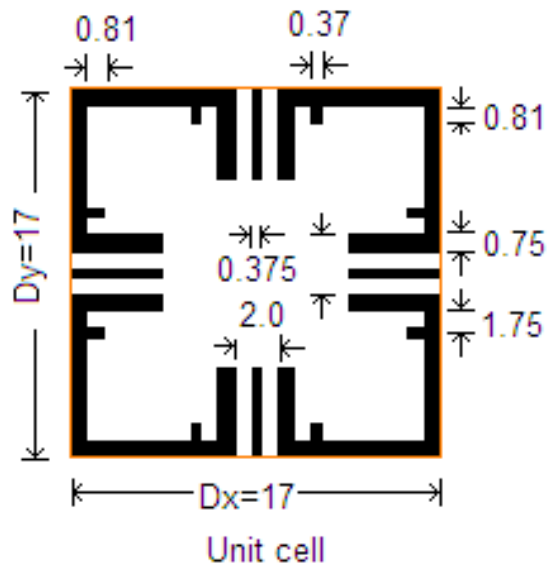
Figure B.1. Geometry of unite cell model of modified Jerusalem Cross for FSS radome simulated in Ansoft designer. All units are in mm

APPENDIX C

RADOME MATERIAL PROPERTIES

Table C.1. Properties for radome materials

Material	Density	Dielec. Const.	Tang. Loss	Therm. Cond.	Water Abs	Cost
	g/cm^3	10 GHz	10 Ghz	W/mk	98HR (%)	\$/m^2
Rohacell 31HF	0.0031	1.046	0.0017	0.029	23	91
Honeycomb HR11/83	0.0048	1.06-1.09	-	0.064	4.4	100
GoreTex RA7906	0.2-2.0	1.55	0.0005	0.1-0.3	0.0	280
Rogers 5880 LZ	1.37	1.96	0.0027	0.2-0.22	0.22	1,219
Nelco SI	1.79	3.2	0.0080	0.294	0.10	77

Table C.2. Advancing (θ_A), receiding(θ_R) and histeresis (θ_H) angles for non-hydrophobic, hydrophobic and suoper-hydrophobic materials used for the outer skin radome layer.

Material	Category	θ_A	θ_R	θ_H
Fiber Glass	None	105°	15°	82°
GoreTex	Hydrophobic	120°	47°	73°
Teflon	Hydrophobic	120°	79°	41°
Teflon S240	Super Hydrop.	150°	144°	6°
Hirec100	Super Hydrop.	151°	144°	7°
Cytonix WX2100	Super Hydrop.	160	151	9

APPENDIX D

CASA PHASED ARRAY ANTENNA COST MODEL

	Concept	Quoted by	Qty	Unit cost ($)				Total Panel Cost (1 panel) ($)			
				1	10	100	1,000	1	10	100	1,000
Antenna	Passive array antenna fabrication (with	Cirex	4	$ 2,080	$ 1,261	$ 1,114	$ 1,031	$ 8,320	$ 5,044	$ 4,455	$ 4,125
	Rohacell		1	$ 217	$ 217	$ 217	$ 217	$ 217	$ 217	$ 217	$ 217
	SMP conectors	Digi_key, Hittite	128	$ 8	$ 8	$ 8	$ 5	$ 1,024	$ 639	$ 639	$ 639
	Cables (SMP-SMA) and SMP connectors	MS Electronics	128	$ 26	$ 16	$ 16	$ 10	$ 2,048	$ 1,280	$ 1,280	$ 1,280
BackPlane	Parts (RF and Digital)	Digi_key, Hittite	4	$ 233	$ 179	$ 132	$ 132	$ 930	$ 718	$ 530	$ 527
	SMA-SMA cables	Custome Cables	128	$ 21	$ 11	$ 11	$ 8	$ 1,408	$ 1,024	$ 1,024	$ 1,024
	Power Combiner/ Divider enclossure (*)	Cirexx	4	$ 160	$ 32	$ 22	$ 18	$ 640	$ 128	$ 88	$ 72
	Board fabrication	Cirexx	4	$ 1,000	$ 580	$ 296	$ 270	$ 4,000	$ 2,320	$ 1,184	$ 1,080
	Board Assembly	Cirexx	4	$ 1,058	$ 181	$ 63	$ 60	$ 4,232	$ 724	$ 252	$ 240
T/R Module	Parts (RF and Digital)	Digi_key, Hittite	64	$ 438	$ 431	$ 374	$ 306	$27,594	$21,312	$19,572	$ 19,572
	Board fabrication	Cirex	64	$ 880	$ 187	$ 37	$ 22	$ 2,624	$ 1,786	$ 1,402	$ 1,402
	Board Assembly	Cirex	64	$ 500	$ 116	$ 6	$ 5	$ 4,672	$ 349	$ 310	$ 310
	Enclosure	Amherts Machine	64	$ 36	$ 22	$ 12	$ 8	$ 1,408	$ 614	$ 512	$ 512
Mechanical parts	Elevation positioner	Direct Perception	1	$16,000	$14,000	$10,000	$10,000	$16,000	$14,000	$10,000	$ 10,000
	Frame, enclosure and Yoke (*)	-	1	$ 2,000	$ 1,400	$ 1,200	$ 1,000	$ 2,000	$ 1,400	$ 1,200	$ 1,000
Radome	Radome (GoreTex Fabric)	Gore Tex	1	$ 817	$ 817	$ 817	$ 817	$ 817	$ 817	$ 817	$ 817
	Foam	Rohacell	1	$ 900	$ 900	$ 900	$ 900	$ 900	$ 900	$ 900	$ 900
Others	Power supplies	-	4	$ 737	$ 654	$ 427	$ 400	$ 2,948	$ 2,616	$ 1,708	$ 1,600
	Total cost ($)							$ 81,782	$ 55,888	$ 46,089	$ 45,316

Notes:
(*) Assumed values
File: Cost Model-Phase Tilt_Jsalazar
Dreated: April 1rst.2009
Updated: May 1rst. 2012
Revision II by:
  Jorge Salazar
  Rafael Medina

a)

b)
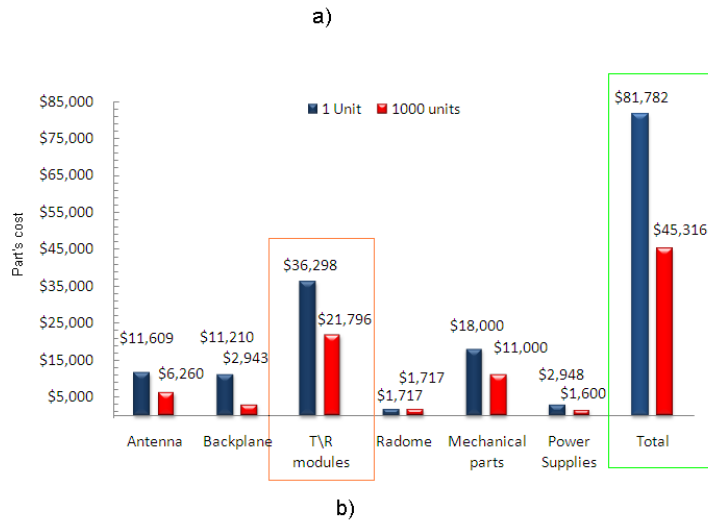
Figure D.1. Cost-model for CASA phased array antenna. a) Cost detailed for each part of the phased array antenna and b) Summary of CASA phased array antenna in bar chart.
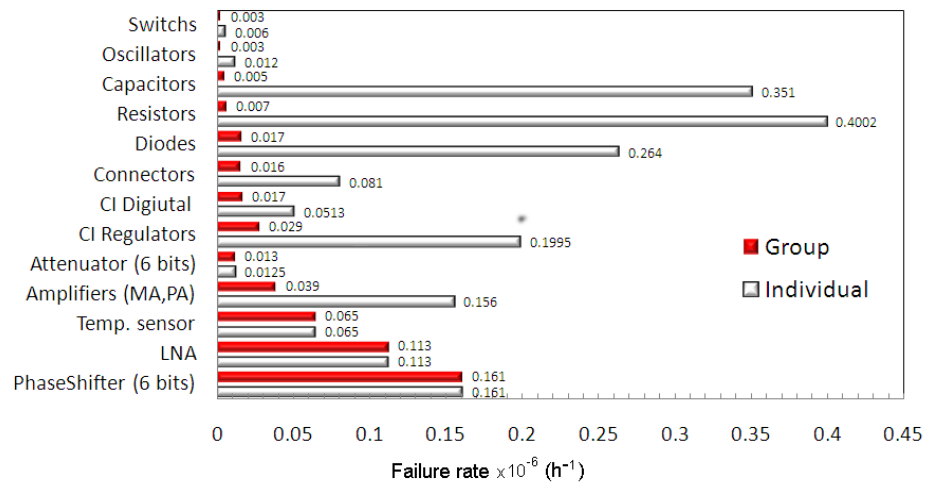
Figure D.2. Failure rate of components in T\R module

Item	Qty	Value	Part Number	Distributor	Unit Price	Failure rate per 10^6 hrs	Total faiulre rate per 10^-6 hrs	MBTF(years)	Price each 1	10	100	500	1000	Total 1	10	100	500	1000
1	36	100pF	ECJ-0EB1E682K	Digi-Key	0.18	0.00360	0.389	293.609	0.18	0.114	0.0409	0.0209	0.01476	6.48	4.104	1.4724	0.7517	0.53136
2	2	1uF	TCA1C105M8R	Digi-Key	0.33	0.00180	0.011	10569.931	0.33	0.283	0.247	0.195	0.1625	0.66	0.566	0.494	0.39	0.325
3	1	1uF	TCA1C106M8R	Digi-Key	0.33	0.00180	0.005	21139.861	0.33	0.283	0.247	0.195	0.1625	0.33	0.283	0.247	0.195	0.1625
4	1	2.2uF	TCA1C225M8R	Digi-Key	0.33	0.00180	0.005	21139.861	0.33	0.283	0.247	0.195	0.1625	0.33	0.283	0.247	0.195	0.1625
5	2	0.01uF	ECJ-1VB1E103K	Digi-Key	0.33	0.00360	0.022	5284.965	0.33	0.283	0.247	0.195	0.1625	0.66	0.566	0.494	0.39	0.325
6	5	10uF	TCA1C106M8R	Digi-Key	0.33	0.00180	0.027	4227.972	0.33	0.283	0.247	0.195	0.1625	1.65	1.415	1.235	0.975	0.8125
7	16	100nF	ECJ-0EB1A104K	Digi-Key	0.0033	0.00360	0.173	660.621	0.0033	0.033	0.0117	0.006	0.00423	0.0528	0.528	0.1872	0.0957	0.06768
8	2	0.1uF	F971V104MAA	Digi-Key	0.0394	0.00180	0.011	10569.931	0.0394	0.394	0.3377	0.2814	0.22512	0.0788	0.788	0.6754	0.5628	0.45024
9	2	CZRU52C5V1	CZRU52C5V1	Digi-Key	0.46	0.00330	0.036	3144.773	0.46	0.333	0.1961	0.1184	0.0925	0.92	0.666	0.3922	0.2368	0.185
10	4	CZRU52C2	CZRU52C2	Digi-Key	0.53	0.00330	0.073	1572.386	0.53	0.378	0.226	0.1344	0.105	2.12	1.512	0.904	0.5376	0.42
11	2	SMA	142-0761-851	Digi-Key	8.45	0.00540	0.022	5284.965	8.45	7.524	5.5278	4.2999	3.83875	16.9	15.048	11.0556	8.5999	7.6775
12	1	HEADER 15X2	TFML-115-01-S-D-RA	Digi-Key	5.21	0.00540	0.011	10569.931	5.21	3.764	3.088	2.75	2.702	5.21	3.764	3.088	2.75	2.702
13	1	EXB-E10C472J	EXB-E10C472J	Digi-Key	0.42	0.00230	0.007	16544.239	0.42	0.389	0.315	0.262	0.21	0.42	0.389	0.315	0.262	0.21
14	1	EXB-E10P472J	EXB-E10P472J	Digi-Key	0.42	0.00230	0.007	16544.239	0.42	0.389	0.315	0.262	0.21	0.42	0.389	0.315	0.262	0.21
15	13	4.7K	ERJ-2GEJ472X	Digi-Key	0.08	0.00230	0.090	1272.634	0.08	0.081	0.0436	0.0251	0.01711	1.04	1.053	0.5668	0.3263	0.22243
16	4	127 Ohm	RC1206FR-07127RL	Digi-Key	0.088	0.00230	0.028	4136.060	0.088	0.082	0.0444	0.0255	0.1737	0.352	0.328	0.1776	0.1018	0.6948
17	5	200	ESR03EZPJ241	Digi-Key	0.142	0.00230	0.035	3308.848	0.142	0.142	0.0746	0.0439	0.02996	0.71	0.71	0.373	0.2195	0.1498
18	4	4.7K	ERJ-2GEJ472X	Digi-Key	0.08	0.00230	0.028	4136.060	0.08	0.081	0.0436	0.0251	0.01711	0.32	0.324	0.1744	0.1004	0.06844
19	4	210	ERJ-2RKF2100X	Digi-Key	0.08	0.00230	0.028	4136.060	0.08	0.081	0.0436	0.0251	0.01711	0.32	0.324	0.1744	0.1004	0.06844
20	1	200	ERJ-P06J201V	Digi-Key	0.0165	0.00230	0.007	16544.239	0.0165	0.165	0.0986	0.058	0.0348	0.0165	0.165	0.0986	0.058	0.0348
21	2	1.5K	ERJ-2GEJ152X	Digi-Key	0.08	0.00230	0.014	8272.120	0.08	0.081	0.0436	0.0251	0.01711	0.16	0.162	0.0872	0.0502	0.03422
22	1	100 Ohm	MCR01MZPJ101	Digi-Key	0.074	0.00230	0.007	16544.239	0.074	0.0398	0.0398	0.0229	0.0156	0.074	0.0398	0.0398	0.0229	0.0156
23	3	2.4 Kohms	ERJ-3GEYJ242V	Digi-Key	0.08	0.00230	0.021	5514.746	0.08	0.081	0.0436	0.0251	0.01711	0.24	0.243	0.1308	0.0753	0.05133
24	3	100 Ohm	ERJ-3GEYJ101V	Digi-Key	0.08	0.00230	0.021	5514.746	0.08	0.081	0.0436	0.0251	0.01711	0.24	0.243	0.1308	0.0753	0.05133
25	1	487 Ohm	ERJ-3EKF4870V	Digi-Key	0.08	0.00230	0.007	16544.239	0.08	0.081	0.0436	0.0251	0.01711	0.08	0.081	0.0436	0.0251	0.01711
26	2	49.9	ERJ-2RKF49R9X	Digi-Key	0.098	0.00230	0.014	8272.120	0.098	0.098	0.053	0.0304	0.02074	0.196	0.196	0.106	0.0608	0.04148
27	8	49.9 (165)	ERJ-2RKF49R9X	Digi-Key	0.098	0.00230	0.055	2068.030	0.098	0.098	0.053	0.0304	0.02074	0.784	0.784	0.424	0.2432	0.16592
28	5	100 Ohm (140)	MCR01MZPJ101	Digi-Key	0.074	0.00230	0.035	3308.848	0.074	0.0398	0.0398	0.0229	0.0156	0.37	0.199	0.199	0.1143	0.078
29	2	300 Ohm	ERJ-3GEYJ301V	Digi-Key	0.071	0.00230	0.014	8272.120	0.071	0.071	0.0382	0.022	0.01499	0.142	0.142	0.0764	0.0439	0.02998
30	4	LOADSW	FDC6331L	Digi-Key	0.78	0.00100	0.012	9512.938	0.78	0.582	0.4365	0.2716	0.25802	3.12	2.328	1.746	1.0864	1.03208
31	3	N74LVC2G14DC	SN74LVC2G14DCKR	Digi-Key	0.4	0.00570	0.053	2153.466	0.4	0.4	0.24	0.1328	0.112	1.2	1.2	0.72	0.3984	0.336
32	2	LM317DCY	LM317DCYR	Digi-Key	0.62	0.00950	0.057	2002.724	0.62	0.62	0.3465	0.2156	0.20484	1.24	1.24	0.693	0.4312	0.40968
33	2	AP1117Y33L	AP1117Y33L	Digi-Key	0.95	0.00950	0.057	2002.724	0.95	0.95	0.63	0.525	0.42	1.9	1.9	1.26	1.05	0.84
34	1	AP1117Y25L	AP1117Y25L	Digi-Key	0.95	0.00950	0.029	4005.447	0.95	0.95	0.63	0.525	0.42	0.95	0.95	0.63	0.525	0.42
35	1	LD1117S12TR	LD1117S12TR	Digi-Key	0.77	0.00950	0.029	4005.447	0.77	0.595	0.51	0.425	0.34	0.77	0.595	0.51	0.425	0.34
36	1	3S100E-4VQG100	C3S100E-4VQG100	Digi-Key	9.48				9.48	9.48	9.48	9.48	9.48	9.48	9.48	9.48	9.48	9.48
37	1	M25PE10	M25PE10-VMN6P	Digi-Key	2.1				2.1	1.65	1.4	1.15	0.875	2.1	1.65	1.4	1.15	0.875
38	1	E-25.000MHZ-L	OSE-25.000MHZ-LC-	Digi-Key	3.47				3.47	3.21	2.2275	1.881	1.881	3.47	3.21	2.2275	1.881	1.881
39	1	TC74	TC74A0-5.0VCTTR	Digi-Key	1.34	0.06500	0.195	585.412	1.34	1.34	1.08	1.08	0.98	1.34	1.34	1.08	1.08	0.98
40	1	LM337	LM337IMP/NOPB	Digi-Key	1.86	0.00950	0.076	1502.043	1.86	1.86	1.02	0.78	0.78	1.86	1.86	1.02	0.78	0.78
9	10	MPP4203	MPP4203	Microsemi	1.2	0.00360	0.198	576.542	1.2	1.2	1.2	1.2	1.2	12	12	12	12	12
13	2	SMP	P606-6CC	Tensolite	16.54	0.00540	0.022	5284.965	16.54	16.54	13.4	13.4	13.4	33.08	33.08	26.8	26.8	26.8
20	2	50 Ohm	S0202AF50R0FEB	SOTA	4.16	0.00230	0.014	8272.120	4.16	4.16	4.16	2.79	2.25	8.32	8.32	8.32	5.58	4.5
35	2	HMC232LP4	HMC232LP4	Hittite	30.51	0.00442	0.009	12913.490	30.51	30.51	27.25	27.25	23.37	61.02	61.02	54.5	54.5	46.74
36	3	HMC441LP3	HMC441LP3	Hittite	18.28	0.0880	0.264	432.406	18.28	18.28	16.33	16.33	12.52	54.84	54.84	48.99	48.99	37.56
37	1	HMC591LP5	HMC591LP5	Hittite	45.05	0.0390	0.039	2927.058	45.05	45.05	40.23	40.23	35.11	45.05	45.05	40.23	40.23	35.11
38	1	HMC642LC5	HMC642LC5	Hittite	121.95	0.1610	0.161	709.039	121.95	121.95	108.88	108.88	84.67	121.95	121.95	108.88	108.88	84.67
39	1	HMC425LP3	HMC425LP3	Hittite	12.23	0.0125	0.013	9132.420	12.23	12.92	10.92	10.92	9.18	12.23	12.92	10.92	10.92	9.18
40	1	HMC564LC4	HMC564LC4	Hittite	20.94	0.1130	0.113	1010.223	20.94	20.94	18.7	18.7	15.91	20.94	20.94	18.7	18.7	15.91
	177					Total Failure rate	2.5							438.136	431.168	374.031	362.71	305.809

Figure D.3. T\R module components cost and failure rate information

170

BIBLIOGRAPHY

[1] Paul L. Smith, James Frost Davis, Eastwood IM, Jefrey K. Lazo, et al., "Evaluation of the Mutifuction Phased Array Radar Planning Process". *The National Academy press*, Washington , D.C., 2008.

[2] D.J. McLaughlin et al., "Distributed Collaborative Adaptive Sensing (DCAS) for improved Detection, Understanding and Predicting of Atmosphere Hazards", *in Proc. Of 85th AMS Annual Meeting 2005*, San Diego, CA.

[3] McLaughlin, D., D. Pepyne, V. Chandrasekar, B. Philips, J. Kurose, et al., "Short-wavelength technology and the potential for distributed networks of small radar systems". *Bull. Amer. Meteor. Soc.*, 90, 1797-1817.

[4] P. Meischner, C. Collier, A Illingworth, J. Joss and W. Randeu., "Advanced Weather Radar Systems in Europe: The COST 75 Action", *Bulletin of the American Meteorological Society*, Vol.78. No. 7, pp. 1411-1430., July 1997.

[5] Shapiro, A., P. Robinson, J.Wurman, J. Gao, "Single-Doppler Velocity Retrieval with Rapid-Scan Radar Data". *Journal of Atmospheric and Oceanic Technology*, 20, 1758–1775, 2003.

[6] H.Bluestein, R.Tanamachi, J.Houser I.Popstefanija, B.Seeger, R.Bluth, J.B.Knorr, "Use of a mobile, phased-array, X-Band Doppler radar to study severe convective storms and tornadoes" *Proceedings The Fifth European Conference on Radar in Meteorology and Hydrology* 2008.

[7] Heilselman, P. L., D. L. Prriegnitz, K. L. Manross, T. M. Smith, and R.W. Adams, "Rapid Sampling of Severe Storms by the National Weather Radar Testbed Phased Array Radar". *Weather Forecasting,* 23, 808-824., 2008.

[8] Douglas Carlson, Jeffrey Herd, Sean Duffy, Mark Weber, Glenn Brigham, Michael Rachlin, Daniel Curcio, Cheryl Liss, Chris Weigand, "Low cost Phased Array Radar: The Multifunction.

[9] Crum, T. D., and R. L. Alberty, "The WSR-88D and the WSR-88D Operational Support Facility". *Bull. Amer. Meteor. Soc.*, 74, 1669–1687., 1993.

[10] Evans, J., and D. Turnbull, "Development of an automated windshear detection system using Doppler weather radar". *Proc. IEEE*, 77,1661-1673., 1989.

[11] Istok, M.J., M.A. Fresch, A.D. Stern, R.E. Saffle, B.R. Klein, N. Shen, D.J. Stein III, Y. Song, and W.M. Blanchard, "Future Terminal Doppler Weather Radar (TDWR) Products for NWS Operations", *23rd Conf on Interactive Information and Processing Systems, Amer. Meteor. Soc.*, San Antonio, TX., 2007.

[12] Brotzge, J., D. Andra, K. Hondl, and L. Lemon, "A case study evaluating Distributed, Collaborative, Adaptive Scanning: Analysis of the May 8th, 2007, Minisupercell Event". *Preprints, Symposium on Recent Developments in Atmospheric Applications of Radar and Lidar, AMS Conf.*, New Orleans, LA.

[13] A. Puzella, R. Alm., "Air-Cooled, Active Transmit/Received Panel Array," *2007 IEEE Radar Conference.*

[14] Salazar, J.L, R. Medina, J.Knapp, and D. J, McLaughlin, "Phase-Tilt Array Antenna Design for Distributed Radar Network for Weather Sensing". *IEEE International Symposium on Geosciences and Remote Sensing*, Boston, MA., 2008.

[15] J.M. Trabal, I. Zawadzki and D.J. McLaughlin, "A Method to Correct for Wet Radome Attenuation in CASA Radars by the Use of a Contiguous WSR-88D Radar", *ERAD 2008,* Helsinki, Finland.

[16] Y. Liu, V. N. Bringi and M. Maki, "Improved rain attenuation correction algorithms for radar reflectivity and differential reflectivity with adaptation to drop shape model variation", *Proc. IGARSS*, vol. 1, pp. 1910-1913, Colorado, July 2006.

[17] S. Lim, V. Chandrasekar, P. lee, and A. P. Jayasumana, "Reflectivity retrieval in a networked radar environment: demonstration from the CASA IP1 radar network", *IEEE International Symposium on Geosciences and Remote Sensing*, Barcelona, July 2007.

[18] Brown, R. A., R. M. Steadham, B. A. Flickinger, R. R. Lee, D. Sirmans, and V. T. Wood, "New WSR-88D volume coverage pattern 12: Results of field tests. *Wea. Forecasting*, 20, 385–393.

[19] Brotzge, J., K. Droegemeier, and D. McLaughlin, "Collaborative Adaptive Sensing of the Atmosphere (CASA): New radar system for improving analysis and forecasting of surface weather conditions". *Journal Transportation Research Board*, 1948,145-151., 2006.

[20] Doviak, R.J., D.S. Zrnic, "Doppler Radar and Weather Observations, *Academic Press*, 562 pp., 1993.

[21] Ian Anderson., "Measurement of 20-GHz Transmission Through a Radome in Rain".,*IEEE Transaction in Antennas and Propagation*, Vol.AP-23, No5, September 1975.

[22] A.J.Fenn.,"Measurements of Wet Radome Transmission Loss and Depolarization Effects in Simulated Rain at 20 GHz"., *10th International Conference on Antennas and Propagation*, 14-17, April 1997.

[23] Mikko Kurri and Asko Huuskonen., "Measurement of the Transmission Loss of a Radome at Different Rain Intensities"., *Journal of Atmospheric and Oceanic Technology*, Vol.25, Dec. 2007.

[24] R. Bechini, V. Chandrasekar, R.Cremonini and S.Lim, "Radome Attenuation at X-Band Radar Operations", *ERAD 2010 The Sixt European Conference on Radar Meteorology and Hydrology.*

[25] Weigand, R.M., "Performance of a water-repellent radome coating in an airport surveillance radar," *Proceedings of the IEEE* , vol.61, no.8, pp. 1167- 1168, Aug. 1973.

[26] P. Schuh, H. Sledzik, R. Reber, A. Fleckenstein, R. Leberer, M. Oppermann, R. Quay, F. van Raay, M. Seelmann-Eggebert, R. Kiefer, and M. Mikulla, "GaN MMIC based T/R-Module front-end for X-Band applications," in *European Microwave Integrated Circuit Conference Proceedings, (Amsterdam)*, pp. 274 - 277, Oct. 2008.

[27] Golden, K., Bessemoulin, A., Dadello, A., Hales, P. "A 3-chip MMIC solution for X-Band phased array radar," Microwaves, Communications, Antennas and Electronics Systems (COMCAS), *2011 IEEE International Conference on* , vol., no., pp.1-4, 7-9 Nov. 2011

[28] Carlo Kopp, "Active Electronically Steered Arrays A Maturing Technology", *Australian Aviation*, June 2002.

[29] Jorge L. Salazar, Anthony P. Hopf, Robert F. Contreras, Brenda Philips, Eric J. Knapp, David McLaughlin, Jerry Brotzge, Keith Brewster, "Coverage Comparison of Short Range Radar Networks vs. Conventional Weather Radars: Case Study in the Northwestern United States". *IGARSS 2009*: 964-967

[30] Junyent, F., V. Chandrasekar, D. McLaughlin, E. Insanic, and N. Bharadwaj, 2010: "The CASA Integrated Project 1 Networked Radar System", *J. Atmos. Oceanic Technol.*, 27, 61-78.

[31] Bharadwaj, Nitin; Chandrasekar, V., "Networked Waveform System for Range Velocity Ambiguity Mitigation," *Geoscience and Remote Sensing Symposium, 2008. IEEE International* , vol.4, no., pp.IV -1010-IV -1013, 7-11., July 2008.

[32] V. Chandrasekar, F. Junyent. "CASA IP5 System Requirements", *CASA internal document*, 2009.

[33] Apoorva Bahaj. "Radar site requirements and sitting options", *CASA internal document*, June 2011.

[34] Gerald V. Trunk., "Optimal Number of Phased Array Faces for Horizon and Volume Surveillance - Revisited", *in IEEE*, 2003.

[35] J. Salazar, E. Knapp, D. J. McLaughlin. "Antenna Design Trade-offs for Dense Distributed Radar Network for Weather Sensing", *Preprints Proceedings of 33rd International Conference on Radar Meteorology 2007*, Cairns, Australia.

[36] R. J Mailloux, "Phased Array Antenna Handbook", in *Artech House*, 2005, Norwood, MA, USA.

[37] Merrill I. Skolnik, " Radar handbook" *McGraw Hill Companies*, 1990.

[38] V. Chandrasekar and R. Jeffrey Keeler., "Antenna Pattern Analysis and Measurement for Multiparameter Radars", in *J. Atmos. Sci.*,10,674-683.

[39] Brunkow, David, V. N. Bringi, Patrick C. Kennedy, Steven A. Rutledge, V. Chandrasekar, E. A. Mueller, Robert K. Bowie, "A Description of the CSU–CHILL National Radar Facility". *J. Atmos. Oceanic Technol.*, 17, 1596-1608. Phased Array radar (MPAR) for Air Traffic Control and Weather Surveillance". *M/A-COM Technology Solutions Inc.* Lowell, MA.

[40] Bringi V. N. and V. Chandrasekar. "Polarimetric Doppler weather radar". *Cambridge University Press*, 2001.

[41] Yanting Wang, and V. Chandrasekar., "Polarization Isolation Requirements for Linear Dual-Polarization Weather Radar in Simultaneous Transmission Mode of Operation". *IEEE Transacions on Geoscience and Remote Sensing*, Vol.44, No.0, August 2006.

[42] V. Chandrasekar and R. Jeffrey Keeler., "Antenna Pattern Analysis and Measurement for Multiparameter Radars", in *J. Atmos. Sci.*,10,674-683., 2007.

[43] D.A. Brunkow et al., "A Description of the CS-CHILL National Radar Facility", in *J. Atmos. Oceanic Technol.*,17,1596-1608.

[44] G. E. Crain, "Polarization Selection for Phased Array Weather Radar", *IEEE International Symposium on Geosciences and Remote Sensing*, 2007.

[45] Guifu Zhang; Doviak, R.J., Zrnic, D.S., Crain, J., Staiman, D., Al-Rashid, Y., "Phased Array Radar Polarimetry for Weather Sensing: A Theoretical Formulation for Bias Corrections," *Geoscience and Remote Sensing, IEEE Transactions*, vol.47, no.11, pp.3679-3689, Nov. 2009.

[46] David Pozar and Barry Kaufman, "Design Consideration for Low Sidelobe Microstrip Arrays", *IEEE Trans. Antennas and Propagation*, Vol. 38, No.8, pp. 1176-1185, August 1990.

[47] Pozar, D. M., "A review of bandwidth enhancement techniques for microstrip antennas," Microstrip Antennas: Analysis and Design of Microstrip Antennas and Arrays, 157-166, *IEEE Press*, 1995.

[48] D. M. Pozar and D. H. Schaubert, "Scan Blindness in Infinite Phased Array of printed Dipoles", 1*984 IEEE Tansactions of Antenna and Propagation*, Vol. 32, No.6, pp. 602-610, June 1984.

[49] D. M. Pozar and D. H. Schaubert, "Analysis of an Infinite Array of Rectangular Microstrip Patches with Idealized Probe Feeds," *IEEE Trans. Antennas and Propagation*, Vol. AP-32, pp. 1101-1107, October 1984.

[50] Pozar, D.M., "The active element pattern," *Antennas and Propagation, IEEE Transactions on* , vol.42, no.8, pp.1176-1178, Aug 1994.

[51] J. Huang, "The finite ground plane effect on the microstrip antenna radiation patterns," *IEEE Transactions on Antennas and Propagation,*vol. 31, no. 4, pp. 649–653, July 1983.

[52] Vaudon, P., Aubreton, T., Dufrane, P., and Jecko, B., "Influence of the ground plane structure on the radiation pattern of microstrip antennas", *Ann. Telecommun.*, 1993, 48, (5–6), pp. 319–329

[53] David M. Pozar, "A Review of Aperture Coupled Microstrip Antennas: History, Operation, Development, and Applications", *University of Massachusetts at Amherst Amherst*, MA 01003, May 1996.

[54] D. M. Pozar and S.D. Targonski, "Improved Coupling for Aperture Coupled Microstrip Antennas", *1991 IEEE Electronics letters*, Vol.27 No.13, June 20th 1991.

[55] S. Gao, L. W. Li, M.S. Leong, and T.S. Yeo, "A broad-Band Dual-Polarized Microstrip Patch Antenna with Aperture Coupling", *IEEE Trans. Antennas and Propagation*, Vol. 51, No.4, pp. 898-900, April 2003.

[56] J. R. Whinnery and H. W. Jamieson, "Equivalent circuits for discontinuities in transmission lines," in *Proc. Inst. Radio Eng.,* vol. 32, no. 2, pp. 98–114, Feb. 1944.

[57] Arun K. Bhattacharyya, "Phased Array Antennas: Floquet Analysis, Synthesis, BFNs and Active Array Systems", a *John Wiley &Son, INC.*, Publications, 2005.

[58] "Report of the Investigation of Models for Evaluating Technology to Reduce Attenuation in Radomes for 9-GHz-band Meteorological Radars (excerp)", *Support Center for Advanced Telecommunications Technology Research*, March 2009.

[59] Rafael Medina, Jorge Luis Salazar, Rafael Medina, Eric Knapp, Anthony Hopf., "T/R Module for CASA Phase-Tilt Radar Antenna Array". *2010 IEEE International Symposium on Phased Array System & technology*, October 15, 2010.

[60] Ansys/Ansoft HFSS, version 11.2, *www.ansoft.com.*

[61] D. M. Pozar, "A Review of Bandwidth Enhancement Techniques for Microstrip Antennas", pp. 157-166, in Microstrip Antennas, *IEEE Press*, 1995.

[62] D. M. Pozar and D. H. Schaubert, "Analysis of an Infinite Array of Rectangular Microstrip Patches with Idealized Probe Feeds," *IEEE Trans. Antennas and Propagation*, Vol. AP-32, pp. 1101-1107, October 1984.

[63] H.Leaderman, "Electrical design of normal-incidence radomes," Chap. 10 in Radar Scanners and Radomes., Eds., *McGraw-Hill,* New York (1948).

[64] Lee Kyung-Wong, Chung Yeong-Chul, Hong Ic-Oyo, and Yook Jong-Gwan, "An Effective Design Procedure for A-sandwich Radome," in *Antennas and Propagation Society International Symposium (APSURSI)*, Toronto, ON, 2010.

[65] Ben A. Munk, "Frequency Selective Surface: Theory and Design," , *New York*, 2000.

[66] Norman E. Clough, "Innovations in ePTFE Fiber Technology : New Capabilities, New Applications, New Opportinities," *in Techtextil North America Symposium 2009*, April 21-23, 2009.

[67] Charles E. Hendrix, James E. McNally, and Robert A. Monzingo., "Depolarization and Attenuation Effects of radomes at 20 GHz", I*EEE Transaction in Antennas and Propagation*, Vol.37, No3, March 1989.

[68] A.W. Rudge., K. Milne., A.D. Olver., P.Knight and R.H.J.Cary., " The handbook of Antenna Design"., *IEE electromganetic Series*., 2nd. Edition, 1986.

[69] J.M. Coulson, J.F. Richardson, J.R.Backhurst and J.H. Harker.,*"Chemical Engineering"*. 6th ed. *Butterworth Heinemann*, Vol1.

[70] Guifu Zhang, J. Vivekanandan and Edward Brandes., "A Method for estimating Rain Rate and Drop Size Distribution from Polarimetric Radar Measurements", *IEEE Transactions on Remote Sensing*, Vol. 39, No.4, April 2001.

[71] Nilsson, M., and Rothstein, J. P., "Using sharp transition in contact angle hysteresis to move and deflect droplets on a superhydrophobic surface," submitted *Phys. Fluids*, (2011).

[72] Johnson, M.F.G., Schluter, R.A., Miksis, M. J., and Bankoff, S.G., "Experimental study of rivulet formation on an inclined surface plate by fluorescent imaging" , *J Fluid Mech* 1999.

[73] Ari Sihvola., "Mixing Rules with Complex Dielectric Coefficients", *Subsurface Sensing Technologies and Applications* Vol. 1, No. 4, 2000.

[74] MIL-Handbook 217, 1991.

[75] D. N. McQuiddy et al., "Transmit/receive module technology for X-band active array radar". *Proc. IEEE* 79, 308-341, 1991.

[76] Agrawal, A.K.; Holzman, E.L.; , "Active phased array design for high reliability," *Aerospace and Electronic Systems, IEEE Transactions on* , vol.35, no.4, pp.1204-1211, Oct 1999.

[77] Van Vliet, F.E., Van Wanum, M., Roodnat, A.W., Alfredson, M. "Fully-integrated wideband TTD core chip with serial control", *Gallium Arsenide applications symposium*. GAAS 2003, 6-10

[78] Oct. 2003, Munich.

[79] Brookner, Eli, " Antenna Array Fundamentals", *Raytheon Co.*, Wayland MA. 1991.

[80] Balbir S. Dhillon, " Reliability Engineering in Systems Desin and Operation", *Van Nostrand Reinhold Company Inc.* 1983.

[81] B.D.Dickinson and L.Sessen, "Life Cycle Cost Procurment of Systems and Spares", *Anual Reliability and Maintainability Symposium*, 1975, pp 282-286.